Industrial Chemistry & Materials

ROYAL SOCIETY OF CHEMISTRY

REVIEW

View Article Online
View Journal

Cite this: DOI: 10.1039/d6im00018e

Electrochemical upcycling of polyethylene terephthalate: catalyst design, reaction mechanisms, and integrated paired electrolysis

Xi Zhu,[a] Lingwei Hu,[b] Xingqun Zheng,[c] Qingmei Wang,[d] Jitao Li,[b] Dan Liu,[e] Weiwei Lei,[e] Yi Zeng,[f] Qingsong Hua*[f] and Shun Lu*[g]

Polyethylene terephthalate (PET) waste has become a persistent global environmental challenge. Electrochemical PET upcycling has recently emerged as a promising strategy. This review provides a comprehensive overview of the reaction pathways, catalyst design principles, and integrated paired-electrolysis strategies for the ethylene glycol oxidation reaction (EGOR). The EGOR proceeds through C_1 (formic acid, FA) and C_2 (glycolic acid, GA) oxidation pathways, with product selectivity governed by several key factors including the catalyst, applied potential and electrolyte conditions. The catalysts for the EGOR focus on noble metals, transition-metal compounds, metal–organic frameworks, organic catalysts, and heterojunction architectures. Besides the anodic EGOR, energy-efficient paired electrolysis systems coupling the EGOR with cathodic reactions, such as hydrogen evolution, two-electron oxygen reduction to H_2O_2, CO_2 reduction, and nitrate reduction, are highlighted for their ability to lower cell voltage and enable the co-production of value-added chemicals. Mechanistic insights derived from spectroscopy characterization and theoretical calculations are critically examined to elucidate active-site evolution, intermediate stabilization, and reaction-depth control. Finally, key challenges and future opportunities are identified, including selectivity control at industrial current densities, impurity tolerance, product separation, and standardized testing protocols. This review aims to provide a mechanistic and system-level framework to guide the rational design of selective, energy-efficient, and scalable electrochemical PET upcycling technologies.

Keywords: Electrochemical upcycling; Polyethylene terephthalate; Ethylene glycol oxidation; Paired electrolysis; Formic acid.

Received 14th January 2026,
Accepted 22nd April 2026

DOI: 10.1039/d6im00018e

rsc.li/icm

1 Introduction

Polyethylene terephthalate (PET) is one of the most extensively manufactured polymers worldwide, valued for its mechanical strength, transparency, and chemical durability.[1–5] With annual production exceeding 80 million tons and continuous growth driven by packaging, textiles, and consumer goods, PET waste accumulation has become a critical environmental threat.[6,7] Its high crystallinity, hydrophobic aromatic backbone, and resistant ester linkages hinder natural degradation, resulting in long-term persistence in ecosystems, microplastic formation, and bioaccumulation across food webs.[8] The rapid increase of consumption and slow turnover of

[a] Department of Crop & Soil Sciences, University of Georgia, Georgia 30223, USA
[b] School of Physics and Telecommunications Engineering, Zhoukou Normal University, Zhoukou 466001, China
[c] School of Safety Science and Engineering, Chongqing University of Science & Technology, Chongqing 401331, China
[d] School of Chemistry and Chemical Engineering, Guizhou University, Guiyang, Guizhou 550025, China
[e] School of Science, STEM College, RMIT University, Melbourne, Australia
[f] School of Physics and Astronomy, Beijing Normal University, Beijing 100875, China. E-mail: q.hua@bnu.edu.cn
[g] Chongqing Institute of Green and Intelligent Technology, Chinese Academy of Sciences, Chongqing 400714, China. E-mail: lushun@cigit.ac.cn

Xi Zhu

Xi Zhu is currently a postdoctoral researcher at the University of Georgia, USA. She received her Ph.D. degree in 2023 from Chongqing Institute of Green and Intelligent Technology, Chinese Academy of Sciences. Her research interests focus on the fabrication of functional nanomaterials and their applications in electrochemical degradation of environmental pollutants, electrochemical sensing, and energy storage devices.

waste highlight an urgent need to establish scalable recycling and valorization technologies to convert PET into recoverable carbon products.[9]

Conventional PET recycling routes, including mechanical reprocessing,[10] thermochemical cracking,[11–13] and chemical[14–18] or enzymatic depolymerization,[3,19–21] have achieved varying levels of industrial relevance but remain constrained by fundamental limitations. Mechanical recycling inevitably downgrades polymer quality; thermochemical cracking requires high temperatures (>450–600 °C) and generates complex, low-selectivity product mixtures; solvolysis routes (glycolysis, methanolysis, alkaline hydrolysis) rely on corrosive reagents and energy-intensive conditions. Even biocatalytic PET hydrolysis, while operating under mild conditions, suffers from low turnover rates, enzyme instability, and high cost. Photocatalytic PET degradation has recently been explored as a low-temperature alternative;[22] however, its practical impact is hindered by insufficient photon utilization, slow kinetics, and catalyst deactivation. Consequently, most existing recycling technologies largely reduce waste volume rather than achieving closed-loop monomer recovery.

Electrochemical oxidation (EO) has recently gained attention as a compelling alternative to thermochemical and solvent-driven depolymerization. EO enables PET conversion under ambient conditions without high temperatures or reactive solvents.[23–25] PET is first hydrolyzed into ethylene glycol (EG) and terephthalate, after which EG becomes the central electroactive intermediate.[26] Depending on the catalyst surface structure, dynamic phase reconstruction, and applied potential, EG can undergo C_1 oxidation to formic acid (FA) *via* C–C bond cleavage or C_2 oxidation to glycolic acid (GA).[27,28] Importantly, the ethylene glycol oxidation reaction (EGOR) operates at significantly lower overpotential rates than the OER, reducing overall cell voltage and enabling the co-production of value-added chemicals.[29]

At present, PET upcycling in electrochemical systems generally follows two distinct pathways: i) material upcycling. It converts PET into functional materials, such as carbon,[30] metal–organic frameworks (MOFs) for batteries, supercapacitors, and electrocatalysts.[3,31–37] For example, Xu *et al.* developed a one-step pyrolysis method using a nickel-based catalyst to convert discarded PET bottles into oxygen-rich, highly graphitized carbon nanotubes (CNTs) with porous structures and abundant functional groups.[38] The optimized CNT-700 material exhibited excellent electrochemical performance, including high capacitance, low resistance, and outstanding cycling stability exceeding 9000–10 000 cycles. ii) Catalytic chemical or electrochemical upcycling that transforms PET into higher-value chemicals and fuels. Wei *et al.* demonstrated that PET can be effectively degraded through an electrochemical pathway, where the PET-derived EG is selectively oxidized into GA using a defect-rich PdSb catalyst.[39] This review focuses on the latter, with particular emphasis on electrocatalytic PET degradation and electro-upcycling, which provide selective, energy-efficient routes for carbon valorization.

Recent publication trends have underscored the rapidly growing interest in PET upcycling, as shown by Web of Science searches using the keywords "PET" and "upcycling", as well as the combined terms "PET", "upcycling", and "electrochemical". Both datasets reveal a steady year-over-year rise in research output (Fig. 1a and b), indicating not only the expanding scientific attention to PET valorization but also the urgent need for sustainable and energy-efficient pathways besides conventional recycling. Within this landscape, electrochemical PET conversion has emerged as a particularly dynamic frontier.

Herein, this work involves four tightly interconnected dimensions (Fig. 1c): (i) PET-derived EGOR pathways are discussed, including C_1 and C_2 routes that determine carbon utilization and product value, along with the key factors that regulate the selectivity between these pathways; (ii) the development of advanced electrocatalysts, including noble metals, transition-metal compounds, MOFs, organic systems, and heterojunction interfaces; (iii) the design of paired

Qingsong Hua

Qingsong Hua is a Distinguished Professor at Beijing Normal University. He received his PhD degree in Mechanical Engineering from Clausthal University of Technology, Germany. Prior to joining Beijing Normal University, he gained extensive academic and industrial experience in both China and Germany. His research focuses on lithium batteries, fuel cells, and their hybrid systems, with particular emphasis on full-chain integrated research and engineering applications.

Shun Lu

Shun Lu is an Associate Professor at Chongqing Institute of Green and Intelligent Technology, Chinese Academy of Sciences, China. He received his Ph.D. degree in Agricultural Biosystems and Mechanical Engineering from South Dakota State University, USA (2021). His research interests include the structure–activity exploration of nickel-based catalysts and their applications in environmental and energy science. He was selected into the Stanford–Elsevier World's Top 2% Scientists list (2024) and awarded the ACS Energy & Fuel Rising Star (2025).

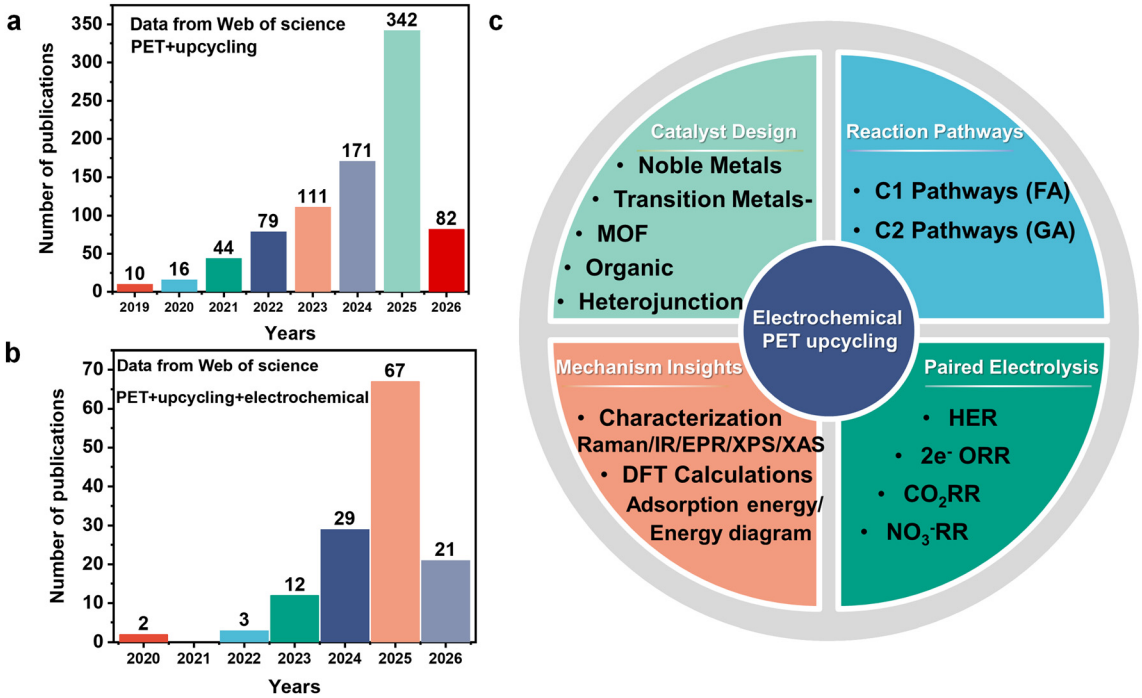

Fig. 1 Publication trends based on keyword searches using (a) "PET" and "upcycling", and (b) the combined terms "PET", "upcycling", and "electrochemical"; (c) overview of electrochemical PET upcycling, summarizing major reaction pathways, catalyst categories, paired cathodic reactions, and key mechanistic pathways.

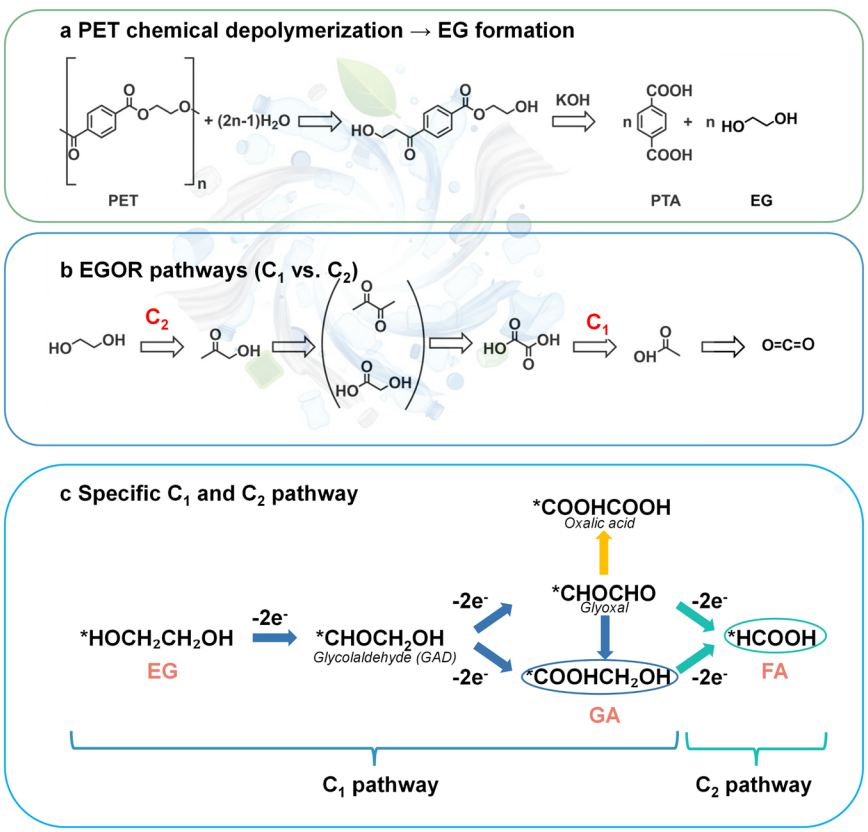

Fig. 2 PET hydrolysis and electrochemical upgrading. (a) Chemical depolymerization converts PET into EG and PTA; (b) EGOR pathways showing C_1 products of FA and C_2 products of GA; (c) proposed reaction pathways for the EGOR (C_1 for FA and C_2 for GA).

electrolysis architectures that couple the EGOR with value-added cathodic reactions such as the hydrogen evolution reaction (HER), oxygen reduction reaction to H_2O_2 ($2e^-$ ORR), CO_2 reduction reaction (CO_2RR), and nitrate reduction reaction (NO_3^-RR) to enhance overall energy efficiency and co-product formation; (iv) mechanistic elucidation through *in situ* spectroscopy and theoretical calculations to unravel active-site evolution, reaction pathways, and C_1/C_2 oxidation selectivity. Together, these research directions define the core framework of emerging electrochemical PET upcycling technologies and highlight the importance of a systematic and comprehensive review.

2 Degradation pathway of PET-derived EG

EO provides a mild, scalable, and environmentally compatible alternative pathway.[40] Instead of relying on heat or strong chemicals, EO operates under ambient conditions and directly activates EG through anode-generated oxidative species such as ·OH, superoxide, and metal-oxo intermediates.[41] Because pristine PET is electrically insulating, depolymerization or alkaline hydrolysis is first conducted to release EG and terephthalate (TPA), as shown in Fig. 2a, after which the EGOR becomes the core transformation step. The EGOR is thermodynamically more favorable than the conventional OER, enabling simultaneous PET upcycling and reduced energy input.[42] Depending on reaction depth and applied potential, the EGOR follows two competitive pathways: C_1 pathway: complete C–C cleavage yields FA or formate as the dominant product;[43] C_2 pathway: partial oxidation produces GA or glycolate while retaining the carbon backbone.[44]

At moderate potentials, selective C_2 products are desirable due to reduced energy loss and higher carbon utilization.[45] However, under aggressive industrial current densities (>300 mA cm^{-2}), excessive oxidation facilitates C–C cleavage and shifts selectivity toward C_1 species (Fig. 2b). Therefore, controlling reaction conditions and tailoring the catalyst electronic structure remain critical for directing the oxidation toward aimed C_1 or C_2 products.

2.1 C_1 pathway

The EGOR allows deep oxidative cleavage of EG to generate C_1 products with high atom utilization. Among various oxidation outcomes, FA represents the most valuable and widely reported C_1 product.[46] During electrooxidation, EG undergoes stepwise α-C–H dehydrogenation to form glycolaldehyde, which is further oxidized to GA. Subsequent C–C bond scission of GA produces FA through either the $HOCH_2COO^- \rightarrow HCOO^- + CO_2 + 2e^-$ pathway or the aldehyde–formate intermediate route, depending on the catalyst properties and potential.[43] Under sufficiently strong anodic conditions, EG may also be directly oxidized to FA *via* a four-electron pathway, whereas deeper oxidation can convert FA into CO_2, making selectivity control essential. The specific reaction equations for C_1 products are exhibited in eqn (1)–(7) (Fig. 2c):[47–49]

$$CH_2OHCH_2OH \rightarrow (CH_2OHCH_2OH)_{ads} \quad (1)$$

$$(CH_2OHCH_2OH)_{ads} + 2OH^- - 2e^- \rightarrow (CHOCH_2OH)_{ads} + 2H_2O \quad (2)$$

$$(CHOCH_2OH)_{ads} + 2OH^- - 2e^- \rightarrow (COOHCH_2OH)_{ads}\ (GA) + H_2O \quad (3)$$

$$(CHOCH_2OH)_{ads} + 2OH^- - 2e^- \rightarrow (CHOCHO)_{ads} + 2H_2O \quad (4)$$

$$(CHOCHO)_{ads} + H_2O \rightarrow (COOHCH_2OH)_{ads}\ (GA) \quad (5)$$

$$(COOHCH_2OH)_{ads} + 2OH^- - 2e^- \rightarrow 2(HCOOH)_{ads}\ (FA) + H_2O \quad (6)$$

$$(CHOCHO)_{ads} + 2OH^- - 2e^- \rightarrow 2(HCOOH)_{ads}\ (FA) \quad (7)$$

FA yields are closely dependent on the catalyst electronic structure, surface oxyhydroxide formation kinetics, and OH^- availability. Catalysts that facilitate rapid formation of high-valence NiOOH/CoOOH typically exhibit stronger oxidative capability and favor C–C cleavage, thereby enhancing FA selectivity. Meanwhile, the reaction environment plays a decisive role: alkaline media accelerate EG deprotonation and C_1 formation, while high current density (>300 mA cm^{-2}) can trigger over-oxidation toward CO_2.[50] Properly optimized electrocatalysts and potential regulation therefore enable PET-derived EG to transform into formate efficiently, representing a key route for closed-loop carbon upcycling toward C_1 chemicals. Jiang *et al.* developed a self-supported $NiCo_2O_4$ electrocatalyst on nickel foam (NF) for selectively converting PET-derived EG into C_1 products, primarily formate.[51] The synergistic redox interplay between Ni and Co centers enhanced EG activation and directed efficient C–C bond cleavage toward C_1 pathways. The catalyst achieved a high formate faradaic efficiency (FE) of 96.7% and industrial-level current density.

Qi *et al.* employed DFT calculations to investigate the reaction energetics for the EGOR toward FA.[47] The calculated free-energy pathways suggest that EG initially adsorbs on the NiOOH surface and subsequently undergoes sequential dehydrogenation steps, forming glycolaldehyde, GA, formaldehyde, and ultimately FA. Notably, the rate-determining step varies with catalyst composition. For $Cr_{0.15}$–$Ni(OH)_2$–NiOOH, the highest energy barrier corresponds to the dehydrogenation of formaldehyde (1.18 eV). In contrast, for Cr–Ni_3S_2–NiOOH, the rate-limiting step shifts to the adsorption of EG with a significantly reduced barrier of 0.67 eV. These results suggest that sulfur incorporation promotes EG adsorption and effectively decreases the overall reaction barrier, while the combined electronic modulation from Cr and S helps stabilize the NiOOH active phase and improves catalytic performance (Fig. 3a).

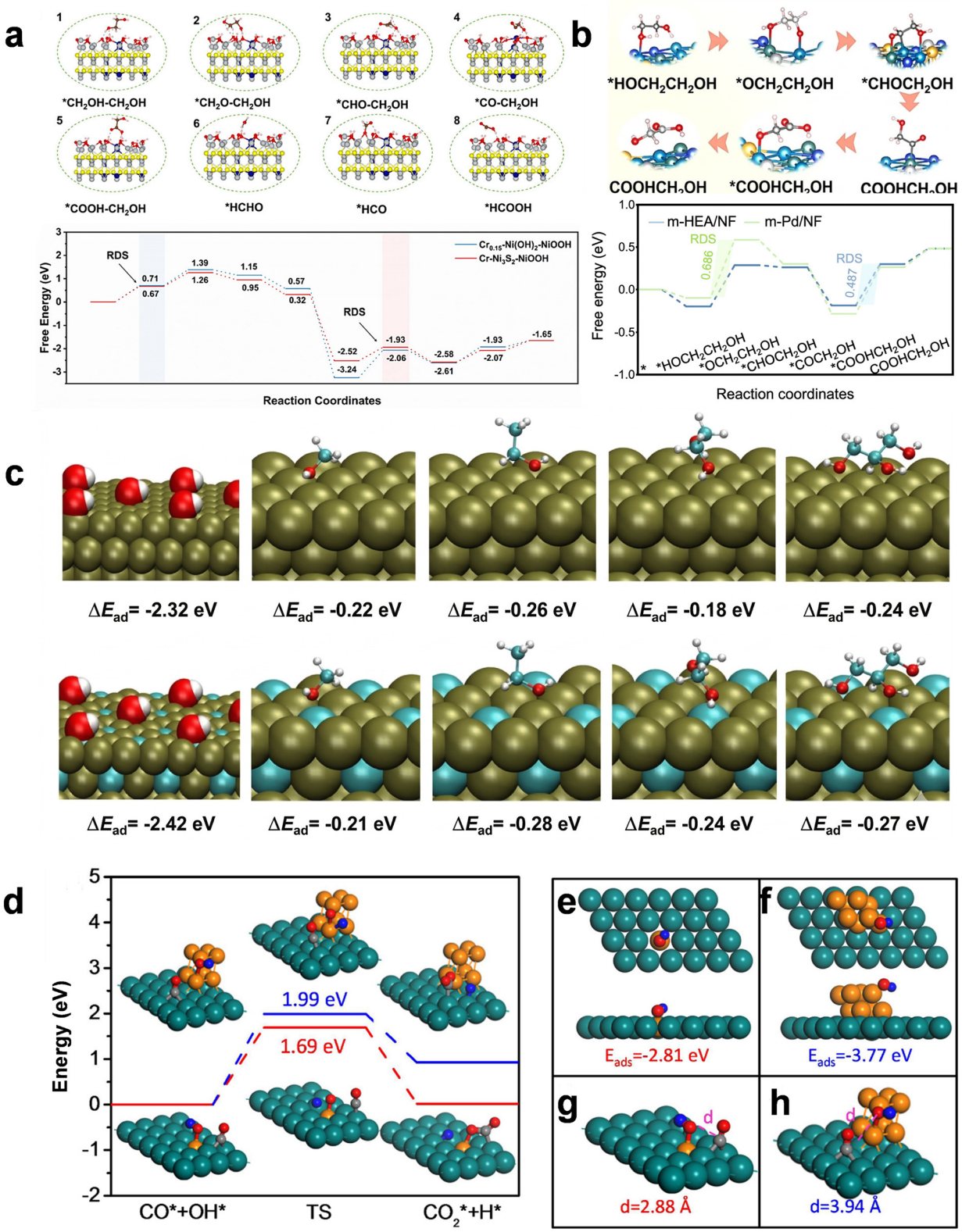

Fig. 3 (a) Reaction pathways of the EGOR with the calculated Gibbs free energy diagram illustrating the C_1 pathway involving C–C bond cleavage. Reprinted with permission from ref. 47. Copyright 2025, Wiley; (b) optimized adsorption configurations of key EGOR intermediates on mesoporous high-entropy alloy (m-HEA/NF) together with the calculated free-energy profiles for the C_2 pathway (EG → GA) on m-HEA/NF and m-Pd/NF. Reprinted with permission from ref. 52. Copyright 2025, Wiley; (c) DFT-optimized adsorption configurations of oxygenated molecules on Pd(111) and $Pd_3Cu(111)$ surfaces; (d) reaction energy profile for CO_{ads} oxidation *via* the Langmuir–Hinshelwood mechanism. Reprinted with permission from ref. 53. Copyright 2016, Elsevier; (e and f) calculated OH_{ads} binding energies on Ru_1@Pt and Ru_8@Pt surfaces; (g and h) optimized configurations showing the distance between CO_{ads} and OH_{ads} at energetically favorable sites. Reprinted with permission from ref. 54. Copyright 2019, Elsevier.

2.2 C_2 pathway

The C_2 pathway of the EGOR proceeds under relatively mild anodic potentials (<1.3 V *vs.* RHE) or on less oxidized catalyst surfaces, enabling partial oxidation without full C–C bond cleavage.[55] In this route, EG is first oxidized at the α-carbon to generate glycolaldehyde or glyoxal, followed by further transformation into GA or glycolate anions through a C–H activation-dominated mechanism. The corresponding reactions for C_2 products are shown in the following eqn (8)–(12) (Fig. 2c).[48,49,56,57]

$$CH_2OHCH_2OH \rightarrow (CH_2OHCH_2OH)_{ads} \quad (8)$$

$$(CH_2OHCH_2OH)_{ads} + 2OH^- - 2e^- \rightarrow (CHOCH_2OH)_{ads} + 2H_2O \quad (9)$$

$$(CHOCH_2OH)_{ads} + 2OH^- - 2e^- \rightarrow (COOHCH_2OH)_{ads} + H_2O \quad (10)$$

$$(CHOCH_2OH)_{ads} + 2OH^- - 2e^- \rightarrow (CHOCHO)_{ads} + 2H_2O \quad (11)$$

$$(CHOCHO)_{ads} + H_2O \rightarrow (COOHCH_2OH)_{ads} \quad (12)$$

For example, Wang *et al.* investigated the co-electrochemical upcycling of nitrate and PET plastics using a mesoporous Pd_3Au film on Ni foam, with a particular focus on producing the C_2 product GA from PET-derived EG.[58] The Pd–Au synergy and mesoporous architecture significantly enhanced the EGOR, enabling a high FE of 95.32% for GA at 0.9 V. Theoretical analysis showed that optimized adsorption of $*OCH_2–CH_2OH$ and strengthened C–C bond activation pathways favored selective C_2 product formation. Zhou *et al.* demonstrated this concept using a mesoporous high-entropy alloy supported on NF (m-HEA/NF).[52] In Fig. 3b, DFT calculations indicate that the EGOR on m-HEA/NF proceeds through a series of surface-bound intermediates ($*HOCH_2CH_2OH \rightarrow *OCH_2CH_2OH \rightarrow *CHOCH_2OH \rightarrow *COCH_2OH \rightarrow *COOHCH_2OH$), suggesting a stepwise dehydrogenation process that maintains the C–C bond and ultimately leads to glycolaldehyde (GA) formation. The calculated free-energy diagram (Fig. 3b) shows that the reaction on m-HEA/NF requires significantly lower energy barriers than on m-Pd/NF. In particular, the rate-determining step corresponds to the dehydrogenation of $*OC–CH_2OH$ to *GA with a barrier of 0.487 eV, whereas a higher barrier of 0.686 eV is observed on m-Pd/NF. This difference implies that m-HEA/NF provides a more favorable energetic landscape for stabilizing key C_2 intermediates. Consequently, catalysts with moderate oxidation capability, such as m-HEA/NF, can suppress excessive C–C bond cleavage and promote the selective formation of C_2 products during the EGOR.

2.3 Selectivity toward C_1 and C_2 pathways

Current EGOR studies are still largely dominated by C_1 products, mainly FA, because C–C bond cleavage proceeds readily on highly oxidizing oxyhydroxide-type surfaces.[56,57] However, from the perspectives of carbon utilization and product value, steering selectivity toward C_2 products such as glycolate is a more rational target whenever downstream separation and utilization are feasible, as it avoids unnecessary carbon loss caused by deep oxidative fragmentation and retains more chemical energy in the products.

Achieving C_2 selectivity requires suppressing excessive reaction depth. Electrochemically, this corresponds to avoiding conditions where the ratio of surface oxidants to substrate becomes too high. Current potential plays a central role: high current potential often drives the system into a transport-limited regime with oxidant-rich surfaces, which accelerates secondary oxidation and promotes C–C cleavage. Next, we analyze product selectivity from the perspectives of catalyst composition, applied potential, and electrolyte conditions.

2.3.1 Catalyst composition. The selectivity of the EGOR is strongly dependent on the catalyst design. Both the composition and structural configuration of electrocatalysts can significantly influence the reaction pathway by modulating the adsorption strength of reaction intermediates and the ability to cleave C–C bonds.[59] Rational tuning of the catalyst components, electronic structure, and surface geometry can therefore regulate whether the EGOR proceeds through partial oxidation (C_2 pathway) or complete oxidation (C_1 pathway).[60,61] Consequently, optimizing the catalyst composition and architecture has become an effective strategy for controlling product distribution during the EGOR.

For example, de Lima *et al.* investigated the EGOR on Pt–Ru catalysts and found that the catalyst composition strongly influences product distribution.[62] Increasing the Ru content enhances the overall oxidation rate but shifts the reaction toward partial oxidation pathways, producing mainly C_2 products (GA). Freitas *et al.* reported that introducing an Ir interlayer beneath a Pt surface ($Pt_{pc}/Ir_{3.0}/Pt_{3.0}$) ($Pt_{pc}$ = polycrystalline Pt) significantly enhances C–C bond cleavage during the EGOR, leading to higher CO_2 formation (C_1 pathway), whereas polycrystalline Pt primarily produces partial oxidation C_2 products such as GA.[63] Tang *et al.* reported that screw-like PdPt nanowires with high-index facets significantly enhance C–C bond cleavage during the EGOR, resulting in increased CO_2 formation (C_1 pathway), whereas conventional Pt catalysts mainly produce partial oxidation C_2 products.[64]

In addition to experimental studies, theoretical calculations provide powerful tools for understanding and predicting product selectivity in the EGOR. DFT calculations can be used to evaluate key descriptors such as adsorption energies of reaction intermediates, activation barriers of elementary steps, and Gibbs free energy changes along reaction pathways.[60,65,66] These parameters provide fundamental insights into the thermodynamic feasibility and kinetic preference of competing reaction routes. By constructing detailed reaction networks and comparing the

energetics of C_2-retaining pathways *versus* C–C bond cleavage routes, theoretical calculations can help identify the dominant reaction pathway and predict the resulting product distribution.[67] These theoretical predictions can further provide important guidance for rational catalyst design, enabling the development of electrocatalysts with improved activity and enhanced selectivity toward desired EGOR products. Serov *et al.* investigated Pd–Cu electrocatalysts for the EGOR by combining experimental studies with DFT calculations.[53] Theoretical results showed that the adsorption energy of hydroxyl species on the $Pd_3Cu(111)$ surface (−2.42 eV) is stronger than that on Pd(111) (−2.32 eV), indicating that the introduction of Cu promotes OH adsorption on the catalyst surface. The enhanced OH_{ads} coverage facilitates the oxidation of adsorbed intermediates and accelerates the overall oxidation reaction (Fig. 3c). Wang *et al.* studied Ru-modified Pt_3Mn nanocrystals for the EGOR by combining *in situ* FTIR spectroscopy with theoretical calculations.[54] The *in situ* FTIR results showed that Pt_3Mn–Ru catalysts favor C–C bond cleavage of EG and facilitate the rapid oxidation and removal of CO_{ads} intermediates. DFT calculations further revealed that the Pt_3Mn–Ru surface exhibits a lower reaction barrier (1.69 eV) for CO_{ads} oxidation assisted by OH_{ads} species and provides an energetically favorable configuration with a CO_{ads}–OH_{ads} distance of about 2.88 Å. These results demonstrate that tuning the electronic structure and surface configuration of catalysts can regulate key reaction steps and guide the rational design of Pt-based catalysts with improved activity and selectivity for the EGOR (Fig. 3d–h).

From the perspective of catalyst design, the adsorption strength of hydroxyl species on the catalyst surface can serve as an important descriptor for controlling EGOR pathways. DFT studies have shown that stronger hydroxyl–surface interactions facilitate C–C bond cleavage of polyol molecules, thereby promoting deeper oxidation toward C_1 products.[68] Therefore, theoretical calculations that evaluate hydroxyl adsorption energies provide a useful strategy for screening catalysts capable of selectively producing C_1 products during the EGOR.

2.3.2 Applied potential. In addition to the catalyst composition and structure, the applied potential also plays a critical role in determining the reaction pathway and product distribution during the EGOR.[69] Variations in potential can significantly influence the adsorption and oxidation of intermediates as well as the ability to cleave C–C bonds, thereby shifting the reaction between partial oxidation (C_2 pathway) and complete oxidation (C_1 pathway).[70,71] *In situ* spectroscopic studies have clearly demonstrated the potential-dependent evolution of reaction intermediates and products during the EGOR.[72,73]

Xin *et al.* demonstrated that the applied potential strongly controls EGOR product selectivity on Pt/C. At low potentials (~0.3 V *vs.* SHE), the EGOR mainly produces C_2 products such as GA, whereas at higher potentials (>0.6 V *vs.* SHE), C–C bond cleavage occurs and C_1 products such as FA are formed.[74] Tang *et al.* investigated the potential-dependent product distribution during the EGOR using *in situ* SPAFTIR spectroscopy on Pd_1Pt_1 nanowires.[64] At potentials below approximately −0.4 V *vs.* RHE, the spectra are dominated by bands corresponding to C_2 products (GA). As the potential increases toward −0.1–0 V *vs.* RHE, a clear CO_2 band (~2343 cm^{-1}) emerges, indicating enhanced C–C bond cleavage and a shift of the reaction pathway toward complete oxidation (C_1 pathway). Pech-Rodríguez *et al.* investigated the potential-dependent EGOR pathway on PtMo/C catalysts using *in situ* FTIR spectroscopy.[75] At relatively low potentials, the spectra are dominated by bands corresponding to C_2 intermediates such as glycolate, glyoxal, and glyoxylate, indicating that the EGOR proceeds mainly through the partial oxidation pathway. As the potential increases above approximately 0.7 V *vs.* RHE, CO_2 bands (~2345 cm^{-1}) begin to appear and intensify, demonstrating that higher potential promotes the oxidation of intermediates and favors the C_1 pathway with complete oxidation to CO_2.

Product selectivity in the EGOR is also governed by a combination of applied potential, adsorption energetics of reaction intermediates, and surface hydroxyl affinity. A representative example is the Pt/SePC catalyst, which demonstrates how these factors collectively regulate the formation of C_2 products.[49] The optimal performance was achieved at 0.8 V *vs.* RHE, delivering 94.6% EG conversion and 84.4% GCA selectivity, while retaining stable catalytic activity with negligible degradation during durability tests. At the electronic-structure level, DFT calculations revealed that Se doping modulates the adsorption configuration and energetics of EG-derived intermediates. Specifically, the free-energy barrier for the EG → glycolaldehyde conversion decreased from 1.24 to 1.05 eV, while the desorption barrier of GCA decreased from 1.37 to 1.16 eV, facilitating the formation and release of C_2 intermediates rather than further oxidation. In addition, the Pt/SePC catalyst exhibited stronger EG adsorption and enhanced OH affinity. The adsorption of EG was evidenced by the largest decrease in open circuit potential after EG addition (0.332 V for Pt/SePC, compared with 0.265 V for Pt/PC and 0.232 V for Pt/C), indicating stronger adsorption of EG in the inner Helmholtz layer. Meanwhile, CO stripping measurements showed a lower onset potential for CO oxidation on Pt/SePC, suggesting a higher affinity for adsorbed OH species and facilitated formation of reactive OH_{ad} intermediates. Together, these results indicate that selective C_2 production requires a balanced catalytic environment involving a moderate potential window, optimized adsorption energetics of reaction intermediates, and appropriate surface OH coverage, which collectively suppress excessive oxidation and stabilize C_2 products such as GA.

2.3.3 Electrolyte conditions. The electrolyte composition and pH also play important roles in regulating EGOR product selectivity by altering surface hydroxyl coverage, intermediate stability, and reaction kinetics.[76–79] For example, Sitta *et al.*

systematically investigated the electro-oxidation of EG on Pt electrodes over a wide pH range and showed that the reaction pathway and product distribution strongly depend on electrolyte pH.[77] In alkaline media, the EGOR mainly produces C_2 intermediates. These observations highlight that the electrolyte composition and pH can shift the balance between C_2 partial oxidation and deeper oxidation pathways by modifying interfacial reaction kinetics and intermediate adsorption behavior. In addition, Sitta *et al.* investigated the electro-oxidation of EG on Pt electrodes in alkaline media containing different alkali cations.[79] The results show that the nature of the electrolyte cation significantly influences the reaction kinetics and product distribution. Stronger noncovalent interactions between hydrated cations and surface oxygenated species increase surface blockage and hinder C–C bond cleavage. As a result, the formation of C_1 products decreases in the order $K^+ > Na^+ > Li^+$, while the production of partially oxidized C_2 species such as oxalate becomes more favorable when smaller cations are present. These findings demonstrate that electrolyte cations can regulate EGOR pathways by modifying interfacial interactions and the availability of surface oxygenated species.

3 Catalyst design for the EGOR

Catalysts for the EGOR can be classified into five major categories (Fig. 4): noble metals,[80,81] transition metal-based compounds,[82–85] MOF catalysts,[86] organic catalysts,[87] and hybrid interfaces including metal-oxide junctions,[88–90] LDH heterostructures, MOF-derived materials, and bimetallic catalysts. Among them, Ni- and Co-based catalysts, particularly NiOOH and NiFe/CoFe LDHs, represent the most efficient and widely used systems for the EGOR, while noble metals remain benchmarks for reaction kinetics.[89] Hybrid catalysts are emerging as next-generation materials capable of enhancing activity, selectivity, and stability in the EGOR.

3.1 Noble-metal catalysts

3.1.1 Single noble catalysts. The EGOR has increasingly relied on noble-metal catalysts, which offer high intrinsic activity, well-defined electronic structures, and excellent resistance to corrosion under oxidative conditions.[80,81] These properties make noble metals particularly effective for the EGOR, enabling rapid C–C activation and high selectivity toward value-added products. Early efforts have focused on single-metal systems such as Pt, Pd, and Au, which provide clean model platforms for understanding adsorption energetics, reaction intermediates, and structure–activity relationships during the EGOR.[91–93]

Pt-based catalysts are widely considered among the most effective electrocatalysts for the EGOR.[94] Pt catalysts exhibit limited capability for C–C bond cleavage, which leads to the formation of multiple C_2 intermediates.[63,64] Hu *et al.* synthesized ultrasmall Pt nanoparticles with controllable sizes and dominant crystal facets *via* a simple chemical reduction strategy.[95] The Pt nanoparticles with ~2 nm size and (111)-dominant facets exhibited superior electrocatalytic activity toward the EGOR in an alkaline electrolyte (0.5 M KOH + 0.5 M EG), delivering a specific activity of 15.51 mA cm^{-2}

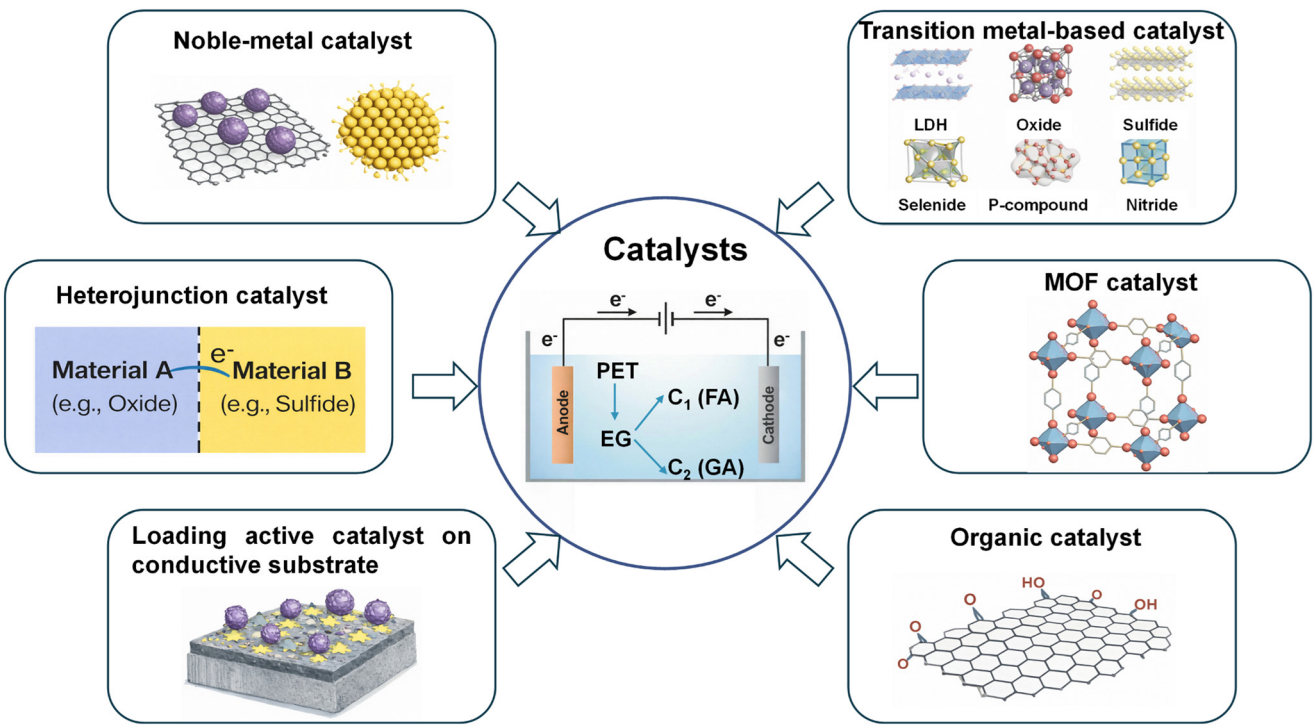

Fig. 4 Catalysts for the EGOR.

and a mass activity of 5.22 A mg^{-1}, which are significantly higher than those of commercial Pt/C. The enhanced performance was attributed to the small particle size and the exposure of Pt(111) facets, which provide more active edge sites and facilitate intermediate oxidation during the EGOR. Sitta *et al.* investigated the EGOR on Pt under both steady-state and oscillatory conditions and found that pH strongly governs activity, reaction order, oscillation kinetics, and activation energy, with a notable transition near pH 12.[77] The study attributes low-pH inhibition to CO poisoning and high-pH enhancement to its absence, offering mechanistic insight into EGOR dynamics.

Palladium has also been widely investigated for the EGOR owing to its catalytic properties like Pt and its relatively lower cost.[39,57,96–98] Pd catalysts generally exhibit high activity for alcohol oxidation in alkaline media and improved tolerance toward poisoning intermediates. However, Pd surfaces still suffer from partial blockage by strongly adsorbed species, and their ability to cleave the C–C bond is limited.[99] As a result, the EGOR on Pd typically proceeds through partial oxidation pathways, predominantly producing C_2 products such as glycolaldehyde, GA, and oxalic acid rather than deep C_1 oxidation products.[100] Ghosh *et al.* developed Pd nanoparticles supported on polypyrrole-modified reduced graphene oxide for the EGOR in alkaline media.[101] The hybrid support improves Pd dispersion and electron transfer, resulting in enhanced catalytic activity and stability compared with Pd/C catalysts. Like many Pd-based catalysts, the EGOR on Pd mainly proceeds through partial oxidation pathways, generating C_2 products.

Au catalysts exhibit superior resistance to poisoning and good stability during alcohol oxidation. However, the intrinsic catalytic activity of Au toward the EGOR is generally lower due to its weaker adsorption toward reaction intermediates.[102,103] In most cases, the EGOR on Au proceeds through partial oxidation pathways, predominantly yielding C_2 products such as glycolate and oxalate. Therefore, various strategies, including alloying, nanostructure engineering, and support interactions, have been explored to improve the catalytic activity and selectivity of Au-based catalysts.[104,105] Wang *et al.* reported facet-engineered Au aerogels as monometallic catalysts for the EGOR in alkaline media.[106] By tuning the (111), (100), and (110) surface facets of Au aerogels, they found that the catalytic activity toward the EGOR strongly depends on the exposed crystal facets, where the activity follows the order (111) $\gg$ (100) $>$ (110). The EGOR on Au surfaces mainly proceeds through partial oxidation pathways, generating C_2 oxygenated products containing carboxylate groups, which tend to adsorb strongly on Au surfaces and influence catalyst stability.

3.1.2 Metal alloy catalysts. However, despite monometallic catalysts having high activity, single-metal catalysts often suffer from limited selectivity tuning, poisoning by strongly adsorbed species, and constrained electronic flexibility.[107,108] To overcome these limitations, recent advances have shifted toward multi-metal architectures, including alloyed nanoparticles, core–shell structures, and metallenes that incorporate two or more noble metals or noble–non-noble combinations.[55,97] These multi-metallic catalysts leverage synergistic electronic interactions, including d-band modulation, p–d hybridization, and interfacial charge redistribution, to optimize intermediate binding, facilitate C–C bond scission or preservation, and suppress overoxidation pathways.[109–111] Systems such as Pt-, Pd-, and Au-based alloys have demonstrated markedly superior activity and product selectivity compared with their monometallic counterparts, highlighting the benefits of cooperative catalysis. Wang *et al.* detailed a mesoporous Pd_3Au/Ni foam catalyst for the simultaneous electrochemical upcycling of nitrate and EGOR, achieving $>$95% FEs for GA formation.[58] Their theoretical analysis shows that Pd–Au synergy optimizes intermediate adsorption and C–C bond stabilization, enabling highly selective co-production of these value-added products. Han *et al.* reported a pulsed-electrocatalysis strategy using a lamellar mesoporous PdCu catalyst to selectively form GA during the EGOR with $>$92% FE, high yield rates, and strong cycling stability (Fig. 5).[40] The pulsed mode enhances GA desorption and active-site renewal, and the method is effective for scaled-up processing of real PET waste. Noble metals possess intrinsically stable electronic structures and well-defined adsorption behavior, enabling α-C–H dehydrogenation and subsequent intermediate oxidation at lower overpotentials.[77,112] This allows fine regulation of product pathways between C_1 (FA) and C_2 (GA). Early mechanistic investigations have clarified key EGOR intermediates on Pt, Au, and Pd surfaces, and revealed how pH and potential govern C–C cleavage and oxidation depth.[43] More recent studies have further demonstrated that noble-metal catalysts can drive the EGOR toward small-molecule products without undergoing oxidative reconstruction or forming MOOH-like species. Under pulsed-potential or moderate-current operation, they maintain high C_2 conversion efficiency and exhibit excellent conductivity along with resistance to surface deactivation.

In addition, Ru- and Ir-based catalysts can also be used in alcohol electrooxidation owing to their unique electronic properties;[63,113] however, they are rarely employed as standalone catalysts for the EGOR. Ru exhibits strong oxophilicity and a high affinity for OH^- adsorption, which facilitates the formation of surface hydroxyl species that can oxidize poisoning intermediates. Nevertheless, pure Ru surfaces often suffer from limited stability and excessive C–C bond cleavage, leading to poor product selectivity.[114] Similarly, Ir possesses excellent chemical stability and corrosion resistance under oxidative potential, but its intrinsic activity toward EG adsorption and activation is relatively moderate, which limits its catalytic efficiency when used alone.[115] As a result, Ru- and Ir-based catalysts are more commonly incorporated into alloy or hybrid systems with other metals.[54,72,109,116] In these alloys, Ru or Ir typically acts as an oxophilic promoter, providing abundant OH* species and modifying the electronic structure of neighboring active

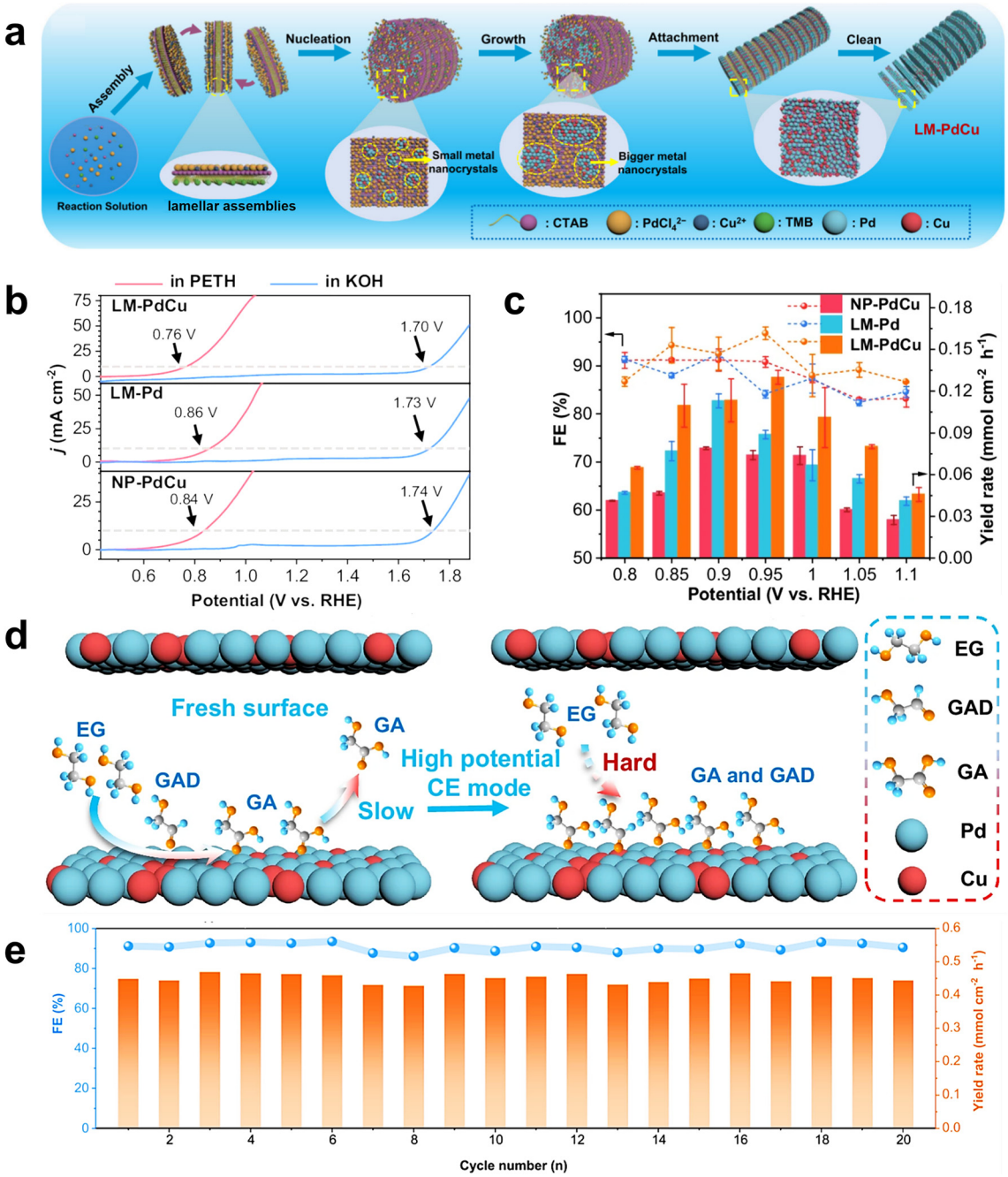

Fig. 5 (a) Scheme of the proposed formation mechanism of LM-PdCu; (b) LSV curves of LM-PdCu, LM-Pd, and NP-PdCu recorded in 1 M KOH with PETH (0.10 M EG) at a scan rate of 5 mV s^{-1}; (c) FE and GA production rates over different catalysts; (d) scheme of GA electrosynthesis from PET upcycling under CE operation; (e) cycling stability of LM-PdCu for the selective electrosynthesis of GA during the EGOR. Reprinted with permission from ref. 40. Copyright 2025, Springer.

metals through ligand and strain effects. This synergistic interaction can accelerate the oxidation of carbonaceous intermediates, suppress catalyst poisoning, and optimize the adsorption–desorption balance of reaction intermediates.[114,117,118] Consequently, alloying Ru or Ir with other metals has become an effective strategy to enhance EGOR activity, selectivity, and long-term stability compared with their monometallic counterparts. For example, Dai *et al.* synthesized shape-controlled PtIr alloy nanocrystals with high-index facets *via* an electrodeposition strategy and investigated their catalytic performance toward the EGOR.[113] PtIr tetrahexahedral (THH) nanocrystals exhibited significantly enhanced activity compared with commercial Pt/C, delivering a forward peak current density of 19.9 mA cm^{-2} for the EGOR. The improved performance was attributed to the synergistic effect between Pt and Ir, where alloying modifies the electronic structure of Pt and optimizes the adsorption strength of reactants and intermediates. In addition, the high-index facets

of the PtIr nanocrystals provide abundant low-coordinated kink and step atoms, which serve as highly active sites for alcohol oxidation. As a result, the combined effect of alloying and surface structure engineering enables superior activity and stability for the EGOR. Duan *et al.* synthesized porous dendritic PtRuPd nanospheres (NS) *via* a one-pot aqueous method using hexadecylpyridinium chloride as a structure-directing agent.[119] The trimetallic PtRuPd catalyst exhibited significantly enhanced catalytic activity toward the EGOR, delivering a forward peak current density of 116.11 mA cm^{-2} and a mass activity (MA) of 1.368 A mg^{-1}, both higher than those of PtPd, PdRu, and commercial Pt/C catalysts. The improved performance was attributed to the synergistic interaction among Pt, Ru, and Pd, where Pt provides the primary active sites for the EGOR, Ru promotes the adsorption of OH^- species and facilitates the removal of CO-like intermediates, and Pd improves the electronic structure and anti-poisoning ability of the catalyst. In addition, the dendritic porous morphology exposes abundant active sites and enhances mass and electron transport, resulting in improved EGOR activity and durability.

Overall, multi-metallic noble-metal catalysts provide an effective strategy to overcome the limitations of monometallic systems in the EGOR by tuning electronic structures, optimizing intermediate adsorption, and improving resistance to catalyst poisoning. The synergistic interactions among different metals, combined with rational nanostructure design, enable enhanced catalytic activity, selectivity, and durability, offering important guidance for the development of high-performance EGOR catalysts.

3.2 Transition metal-based catalysts

Transition-metal compounds represent the most extensively investigated class of anodic catalysts, owing to their tunable electronic structures, multiple accessible oxidation states, and strong ability to activate C–H and C–C bonds. This section summarizes the categories of transition-metal compounds in the EGOR, such as LDHs, oxides, sulfides, selenides, phosphides, phosphates, and nitrides.[120]

3.2.1 LDHs

3.2.1.1 Monometallic LDHs. LDHs, particularly Ni-LDH, Co-LDH, and Fe-LDH, represent one of the most efficient families of catalysts for EG.[121,122] LDHs possess tunable metal compositions, abundant edge active sites, and exceptional redox versatility, enabling rapid *in situ* reconstruction into high-valence oxyhydroxide species under anodic polarization.[116,123] These reconstructed MOOH layers serve as the true active phases for the EGOR, while the brucite-like layered framework provides fast OH^- diffusion pathways and facilitates efficient electron transport, significantly accelerating reaction kinetics.[124] Yan *et al.* developed an Au/$Ni(OH)_2$ catalyst by depositing Au nanoparticles onto $Ni(OH)_2$ nanosheet arrays grown on NF.[125] The conductive $Ni(OH)_2$ support provides abundant hydroxyl groups and facilitates strong interfacial interactions with Au, promoting efficient electron transfer during the reaction. As a result, the catalyst exhibits excellent EGOR activity, delivering a current density of 326.2 mA cm^{-2} at 1.15 V *vs.* RHE with a GA selectivity of 91%. Mechanistic studies reveal that EG molecules are enriched at the Au/$Ni(OH)_2$ interface through the interaction between Au and alkoxide species and hydrogen bonding with $Ni(OH)_2$. This dual interaction increases the local reactant concentration and accelerates the electrooxidation kinetics, enabling high current densities under moderate potentials.

3.2.1.2 Bimetallic LDHs. Compared with monometallic LDHs (*e.g.*, Ni-LDH, Co-LDH), bimetallic LDHs such as NiFe-LDH,[126] CoFe-LDH,[121] and NiCo-LDH[127] exhibit significantly enhanced catalytic activity and selectivity in the EGOR.[83,122] The superior performance originates from the electronic modulation and synergistic redox interactions introduced by the second metal cation. In monometallic LDHs, the transition from Ni^{2+} or Co^{2+} to their high-valence counterparts is thermodynamically possible but kinetically limited, resulting in slower formation of the active oxyhydroxide (MOOH) layer and restricted rates of α-C–H activation and C–C bond oxidation. In contrast, incorporation of a second metal, such as Fe^{3+}, substantially modulates the d-band electronic structure of Ni or Co, lowering the energy barrier for oxidation and enhancing metal–oxygen covalency as well as oxygen-vacancy density. These effects collectively promote the rapid generation of electrophilic oxygen species that govern key steps in the EGOR. The presence of Fe also improves charge-carrier mobility and interfacial electron separation, enabling bimetallic LDHs to stabilize C_2 intermediates such as $HOCH_2COO^-$ and thus suppress excessive C–C cleavage. As a result, monometallic LDHs typically show moderate activity and favor C_1 pathways, whereas bimetallic LDHs achieve higher current densities, lower overpotentials, and superior C_2 product selectivity. These properties establish bimetallic LDHs as the most promising LDH catalysts for advanced EGOR electro-upcycling. For example, Jiang *et al.* prepared a MOF-derived NiCo hydroxide catalyst to upcycle PET-derived EG with high selectivity, achieving 96.5% FE for FA and identifying Co^{3+}/Co^{4+} as the key C–C cleavage sites.[128] Liu *et al.* reported that nickel–iron LDH (NiFe-LDH) is an effective catalyst for the anodic EGOR.[126] The incorporation of Fe into the LDH framework significantly enhances EGOR activity and selectivity while suppressing the competing OER. During the EGOR, NiFe-LDH maintains excellent structural stability; the increased metal-oxygen hybridization facilitates the formation of selective active sites that preferentially oxidize the hydroxyl groups of EG. When integrated into an electrochemical reactor using NiFe-LDH as the anode catalyst and Ag nanoparticles as the cathode catalyst, the system operates at a low full-cell voltage of 1.9 V and achieves nearly 100% FE for CO at 50 mA cm^{-2}. Li *et al.* presented a hierarchical Ni-MOF@MnCo-OH catalyst for the EGOR.[46] The multi-metal heterostructure enhances OH* and EG adsorption and improves electron transfer, achieving ~80%

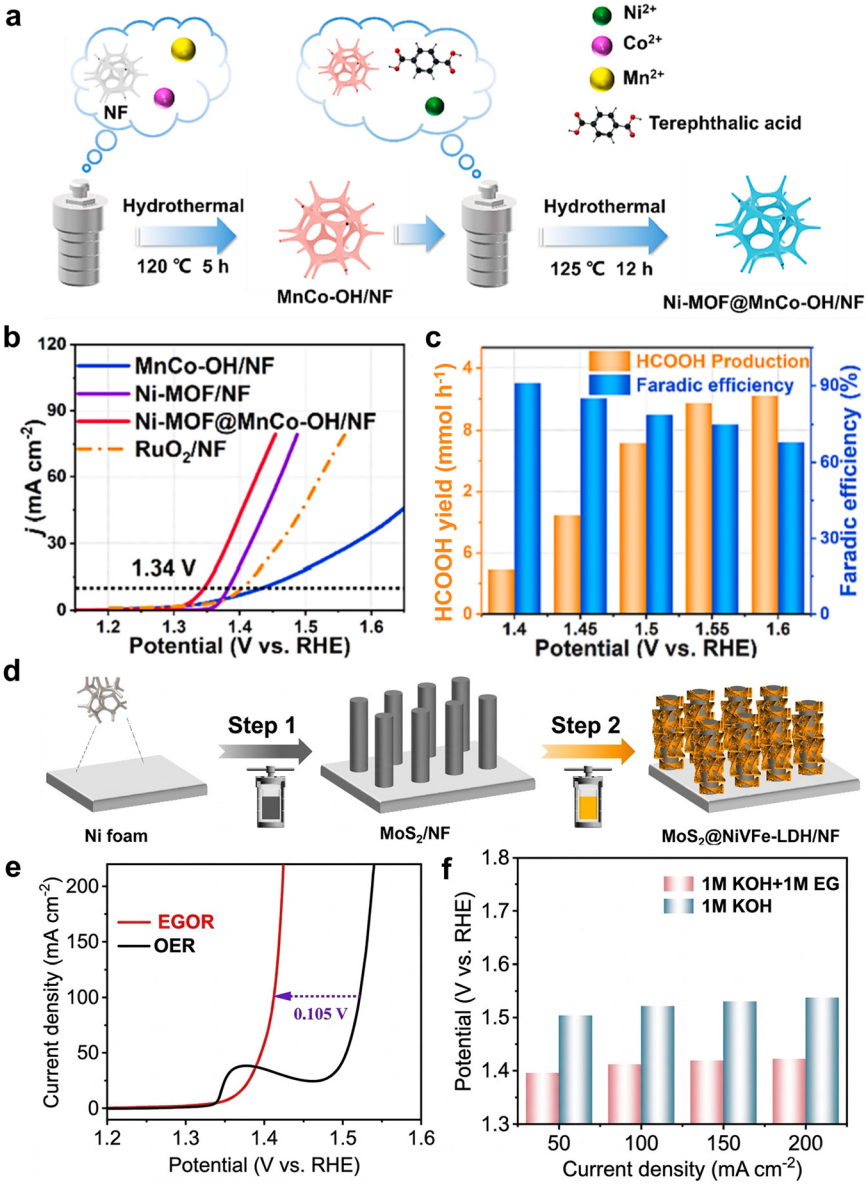

Fig. 6 (a) Scheme of the construction of the NiMOF@MnCo-OH/NF catalyst; (b) polarization curves of MnCo-OH/NF, Ni-MOF/NF, and NiMOF@MnCo-OH/NF; (c) FE and FA yield for the EGOR over Ni-MOF@MnCo-OH/NF at different applied potentials. Reprinted with permission from ref. 46. Copyright 2024, Elsevier; (d) scheme of the fabrication of MoS_2@NiVFe-LDH/NF and its EGOR performance; (e) LSV curves of MoS_2@NiVFe-LDH/NF recorded in 1 M KOH with and without 1 M EG; (f) comparison of the potentials required to achieve various current densities in the absence and presence of EG for MoS_2@NiVFe-LDH/NF. Reprinted with permission from ref. 129. Copyright 2025, Elsevier.

FE at 300 mA cm^{-2}. Combined theoretical calculations and *in situ* FTIR reveal GA as a key intermediate in the EGOR pathway (Fig. 6a–c).

3.2.1.3 Trimetallic LDHs. To further optimize catalytic activity and selectivity, recent studies have introduced a third metal component to construct trimetallic LDHs, such as CoFeNi-LDH, NiFeCu-LDH, and NiFeMn-LDH.[83] The introduction of a third metal can regulate the d-band structure of Ni active sites, enhance OH^- adsorption capability, and accelerate the Ni^{2+}/Ni^{3+} redox transition. For instance, CoFeNi-based catalysts exhibit improved electron transfer kinetics and higher density of catalytically active oxyhydroxide species, resulting in enhanced current density and lower onset potentials for the EGOR. For example, Ma *et al.* reported a Ni_3S_2@NiFeMn-LDH nanosheet array catalyst in which Mn incorporation and heterostructure formation optimize the adsorption of EG and reaction intermediates.[83] The catalyst achieved a current density of 266.6 mA cm^{-2} at 1.36 V *vs.* RHE, markedly higher than those of NiFeMn-LDH and NiFe-LDH, while maintaining a formate FE of ~90%, demonstrating the advantage of trimetallic LDH systems for an efficient EGOR. Yang *et al.* constructed a MoS_2@NiVFe-LDH heterostructured catalyst on NF, in which the introduction of V into the NiFe-LDH effectively regulates the electronic structure and increases the number of active sites.[129] Benefiting from the strong

electronic interaction at the MoS_2/NiVFe-LDH interface and the enhanced formation of NiOOH active species, the catalyst exhibited excellent EGOR activity, requiring only 1.39 V *vs.* RHE to reach 50 mA cm^{-2}, which is significantly lower than the 1.50 V required for the OER, demonstrating the advantage of trimetallic LDH systems for glycol oxidation (Fig. 6d–f).

3.2.2 Oxides. Although LDHs exhibit outstanding catalytic activity and tunability for the EGOR due to their flexible layered structure and excellent redox adaptability, their practical performance is often limited by several intrinsic drawbacks.[130,131] These include relatively low electrical conductivity, moderate mechanical stability under prolonged anodic cycling, and susceptibility to layer delamination or partial dissolution in strongly alkaline environments.[50] Moreover, the density of catalytically accessible sites in LDHs is restricted by their brucite-like layer arrangement, and their reconstruction into the active MOOH phase may be

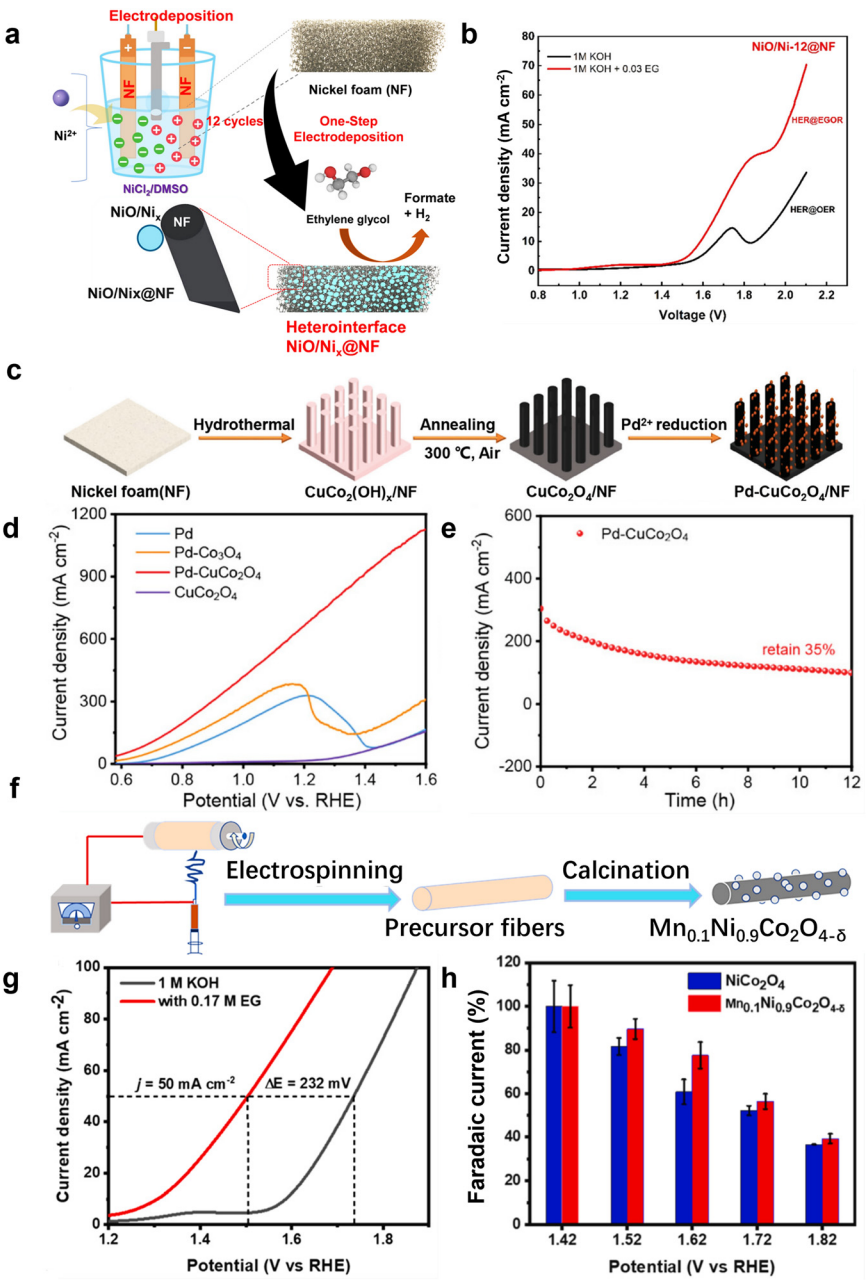

Fig. 7 (a) Scheme of the electrodeposition process for NiO/Ni nanosheets; (b) LSV curves of NiO/Ni-12@NF measured in 1 M KOH with and without 0.03 M EG in a two-electrode configuration. Reprinted with permission from ref. 132. Copyright 2025, The Royal Society of Chemistry; (c) synthetic route of Pd–$CuCo_2O_4$; (d) LSV curves of Pd–$CuCo_2O_4$, Pd–Co_3O_4, Pd, and $CuCo_2O_4$ for the EGOR; (e) stability evaluation of Pd–$CuCo_2O_4$ during the EGOR. Reprinted with permission from ref. 29. Copyright 2024, Wiley; (f) synthetic scheme of $Mn_{0.1}Ni_{0.9}Co_2O_{4-\delta}$; (g) LSV curves of $Mn_{0.1}Ni_{0.9}Co_2O_{4-\delta}$ RSFs for the EGOR; (h) FE of $Mn_{0.1}Ni_{0.9}Co_2O_{4-\delta}$ measured at different applied potentials. Reprinted with permission from ref. 139. Copyright 2023, Elsevier.

incomplete or kinetically hindered under high-current-density operation. These limitations motivate the exploration of alternative catalyst systems with inherently higher conductivity, stronger structural robustness, and more diverse defect chemistries.

3.2.2.1 Monometallic oxides. Transition-metal oxides, such as NiO (ref. 132) and Co_3O_4,[133] thus represent an important complementary class of catalysts for the EGOR.[134] Metal oxides possess rigid crystalline frameworks, rich oxygen-vacancy chemistry, and superior electron-transport properties compared with LDHs, enabling more stable operation at large current densities. Under anodic potential, these oxides undergo *in situ* surface transformation into highly active MOOH species, like LDH reconstruction but often with faster oxidation kinetics and improved durability. For example, Aladeemy *et al.* reported a porous NiO/Ni nanosheet catalyst grown on NF for an efficient EGOR.[132] The catalyst exhibited an onset potential of 1.30 V *vs.* RHE for the EGOR in an alkaline electrolyte and achieved a current density of 121.6 mA cm^{-2} at 1.60 V *vs.* RHE, which is about 4.5 times higher than that of bare Ni/NF. Mechanistic studies revealed that the reaction proceeds through the *in situ* formation of NiOOH active species, which act as redox mediators to promote the stepwise oxidation of EG intermediates (Fig. 7a and b).

3.2.2.2 Bimetallic oxides. Besides simple binary oxides, spinel-type oxides, such as $NiCo_2O_4$,[88,135] have also emerged as an important subclass of oxide catalysts for the EGOR, owing to their mixed-valence metal centers, structural stability, and tunable electronic properties. Bimetallic spinel oxides have been investigated as catalysts for the EGOR, including $NiCo_2O_4$,[34,51,88] $NiFe_2O_4$,[136] and $CuCo_2O_4$.[29] Among these spinel materials, $NiCo_2O_4$ remains the most widely studied spinel catalyst due to its relatively high electrical conductivity (10^{-2}–10^{-1} S m^{-1}).[137] $NiCo_2O_4$ also offers multiple redox-active sites, facilitating efficient α-C–H activation and enhanced selectivity toward C_1 or C_2 oxygenates depending on their electronic structure.[34,51,88] Chen *et al.* found that lattice-oxygen activity determines EGOR performance in MCo_2O_4 spinels.[138] $NiCo_2O_4$ showed the strongest oxygen activity due to its high O 2p ligand-hole density and achieved exceptional metrics with 98.3% formate selectivity and 98.9% FE.

Besides $NiCo_2O_4$, other spinel oxides have also been explored to further tailor the electronic structure and catalytic properties for the EGOR. $NiFe_2O_4$ represents another typical spinel oxide, where the synergistic interaction between Ni and Fe species can also promote EGORs. For example, Zhu *et al.* reported a Ni single atom/P, N-doped amorphous $NiFe_2O_4$ catalyst as an efficient spinel-oxide-derived photoanode for PET hydrolysate oxidation, where the reaction was dominated by the EGOR.[136] Benefiting from the amorphous $NiFe_2O_4$ framework, abundant oxygen vacancies, and optimized Ni–N_3–P local coordination, the catalyst exhibited excellent activity, requiring only 1.39 V *vs.* RHE to achieve 50 mA cm^{-2} under dark conditions. Moreover, the oxidation of PET hydrolysate afforded formate with an FE of up to 93%, highlighting the promise of $NiFe_2O_4$-based spinel oxides for an efficient EGOR.

$CuCo_2O_4$ has also demonstrated promising activity for the EGOR. For example, Liu *et al.* developed a Pd–$CuCo_2O_4$ spinel catalyst for the EGOR coupled with seawater electrolysis.[29] In this system, the $CuCo_2O_4$ surface strongly adsorbs OH^- species, which promotes EG activation and suppresses competing chlorine corrosion in seawater environments. Benefiting from the synergistic interaction between Pd and $CuCo_2O_4$, the catalyst delivered a high EGOR current density of 600 mA cm^{-2} at 1.15 V *vs.* RHE with an FE of 96.1% for GA, while maintaining stable operation for over 100 h (Fig. 7c–e).

3.2.2.3 Trimetallic oxides. In addition to conventional binary spinel oxides, trimetallic spinel catalysts have also been explored for the EGOR, as the incorporation of a third metal can further tune the electronic structure, regulate metal–oxygen covalency, and improve charge-transfer kinetics. These modifications often enhance catalytic activity and suppress competing OER pathways, thereby improving EGOR selectivity and efficiency. For example, Mao *et al.* reported a $Mn_{0.1}Ni_{0.9}Co_2O_{4-\delta}$ spinel nanofiber catalyst for the electro-upcycling of PET microplastics, where PET was first hydrolyzed to generate EG and then selectively oxidized to formate.[139] The optimized catalyst achieved an FE above 95% at 1.42 V *vs.* RHE, with a formate productivity of 4.87 mmol cm^{-2} h^{-1}, demonstrating excellent catalytic activity and selectivity for the EGOR. The enhanced performance was attributed to Mn doping, which modifies the electronic structure of $NiCo_2O_4$ and reduces the lattice-oxygen-driven OER, thereby promoting EGOR pathways (Fig. 7f–h).

Under anodic potentials in alkaline electrolytes, Ni, Co, and Fe oxides undergo dynamic surface reconstruction to form catalytically active MOOH phases, which play a crucial role in alcohol and polyol electro-oxidation reactions. For Ni-based oxides, the catalytic process is generally associated with the electrochemical oxidation of Ni^{2+} to high-valent Ni^{3+} species,[47] leading to the formation of surface NiOOH layers that act as redox mediators for alcohol dehydrogenation during the EGOR.[98] In Co-based oxides, a similar transformation occurs through the oxidation of Co^{2+} to Co^{3+}/Co^{4+} species, generating CoOOH or CoO_2-like surface phases that facilitate C–H bond activation and accelerate the EGOR.[140] Fe-containing oxides can also undergo hydroxylation to form FeOOH under anodic conditions; however, Fe species are generally considered less active toward direct alcohol oxidation. Instead, Fe mainly acts as an electronic modulator that tunes the electronic structure of neighboring Ni or Co sites, stabilizes high-valent oxyhydroxide species, and promotes OH^- adsorption.[141] Notably, these transformations are typically confined to the near-surface region, while the bulk oxide primarily serves as a structural and electronic reservoir during the catalytic cycle.

3.2.3 Sulfides. Although transition-metal oxides exhibit good structural stability and considerable activity for the EGOR, their overall electrical conductivity and electron richness at the metal centers are still limited by the strong metal–oxygen covalency.[142] This constraint hampers charge transport and slows down the generation of high-valence active species under high current densities. To overcome these limitations, research has progressively shifted from oxides to sulfide-based systems. Metal sulfides such as Ni_3S_2 (ref. 98) and Co_9S_8 (ref. 85) possess a more metallic character and significantly higher intrinsic conductivity, enabling faster anodic reconstruction into electron-rich, defect-laden NiOOH/CoOOH shells while retaining a highly conductive sulfide core as an electron reservoir and a transport backbone.[47] Compared with oxides, sulfide-derived MOOH typically features higher oxygen-vacancy concentrations and more coordinatively unsaturated metal sites, which lowers the energy barrier for α-C–H dehydrogenation and the rate-determining step of the EGOR, thereby sustaining faster kinetics and improved product selectivity at elevated current densities.

3.2.3.1 Monometallic sulfides. Monometallic sulfide catalysts reported for the EGOR are Ni- and Co-based sulfides. This focus mainly arises from the favorable redox chemistry of Ni and Co, which can readily undergo Ni^{2+}/Ni^{3+} and Co^{2+}/Co^{3+} transitions under anodic potentials, forming catalytically active oxyhydroxide species that promote alcohol oxidation reactions. In addition, NiCo sulfides generally exhibit high electrical conductivity and facile *in situ* surface reconstruction, which further enhances EGOR kinetics and stability. For example, Chen *et al.* reported a defective NiS hierarchical catalyst for the EGOR.[143] Benefiting from abundant sulfur vacancies and defect engineering, the catalyst exhibited excellent catalytic performance, requiring only 1.34 V *vs.* RHE to achieve 100 mA cm^{-2} for the EGOR. Moreover, the system achieved a FE above 93% for EG-to-formate conversion, demonstrating high activity and selectivity. Mechanistic analysis indicated that the nickel sulfide catalyst undergoes *in situ* surface reconstruction to form an active NiOOH phase, which plays a key role in promoting the EGOR process.

Elemental doping is an effective strategy to regulate the electronic structure of metal sulfides, increase active sites, and accelerate charge-transfer kinetics during the EGOR. Rare-earth elements such as Tb possess highly localized 4f orbitals that are strongly shielded from the chemical environment.[144] As a result, they rarely serve as direct catalytic centers but can effectively modulate the electronic structure of neighboring transition-metal sites, induce oxygen vacancies, and stabilize high-valence metal species, thereby enhancing catalytic activity and durability. For example, Chen *et al.* reported a B and Co dual-doped NiS catalyst for the EGOR.[145] Benefiting from defect engineering and dopant-induced electronic modulation, the catalyst required only 1.34 V *vs.* RHE to reach 100 mA cm^{-2}, while achieving a FE above 93% for EG-to-formate conversion, demonstrating the high catalytic activity and selectivity of doped nickel sulfide systems. In contrast, other sulfides have been much less explored for the EGOR. For example, CuS, FeS, and other sulfides, which possess high electrical conductivity and tunable electronic structures, may represent promising candidates and could be investigated in future studies.

3.2.3.2 Bimetallic sulfides. Compared with monometallic sulfides, bimetallic sulfides usually exhibit enhanced catalytic activity due to the synergistic interaction between different metal centers, which can regulate the electronic structure, improve conductivity, and provide multiple redox-active sites.[140] These features facilitate the formation of active oxyhydroxide species under anodic conditions and accelerate EGOR kinetics. However, current studies on the PET-derived EGOR are still mainly concentrated on Ni–Co sulfides, owing to the favorable redox chemistry of Ni and Co and their facile reconstruction into active NiOOH/CoOOH species. Other bimetallic sulfides have been rarely reported for the EGOR. In the future, extending catalyst design to other bimetallic or trimetallic sulfides may offer new opportunities to further optimize catalytic activity and selectivity. Pataniya *et al.* reported a cerium-incorporated nickel cobalt sulfide (Ce-NiCoS) catalyst for the integrated electrocatalytic upcycling of real PET-derived EG coupled with the HER.[140] Owing to the optimized electronic structure and *in situ*-formed metal oxyhydroxide active sites, the Ce-NiCoS enabled an efficient EGOR at 1.30 V *vs.* RHE at 100 mA cm^{-2}, which is 230 mV lower than the OER, while maintaining high FEs for both formate (96.5%) and H_2 (99%). Importantly, replacing water oxidation with the EGOR reduced the electricity consumption for H_2 production to 4.39 kWh Nm^{-3}, representing an energy saving of approximately 13% compared with conventional water electrolysis.

3.2.4 Selenides

3.2.4.1 Monometallic selenides. Metal selenides ($NiSe_2$ (ref. 60) and Co_3Se_4 (ref. 146)) are regarded as an evolutionary advancement beyond sulfides owing to their higher metallicity, broader d-band characteristics, and superior electron mobility.[60,147] Although M–Se bonds are somewhat weaker than M–S bonds, the oxidation potential of Se^{2-} is significantly higher than that of S^{2-}, making selenides far less susceptible to anion leaching or excessive reconstruction under anodic conditions.[148] Upon applying oxidative potentials, selenides typically generate a thin NiOOH/CoOOH reconstruction shell that remains strongly electronically coupled to the highly conductive Se-rich core. This heterointerface promotes the rapid formation of high-valence metal species, thereby accelerating α-C–H activation and subsequent multi-electron oxidation steps in the EGOR. Furthermore, selenide-derived MOOH often contains a higher density of unsaturated metal centers and oxygen vacancies, lowering the energy barrier for the rate-determining step and improving kinetics and selectivity at elevated current densities. Li *et al.* detailed the development of $NiSe_2$ electrocatalysts for the selective EGOR to formate as a strategy to replace the OER and lower the energy cost of

hydrogen production.[60] By tuning the nanoparticle morphology and crystal phase, the optimized catalyst achieves 50 mA cm^{-2} at only 1.395 V and delivers >80% FE for formate. *In situ* IRAS and DFT calculations confirm a glycolate-mediated C–C cleavage pathway leading to formate as the dominant product, with glycolate and oxalate as minor C_2 species.

3.2.4.2 Bimetallic selenides. Bimetallic selenides have attracted increasing attention as EGOR catalysts due to their tunable electronic structures, synergistic interactions between different metal centers, and enhanced catalytic activity compared to their monometallic counterparts.[146]

Sharma *et al.* developed a bimetallic Ni–Fe_3Se_4 catalyst grown on Ni foam for PET-derived ethylene glycol electrooxidation coupled with hydrogen production.[146] The hierarchically structured Ni–Fe_3Se_4 exhibits low interfacial resistance and abundant active sites, achieving a high FE of ≈89% for formate production and stable operation at industrial-level current densities. Mechanistically, the incorporation of Fe into Ni-based selenide modulates the electronic structure and promotes the formation of NiFeOOH active species under anodic conditions, which serve as the true catalytic sites for EG oxidation. During this reconstruction process, Se species are partially oxidized and may leach into the electrolyte as soluble oxyanions, leading to dynamic surface evolution. This Se removal plays a dual role: on the one hand, it facilitates the formation of defect-rich oxyhydroxide layers, enhances *OH adsorption, and accelerates C–C bond cleavage, thereby favoring selective conversion toward C_1 products such as formate; on the other hand, excessive Se leaching may weaken structural integrity and compromise long-term stability. Therefore, the balance between Se retention and leaching is critical for optimizing both catalytic activity and durability in bimetallic selenide systems.

3.2.5 P-compounds. Phosphorus-containing compounds (P-compounds), including metal phosphides and phosphates, have recently emerged as promising catalysts for the EGOR. These catalysts can also undergo *in situ* transformation into active MOOH species, while the P-containing framework stabilizes the reconstructed layer and promotes efficient electron transport. At present, most phosphorus-based catalysts reported for the EGOR are primarily Ni- and Co-based compounds, while phosphides derived from other transition metals remain largely unexplored. Expanding the composition of metal phosphides beyond Ni and Co may therefore represent a promising direction for future catalyst development. We discuss P-based catalysts for the EGOR, including metal phosphides and phosphates.

3.2.5.1 Metal phosphides. Metal phosphides (*e.g.*, Ni_2P, CoP, FeP, NiCoP) are a highly promising catalyst family besides sulfides and selenides due to their higher electron density, stronger M–P covalency, and more controlled structural evolution during the EGOR.[23,149] Their strong M–P bonding imparts high metallicity and excellent conductivity, allowing the rapid formation of high-valence Ni^{3+}/Ni^{4+} or Co^{3+}/Co^{4+} species under anodic potentials, which effectively accelerate α-C–H dehydrogenation and subsequent multi-electron oxidation steps in the EGOR.[150,151] Compared with oxides, phosphorus-based materials generally exhibit higher electrical conductivity and faster charge-transfer kinetics. Relative to sulfides and selenides, phosphides often possess stronger metal–P bonding and improved structural stability under anodic conditions, reducing anion leaching and excessive surface reconstruction.[121,152] Zhou *et al.* proposed an electrocatalytic strategy for the EGOR into formate, terephthalic acid, and H_2, emphasizing the need for high selectivity and high current density to achieve economic viability.[153] Using a Ni-modified cobalt phosphide ($CoNi_{0.25}P$) catalyst, the system delivers >80% FE for formate at 500 mA cm^{-2} in a membrane-electrode assembly, while maintaining strong selectivity. Structural analyses show that the catalyst evolves into a low-crystalline metal oxy(hydroxide) phase, which serves as the active state for an efficient EGOR. Li *et al.* achieved the development of an ultrathin, porous Fe-doped Ni_2P catalyst for dual-function electrocatalysis, enabling both the EGOR and HER.[90] The Fe-Ni_2P/NF electrode delivers high activity due to abundant active sites and Fe-induced electronic modulation, generating co-produced formate and H_2 at only 1.39 V, significantly lower than conventional water splitting.

3.2.5.2 Metal phosphates. Besides metal phosphides, metal phosphates have emerged as an alternative class of phosphorus-containing catalysts for the EGOR. Although phosphides exhibit excellent conductivity and catalytic activity, their surfaces often reconstruct into active MOOH species under anodic potentials. Phosphate frameworks can serve as stable structural matrices that anchor the reconstructed oxyhydroxide layer, thereby improving structural stability and catalytic durability during the EGOR.[154] For example, Kilaparthi *et al.* reported a $NiCoPO_x$ catalyst supported on activated carbon felt for PET-hydrolysate oxidation coupled with CO_2 reduction.[154] *In situ* Raman spectroscopy revealed the formation of NiOOH/CoOOH active phases during the EGOR, and the system achieved a FE of ~96% for the PET-derived EGOR at a cell voltage of 1.8 V, demonstrating the effectiveness of phosphate-derived catalysts for the EGOR.

3.2.6 Nitrides. Transition metal nitrides have emerged as a promising class of electrocatalysts owing to their metallic conductivity and tunable electronic structures. Compared with oxides or hydroxides, nitrides typically exhibit higher electrical conductivity (103–105 S m^{-1}), enabling faster electron transport during electrochemical reactions.[155] In addition, the incorporation of nitrogen can modulate the electron density of metal centers, thereby optimizing the adsorption energy of key intermediates. Benefiting from these features, many nitride catalysts can deliver current densities of 10–100 mA cm^{-2} at potentials of ~1.20–1.35 V *vs.* RHE for the EGOR in alkaline electrolytes.[156,157] Meanwhile, the strong metal–nitrogen bonding also improves structural stability under highly alkaline conditions, making metal

nitrides attractive candidates for efficient and durable EGOR catalysis. Liu *et al.* reported bifunctional nickel–cobalt nitride nanosheets supported on carbon cloth (Co–Ni_3N/CC) as an efficient electrocatalyst for the PET-derived EGOR.[120] The incorporation of Co regulates the N^{2+}/Ni^{3+} redox behavior and improves EG adsorption and activation, enabling the EGOR at a low potential of 1.15 V *vs.* RHE, significantly lower than that of conventional Ni catalysts (~1.30 V). In PET hydrolysate, the integrated EGOR–HER system achieves 50 mA cm^{-2} at a cell voltage of 1.46 V, demonstrating efficient plastic upcycling coupled with H_2 production. Deng *et al.* reported a hierarchical Co–CeF_3@Ni_3N sheet-on-sheet

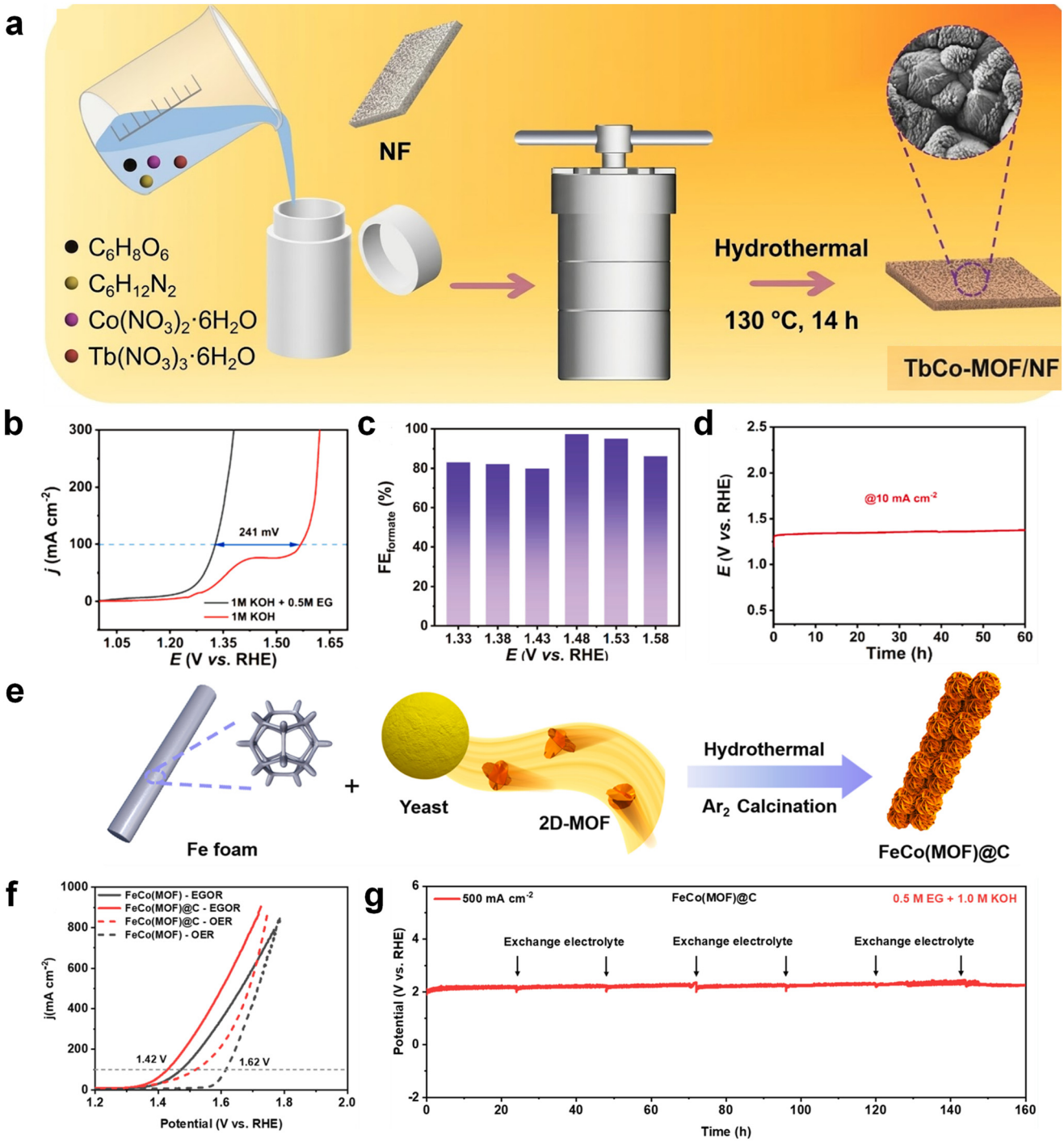

Fig. 8 (a) Scheme of the synthesis of TbCo-MOF; (b) LSV curves of TbCo-MOF/NF in 0.5 M EG + 1 M KOH; (c) FE for formate production at different potentials; (d) chronoamperometric stability of TbCo-MOF/NF for 60 h in 0.5 M EG + 1 M KOH. Reprinted with permission from ref. 163. Copyright 2024, Elsevier; (e) scheme of the synthesis of FeCo(MOF)@C; (f) LSV curves of different samples; (g) stability test of FeCo(MOF)@C at 500 mA cm^{-2} in 0.5 M EG electrolyte. Reprinted with permission from ref. 165. Copyright 2024, The Royal Society of Chemistry.

heterostructure supported on NF (Co–CeF_3@Ni_3N/NF) for PET hydrolysate electro-upgrading.[158] The introduction of Co species modulates the electronic configuration of Ni_3N and optimizes the adsorption of EG and reaction intermediates, thereby enhancing EGOR activity. The catalyst delivers industrial-level current densities of 80–380 mA cm^{-2} at 1.32–1.44 V *vs.* RHE, with formate FE exceeding 97% and stability over 60 h. In a flow electrolyzer, the system achieves 300 mA cm^{-2} at 1.72 V, demonstrating efficient PET upcycling coupled with H_2 production.

3.3 MOF catalysts

3.3.1.1 Monometallic MOFs. MOFs have gradually established themselves as a unique class of electrocatalysts distinct from noble-metal and transition-metal systems, owing to their ordered coordination geometry, exceptionally high surface area (500–6000 m^2 g^{-1}), and the tunability of both metal nodes and organic linkers.[37,159–161] These structural advantages allow MOFs to serve not merely as high-surface-area hosts, but as molecularly programmable catalytic reactors, where metals such as Ni,[41,159,162] Co,[86,163,164] and Fe (ref. 165 and 166) act as Lewis-acid centers to adsorb and activate EG through M–O coordination, lowering α-C–H cleavage barriers and enabling controlled electron transfer.[41,46,160] For example, Roy *et al.* developed a Co-MOF-74 catalyst grown on NF as an anode for the EGOR.[86] Under anodic conditions, the Co-MOF-74 structure undergoes *in situ* reconstruction to form catalytically active cobalt oxyhydroxide species, which exhibit high activity for the EGOR. The catalyst shows a half-wave potential approximately 0.23 V lower than the OER and produces formate as the main product with nearly 100% FE at the early stage of electrolysis, demonstrating the potential of MOF-derived catalysts for efficient PET upcycling through the EGOR.

3.3.1.2 Doped MOFs. Introducing rare-earth elements (such as Ce (ref. 164) and Tb (ref. 163)) into transition-metal catalysts has recently emerged as an effective strategy to enhance electrocatalytic performance. Owing to their partially filled 4f orbitals, rare-earth elements can regulate the electronic structure of neighboring transition-metal centers, promote charge redistribution, and improve electron transfer kinetics. In addition, rare-earth doping can modify the local coordination environment and stabilize high-valence metal species formed during anodic reconstruction, thereby facilitating catalytic reactions. For example, Guo *et al.* reported a Tb-doped Co-MOF catalyst grown on NF for PET hydrolysate electrolysis.[163] The incorporation of Tb effectively modulated the electronic structure of the Co active sites and promoted the formation of CoOOH active species during the EGOR. As a result, the TbCo-MOF/NF electrode achieved 10 mA cm^{-2} at a cell voltage of 1.55 V in a two-electrode system, demonstrating improved activity for the PET-derived EGOR coupled with hydrogen production (Fig. 8a–d).

3.3.1.3 Bimetallic MOFs. Introducing multiple metal centers into MOFs offers clear advantages over monometallic counterparts by enabling electronic structure modulation, optimized intermediate adsorption, and the creation of synergistic dual active sites. These features not only enhance intrinsic catalytic activity but also mitigate poisoning from strongly adsorbed intermediates and broaden the tunability of product selectivity in organic electrooxidation.[41] Li *et al.* prepared carbon-sphere-supported orthogonal FeCo-MOF nanosheet catalysts *via* a microbial-template strategy for an efficient EGOR and HER.[165] The catalyst requires only 1.42 V for the EGOR, 307 mV for the HER, and 1.83 V for the coupled EGOR||HER at 100 mA cm^{-2} and delivers stable operation for 160 h at 500 mA cm^{-2}. The high surface area of the bimetallic MOF and the synergistic yeast-derived carbon shell enhance contact with *OH and EG, thereby improving activity and durability (Fig. 8e–g). At present, the few reported MOF catalysts for the EGOR predominantly yield C_1 products, such as formate or CO_2,[41,86,162–166] and studies on the selective formation of C_2 products are still lacking. Therefore, understanding how the MOF structure and active sites influence C_2 selectivity remains an important topic for future research.

3.4 Organic catalysts

Following the tunable metal–ligand reactivity of MOFs, purely organic catalysts represent a metal-free alternative for the EGOR, characterized by well-defined molecular binding sites, redox-tunable conjugated frameworks, and excellent chemical sustainability. Unlike transition-metal catalysts, organic catalysts utilize π-electron delocalization, hydrogen-bonding networks, or N-/O-containing functional groups to mediate α-C–H activation and intermediate stabilization. Polyaniline (PANI), polypyrrole (PPy), and COFs (covalent organic frameworks) exhibit strong affinity for EG through H-bond assisted adsorption and electron-rich conjugated backbones that facilitate dehydrogenation while suppressing deep oxidation. Meanwhile, electron-donating amine or imidazole groups can stabilize $HOCH_2COO$* intermediates, maintaining the C_2 carbon skeleton and promoting glycolate formation.

Compared with MOFs, organic catalysts feature lower density of open active sites but superior flexibility in electronic modulation, enabling selective formate *vs.* glycolate tuning through substituent effects, donor–acceptor structural design, or heteroatom doping. Their metal-free nature avoids dissolution and metal-ion leaching under alkaline EGOR conditions, supporting high stability and sustainability. As organic redox polymers, COFs and N-rich macrocycles may serve as future low-cost catalysts with molecular-level selectivity control for the EGOR. Dinda *et al.* detailed the first metal-free EGOR using the organic electrocatalyst (2,2,6,6-tetramethylpiperidin-1-yl)oxyl (TEMPO), demonstrating selective conversion of PET-derived EG into value-added chemicals and H_2.[87] At pH 10, the system produces glycolate and oxalate exclusively, whereas at pH 14,

over-oxidation induces C–C cleavage to form formate and carbonate. Therefore, pH can be regulated to tune reaction rates and product selectivity.

3.5 Hybrid catalysts

3.5.1 Heterojunction catalysts. Building upon organic–inorganic catalytic concepts, heterojunction catalysts have become one of the most rapidly expanding directions for the EGOR. By integrating two or more electronic phases, such as LDH/metal,[89,167,168] LDH/oxide, LDH/sulfide,[169] MOF/oxide, metal/carbon,[170] or organic–inorganic interfaces,[171,172] heterojunctions generate built-in electric fields that accelerate charge separation, lower activation energy, and direct reaction pathways toward C_2 or C_1 products. The interfacial electric field also facilitates the stabilization of key C_2 intermediates such as $HOCH_2COO^-$, thereby suppressing overoxidation and improving product selectivity.[173] Ren *et al.* constructed a dual-electrolysis platform for co-producing NH_3 and GA from nitrate and PET-derived EG, employing low-crystalline CoOOH and Pd nanothorn electrodes.[27] The system delivers ~97% NH_3 FE and highly selective GA formation at an onset voltage of only 0.5 V, highlighting an energy-efficient route for waste-to-value conversion. Liu *et al.* detailed the electro-reforming of PET-derived EG over a heterojunction Pd–$Ni(OH)_2$ catalyst, achieving >85% FE for GA even at industrial current densities (600 mA cm^{-2}) and maintaining stable operation for over 200 h.[174] Their combined experimental and theoretical analysis shows that $Ni(OH)_2$-promoted OH* generation facilitates EG-to-GA oxidation and removes carbonyl poisons, while the synergistic interaction between Pd's downshifted d-band center and oxophilic Ni enables rapid GA desorption and suppresses over-oxidation, resulting in high activity and selectivity.

Rare-earth elements such as Ce rarely serve as direct catalytic centers but act as electronic promoters that regulate the electronic structure of transition-metal active sites, generate oxygen vacancies through Ce^{3+}/Ce^{4+} redox cycling, and stabilize catalytic interfaces, thereby enhancing catalytic activity and durability.[175] Wu *et al.* developed rose-like $NiCo_2O_4$@CeO_{2-x}/NF for the EGOR.[176] By introducing Ce to modulate the spinel oxide interface and create abundant oxygen vacancies, the catalyst achieved 50 mA cm^{-2} at a low cell voltage of 1.32 V and exhibited enhanced reaction kinetics and durability.

Hybrid interfaces also offer superior mechanical integrity and long-term durability. For instance, Ni_3S_2@NiFe-LDH, $NiSe_2$@MXene, and $NiCo_2O_4$/graphene heterostructures maintain high catalytic performance under large current densities because the conductive core resists structural degradation, while the reconstructed MOOH shell remains highly active throughout cycling. By synergistically combining optimized charge transport, tailored electronic structures, and stable interfacial active sites, hybrid interface catalysts have emerged as one of the most promising platforms for high-rate, low-voltage EGORs. Ma *et al.* developed a Ni_3S_2/NiFeMn-LDH heterostructure as an efficient anodic catalyst for the EGOR coupled with the HER.[83] The Ni_3S_2@NiFeMn-LDH/NF electrode delivered a FE of up to 90% toward formate at an applied voltage of 1.5 V, while glycolate and oxalate were formed in minor amounts. Density functional theory calculations indicated that the phase-separated Ni_3S_2 component plays a key mechanistic role by reducing the energy barrier of the rate-limiting step in the EGOR. He *et al.* designed Pt nanoclusters embedded in a Fe-based MOF (MIL-100(Fe)) as a dual-functional electrocatalyst for both the HER and EGOR.[166] Strong Pt–O interfacial interactions within the MOF enhance electron transfer, increase active-site availability, and accelerate proton–electron coupling, yielding markedly improved activity and durability. The Pt/MIL-100(Fe) catalyst delivers high mass activity and long-term stability for the EGOR compared with commercial Pt/C, demonstrating the promise of metal–MOF interfaces for advanced electrocatalyst design.

3.5.2 Loading active catalysts on conductive substrates. Another strategy to improve EGOR performance is the direct loading of active materials onto conductive substrates (CC, NF, and MXenes).[50,170,177] Self-supported electrodes integrate catalytically active phases with highly conductive frameworks such as NF, CC, or metal meshes. This architecture shortens electron-transport pathways, improves mechanical stability, and exposes a larger number of accessible active sites to electrolytes.[6,173] *In situ* growth of LDHs, oxides, sulfides, or phosphides on porous substrates often produces vertically aligned nanosheets, nanoneedles, or hierarchical architectures that enhance mass transport and facilitate bubble release during electrolysis.[101]

Carbon-based materials are widely used as conductive supports due to their high electrical conductivity, large surface area, and ability to stabilize active sites. Zhang *et al.* reported PdFe alloy nanoparticles supported on nitrogen-doped CNTs (PdFe/N-CNTs) as an efficient electrocatalyst for the PET-derived EGOR.[97] The conductive N-CNT framework promotes rapid electron transport and uniform dispersion of PdFe active sites, thereby improving catalytic activity and stability. As a result, the catalyst delivers 10 mA cm^{-2} at 1.22 V *vs.* RHE with a high FE of 87% for FA production during the EGOR (Fig. 9a–c).

MXenes can also be used as conductive substrates for active catalysts due to their metallic conductivity, large surface area, and abundant surface functional groups. These properties enable strong interfacial interactions with loaded catalysts and facilitate rapid electron transport during electrochemical reactions.[177] Yu *et al.* constructed a $CoCuO_x$@MXene/NF catalyst by anchoring $CoCuO_x$ nanoparticles onto conductive MXene nanosheets supported on NF.[50] The MXene substrate provides high electrical conductivity and abundant surface functional groups, enabling strong interfacial electronic coupling between $CoCuO_x$ and MXene. This heterostructure promotes electron transfer and increases the exposure of active sites, thereby significantly enhancing the catalytic activity toward the EGOR. As a result, the $CoCuO_x$@MXene exhibits a

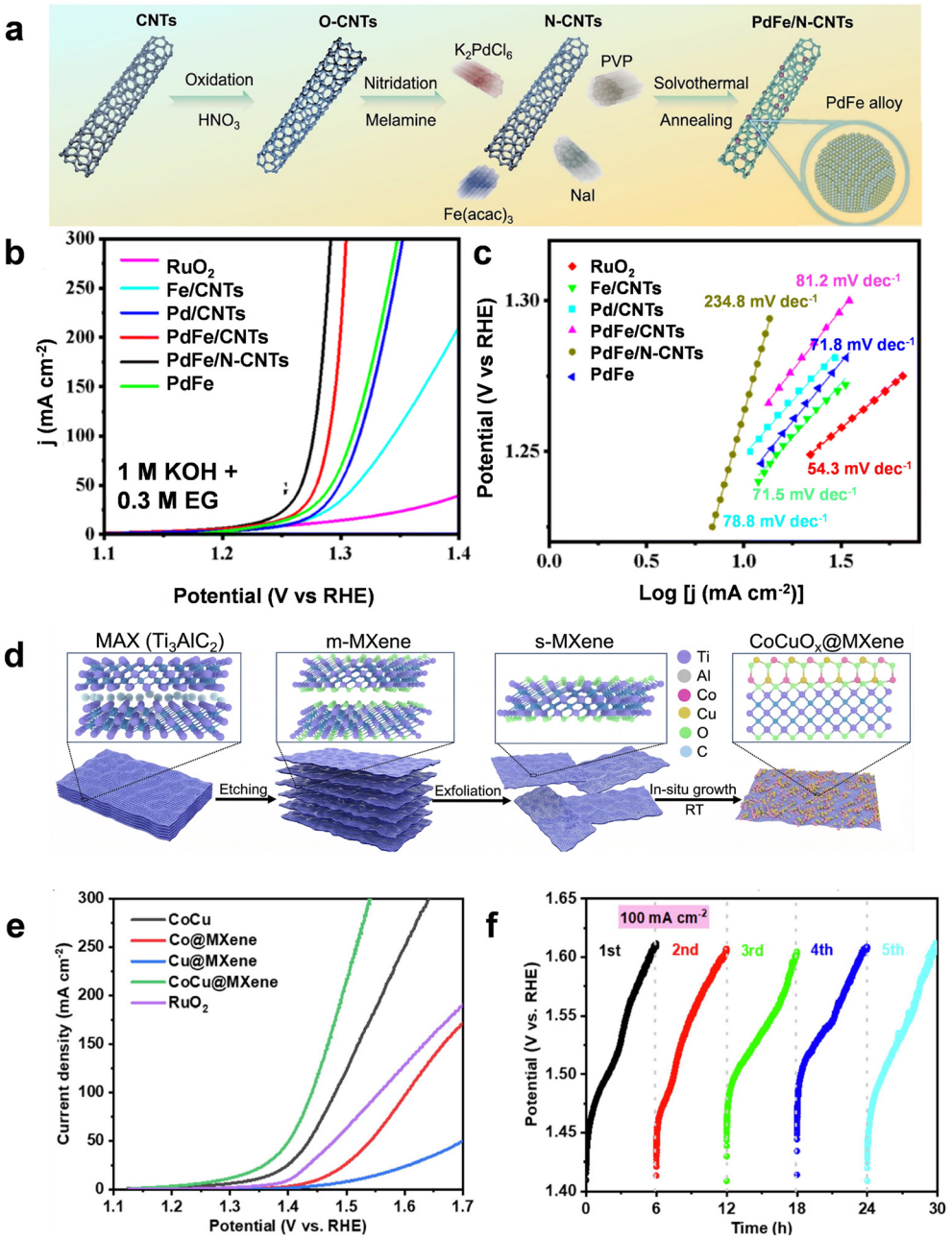

Fig. 9 (a) The preparation of PdFe/N-CNTs; (b) LSV curves of PdFe/N-CNTs, PdFe/CNTs, Pd/CNTs, and Fe/CNTs recorded in 1.0 M KOH with and without 0.3 M EG; (c) corresponding Tafel plots from (b). Reprinted with permission from ref. 97. Copyright 2024, The Royal Society of Chemistry; (d) synthetic scheme of $CoCuO_x$@MXene; (e) EGOR activity of $CoCuO_x$@MXene; (f) stability test of $CoCuO_x$@MXene for the EGOR at 100 mA cm^{-2} over five cycles. Reprinted with permission from ref. 50. Copyright 2025, Elsevier.

low potential of 1.41 V to reach 100 mA cm^{-2} and enables selective conversion of EG derived from PET hydrolysate into formate with a high yield of 87.6%, demonstrating the effectiveness of conductive substrates in improving EGOR performance (Fig. 9d–f).

3.6 Comparison of different catalysts

3.6.1 MOOH phase in different catalysts. Table 1 summarizes the key advantages, limitations, and catalyst design implications of different precursor materials generating the active MOOH phase for the EGOR, including LDHs, oxides, sulfides, selenides, phosphides, phosphates, and MOFs, highlighting how precursor properties influence the electronic structure, defect chemistry, conductivity, and morphology of the reconstructed catalysts, thereby affecting catalytic activity and product selectivity.

Although many transition-metal catalysts reconstruct into MOOH-type active phases under anodic conditions, the precursor materials remain critically important because they

Table 1 Comparison of common precursor catalyst classes generating MOOH-type active phases under anodic conditions

Precursor type	Advantages	Limitations	Design implication
LDHs	Tunable metal composition; abundant OH groups; easy reconstruction to MOOH	Low conductivity	Ideal platform for tuning the electronic structure
Oxides	High structural stability; well-defined crystal facets	Limited conductivity	Suitable for stable catalysts and mechanistic studies
Sulfides/selenides	High intrinsic conductivity; defect-rich reconstructed layers	Possible instability during oxidation	Favor fast kinetics and high current density
Phosphides	Excellent conductivity; conductive core with an active oxyhydroxide shell after reconstruction	Surface oxidation may alter the structure	Efficient charge transfer and high catalytic activity
Phosphates	Strong structural stability; robust frameworks	Low intrinsic conductivity	Stabilize active sites and improve durability
MOFs	Highly tunable porous structures; controllable coordination environments	Stability under anodic conditions can be limited	Enable precise active-site and interface engineering

determine the electronic structure, defect density, conductivity, and morphology of the reconstructed phase. Different precursor classes provide distinct advantages for regulating catalytic activity and reaction pathways. LDHs enable precise tuning of metal composition and facilitate rapid formation of active oxyhydroxide species due to their hydroxyl-rich layered structures, although their relatively low electrical conductivity can limit performance at high current

Table 2 Industrially relevant comparison of catalysts for the EGOR

Catalyst class	Activity	Product selectivity	Stability	Scalability	Material cost	Industrial potential	Key advantages	Limitations
Noble metals	Very high	Tunable C_1/C_2 products	High	Moderate	Very high	Medium	Excellent intrinsic activity and well-defined reaction pathways	High cost and limited abundance
LDHs	High	Mostly C_1	Moderate–high	High	Low	High	Abundant elements, high current density, good catalytic kinetics	Structural reconstruction and possible stability issues
Oxides	Moderate–high	Mainly C_1	High	High	Low	High	Robust structure and good durability	Lower conductivity than sulfides or phosphides
Sulfides/selenides	High	Mostly C_1	Moderate	Moderate–high	Low	Medium–high	High conductivity and fast charge transfer	Possible surface reconstruction and sulfur/selenium leaching
P-compounds/nitrides	High	Mainly C_1	High	High	Low	High	Metallic conductivity and strong structural stability	Mechanistic understanding is still limited
MOF catalysts	Moderate	Mostly C_1	Moderate	Moderate	Moderate	Medium	Tunable structure and high surface area	Limited stability and scalability
Organic catalysts	Low–moderate	Can favor C_2 products	Moderate	High	Very low	Emerging	Metal-free and potentially sustainable	Lower activity and limited studies
Hybrid catalysts	Very high	Tunable C_1/C_2	High	Moderate	Moderate	Very high	Synergistic interfaces enabling high current density and selectivity	Structural complexity and synthesis scalability

densities. Transition-metal oxides generally offer high structural stability and well-defined crystalline structures but often suffer from limited electrical conductivity. Sulfides and selenides typically possess higher intrinsic conductivity and tend to generate defect-rich oxyhydroxide layers during reconstruction, which is beneficial for accelerating reaction kinetics. Metal phosphides exhibit excellent electrical conductivity and can undergo surface oxidation to form highly active oxyhydroxide layers while maintaining conductive cores that facilitate electron transport. In contrast, phosphates usually provide strong structural stability and robust M–O–P frameworks that help stabilize active sites but may exhibit lower intrinsic conductivity. MOFs provide highly tunable porous architectures and coordination environments that enable precise control over active site distribution, although their structural stability under anodic conditions can be limited. Therefore, rational catalyst design should focus not only on the final MOOH active phase but also on selecting precursor materials that effectively regulate the electronic structure, defect chemistry, and transport properties of the reconstructed catalyst.

3.6.2 Performance comparison. Table 2 provides a comparative overview of the major catalyst classes investigated for the EGOR, highlighting their differences in activity, C_1/C_2 product selectivity, stability, scalability, and economic feasibility.

Noble metals such as Pt, Pd, and Au exhibit the highest intrinsic activity and the lowest onset potentials for the EGOR, and their well-defined surface chemistry enables tunable selectivity toward both C_1 and C_2 products. However, their extremely high cost and limited abundance significantly constrain large-scale implementation.

In contrast, transition-metal-based catalysts offer a more favorable balance between performance and cost. LDHs, particularly NiFe and NiCo systems, can deliver high current densities and efficient catalytic kinetics, although structural reconstruction during operation may affect long-term stability. Transition-metal oxides typically exhibit excellent structural robustness and durability, but their relatively low electrical conductivity can limit charge transfer and catalytic rates. Sulfides and selenides provide higher conductivity and faster electron transport, leading to improved catalytic activity; nevertheless, surface reconstruction or possible chalcogen leaching remains a concern. Phosphides and nitrides combine metallic conductivity with strong structural stability, making them promising candidates for high-current operation, although their reaction mechanisms and selectivity control are still not fully understood. Transition-metal-based catalysts generally promote C_1 product formation, although electronic structure tuning may help enhance C_2 selectivity.

MOF-based catalysts represent another emerging class owing to their highly tunable structures and large surface areas, which enable precise control of active sites. However, their moderate activity and limited structural stability currently restrict large-scale applications. Most reported MOF systems still favor C_1 products, and efficient C_2-selective pathways remain rare. Organic catalysts offer the advantage of being metal-free, sustainable, and low-cost, and they can favor the formation of C_2 products. Nevertheless, their

Table 3 Representative electrocatalysts for the EGOR

Catalyst	Electrolyte	Potential (V *vs.* RHE)	j (mA cm^{-2})	Prod.$_{anode}$ (%)	FE$_{anode}$ (%)	Stability	Ref.
Pd–NiTe/NF	1 M KOH	1.35	100	FA	96.5	100% (12 h)	43
mPd$_3$Au/NF	4 M KOH	0.72	—	GA	91.68	—	58
NiFe-LDH/NF	0.5 M CsOH	—	50	FA	105	73% (48 h)	126
CoFe-LDH/NF	1 M KOH	1.44	10	FA (86.01% selectivity)	49.67	—	121
CoNi–OH/CC	1 M KOH	1.3	100	FA	96.5	~82% (50 h)	128
$NiCo_2O_4$	1 M KOH	1.624	100	FA (98.3% selectivity)	98.9	100% (50 h)	138
NiCo–O/NF	1 M KOH	1.35	100	FA	89.6	100% (25 h)	178
$NiCo_2O_4$/NF	1 M KOH	1.34	400	FA	96.7	93% (50 h)	51
B,Co–Ni_3S_2/NF	1 M KOH	1.341	100	FA (>92% selectivity)	>93	39% after 12 h (100 mA cm^{-2})	143
Co,Cl–NiS/NF	1 M KOH	1.50	100	FA (93.9% selectivity)	93.5	~86% (12 h)	145
Ni–Fe_3Se_4	1 M KOH	1.37	100	FA	84	—	147
$NiSe_2$	1 M KOH	1.395	50	FA	80	—	60
CoFe–P/NF	1 M KOH	1.50	100	FA	90	—	150
Fe–Ni_2P/NF	1 M NaOH	1.326	100	FA	—	100% (30 h)	90
Co–Ni_3N/CC	1 M KOH	1.15	—	FA	—	—	120
Pt/MIL-100(Fe)	1 M KOH	−0.25	—	—	—	64.13% (200 CV cycles)	166
TbCo-MOF/NF	1 M KOH	1.39	100	FA	97.3	—	163
Co-polymer/CC	1 M KOH	1.42	10	FA	80		179
TEMPO	1 M KOH	1.53	—	Glycolate	42.88	—	87
AC-400	1.25 M NaOH	—	—	GA	—	—	180
Ni_3S_2@NiFeMn-LDH/NF	1 M KOH	1.5	91.2	FA	90	82% (12 h)	83
Pt/Ni(OH)$_2$	1 M KOH	1.444	1000	FA (90% selectivity)	90	100% (500 h)	89
Ni/Co(OH)$_2$	1 M KOH	1.32	100	FA	80	~100% (10 h)	41
Ni-MOF@MnCo-OH/NF	1 M KOH	1.43	300	FA	~80	—	46
Pd–Ni(OH)$_2$/NF	1 M KOH	1.15	600	GA	>85	~100% (200 h)	174

catalytic activity is generally lower than that of metal-based catalysts, and research in this area remains relatively limited.

Among all catalyst classes, heterojunction or hybrid catalysts show the most promising overall performance. By integrating multiple catalytic components, these systems can generate synergistic interfacial effects that optimize electronic structures, intermediate adsorption, and charge transfer, enabling high activity with tunable C_1/C_2 selectivity, making them promising candidates for future EGOR catalyst design. However, the structural complexity of such catalysts and challenges associated with scalable synthesis remain key issues for future development. Overall, non-noble transition-metal compounds appear to offer the best balance between catalytic activity, cost, and scalability, while heterostructure catalysts represent a major direction for achieving high-performance EGOR systems.

Table 3 compares the reported EGOR performance of representative anodic catalysts discussed above. Most catalyst systems predominantly produce C_1 products, especially FA. High FA selectivity and FE are typically obtained under strongly oxidative conditions, such as high anodic potentials (>1.3 V *vs.* RHE), alkaline electrolytes, and high current densities (100–1000 mA cm^{-2}). These conditions naturally favor deep oxidation and C–C bond cleavage, indicating that the dominance of C_1 products is largely driven by operating conditions rather than intrinsic catalyst selectivity.

In contrast, C_2 products are much less frequently reported and are usually observed under milder potentials, lower current densities, or on noble-metal-based catalysts. This suggests that the C_2-selective EGOR is feasible but is often suppressed under aggressive operating conditions. Importantly, retaining the C_2 carbon backbone leads to higher carbon utilization and lower energy loss, yet this advantage is frequently sacrificed at industrially relevant current densities. In addition, differences in testing protocols and limited stability data make direct comparison across studies difficult. Overall, the results summarized in Table 3 highlight the need to shift EGOR research from maximizing oxidation strength toward controlling reaction depth, enabling more carbon-efficient and scalable C_2-selective pathways.

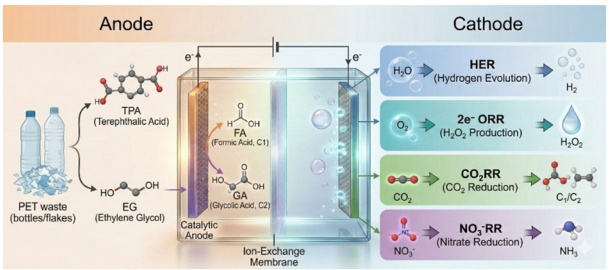

Fig. 10 Integrated electrochemical PET upcycling system. PET is hydrolyzed to TPA and EG, and EG is oxidized at the anode to C_1 or C_2 products. At the cathode, paired reactions, such as the HER, $2e^-$ ORR, CO_2RR, and NO_3^-RR, are employed to enhance energy utilization.

4 Cathodic coupling strategies for the EGOR

Electrochemical systems based on the EGOR can be further improved through rational cathodic coupling strategies. Replacing the conventional OER with the EGOR as the anodic reaction significantly lowers the energy requirement and improves overall energy efficiency. To further enhance energy utilization, the EGOR can be paired with more favorable or value-added cathodic reactions, enabling simultaneous production of valuable products. Typical examples include the HER, $2e^-$ ORR, CO_2RR, and NO_3^-RR. Such paired electrolysis systems allow the upgrading of plastic-waste-derived feedstocks while co-producing energy carriers or valuable chemicals, thereby improving both energy efficiency and economic viability.

The anodic EGOR offers a direct and versatile strategy to generate short-chain acids including FA and GA.[52] However, anodic oxidation operated alone is energetically demanding because the EGOR competes with the OER, which requires high overpotentials (>1.5 V *vs.* RHE) due to sluggish four-electron kinetics. Emerging research demonstrates that the anodic EGOR can be efficiently paired with multiple cathodic reactions to enable dual-production electrolysis (Fig. 10). Improving energy utilization thus requires replacing the OER with a more thermodynamically favorable cathodic pathway that can share charge, lower cell voltage, and simultaneously generate high-value products.

Coupling the EGOR with the HER enables H_2 generation at significantly reduced cell voltage, transforming PET hydrolysate from waste into both an electron donor and a hydrogen source.[89] Besides the HER, the EGOR can also be linked with the $2e^-$ ORR pathway, converting water to H_2O_2 instead of O_2. This route bypasses the high energy barrier of the $4e^-$ OER and generates H_2O_2 as a value-added oxidant, further improving system utility.[124] Furthermore, coupling with the CO_2RR enables simultaneous EGOR and renewable C_1/C_2 chemical production (CO, FA, CH_3OH, acetate),[181] while integration with the NO_3^-RR enables co-production of NH_3 and organic acids, achieving simultaneous carbon and nitrogen valorization.[182] Collectively, the HER, $2e^-$ ORR, CO_2RR, and NO_3^-RR provide diversified paired-electrolysis pathways that reduce energy input compared with the OER, broaden product value, and shift the EGOR toward resource-positive upcycling rather than energy-consuming mineralization.

4.1 Hydrogen evolution reaction

The EGOR can be paired with the HER, offering a more energy-efficient alternative to conventional water splitting. Unlike the OER, which requires >1.5 V, the EGOR proceeds at a much lower onset potential (≈0.6–1.2 V *vs.* RHE),

enabling hydrogen production at reduced cell voltage and lower energy consumption.[131,179] In this configuration, PET-derived EG undergoes anodic α-C–H dehydrogenation, generating electrons that directly drive the HER, while simultaneously forming value-added products such as formate and glycolate instead of waste oxygen.[23] Meanwhile, anodic activation of EG produces aldehyde and carboxyl intermediates without requiring high anodic oxygen evolution kinetics, allowing selective tuning of product distribution by adjusting the potential, pH, or catalyst composition.[183] Ma *et al.* developed Ni–Co_9S_8 NSAs/NF, enabling the conversion of EG into formate through an anodic oxidation-coupled cathodic HER process.[85] The catalyst delivered a formate FE exceeding 90% at a current density of ~130 mA cm^{-2} and maintained stable output under an applied potential of 1.5 V *vs.* RHE, demonstrating

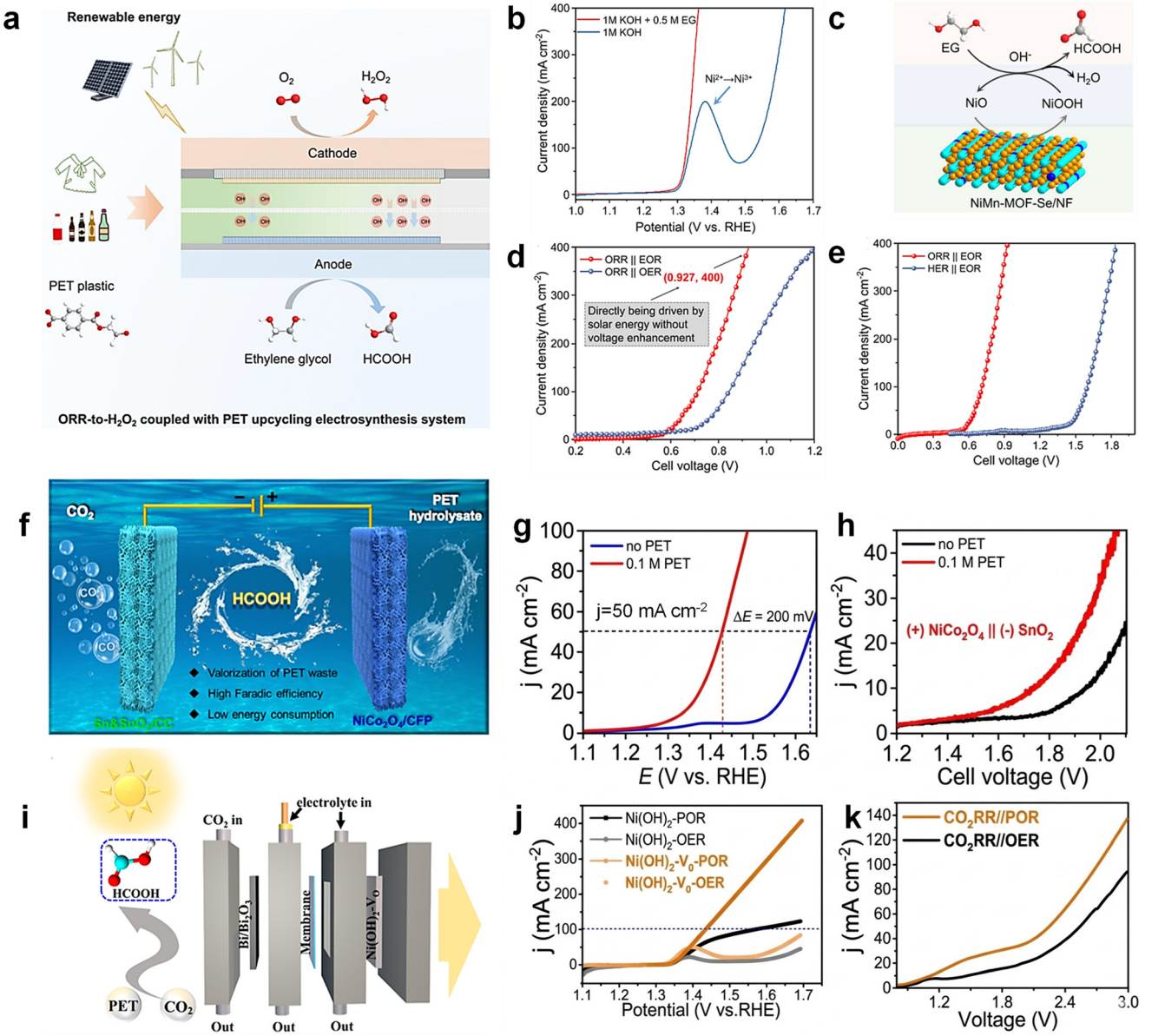

Fig. 11 (a) Scheme of the electrolysis system coupling $2e^-$ ORR-to-H_2O_2 production with the EGOR; (b) LSV comparison of NiMn-MOF-Se/NF in 1.0 M KOH with and without 0.5 M EG; (c) proposed catalytic reaction mechanism for the integrated H_2O_2 synthesis–EGOR process; (d) polarization curves comparing the ORR||EOR with the traditional ORR||OER configuration; (e) polarization curves comparing the ORR||EOR system and HER||EOR system. Reprinted with permission from ref. 185. Copyright 2023, Springer; (f) scheme of the paired electrolysis system enabling simultaneous anodic EGOR and cathodic CO_2 reduction to FA; (g) LSV curves of $NiCo_2O_4$/CFP in 1 M NaOH with and without 0.1 M PET hydrolysate; (h) LSV profiles of the SnO_2||$NiCo_2O_4$ two-electrode configuration with and without the EGOR in the anodic compartment. Reprinted with permission from ref. 191. Copyright 2022, American Chemical Society; (i) scheme of the solar-driven integrated two-electrode flow cell for EGOR–CO_2RR coupling; (j) LSV comparison of $Ni(OH)_2$-V_O and pristine $Ni(OH)_2$ for the EGOR and OER; (k) LSV responses of the integrated reactor with or without the EGOR. Reprinted with permission from ref. 181. Copyright 2023, American Chemical Society.

its strong capability for EGOR–HER integrated upcycling. Xia *et al.* developed bimetallic phosphide@bio-carbon (Fe_2P–Co_2-P@C) for the EGOR coupled with the HER. DFT calculations identified *CHO–CHO as a key intermediate and revealed that the introduction of P promotes the surface reconstruction of transition-metal phosphides, enhancing intermediate adsorption and facilitating the EGOR. Benefiting from the metal–support interface between bimetal phosphides and the bio-carbon framework, the catalyst improves electron transfer and stabilizes reaction intermediates. As a result, the catalyst achieves a highly selective EGOR toward FA with a FE of 99.1% at 1.35 V *vs.* RHE. When coupled with the HER, the EGOR–HER system requires only 1.76 V to reach 500 mA cm^{-2} and maintains stable operation for over 240 h in PET hydrolysate, demonstrating its potential for plastic-waste upcycling and hydrogen production.

The EGOR||HER pairing represents a promising waste-to-energy route, advancing dual-output electrolysis toward carbon circularity and energy efficiency.[174] Liu *et al.* reported an integrated seawater electrolyzer coupled with PET upcycling. In this system, an ultra-low anode potential of 1.15 V *vs.* RHE was sufficient to sustain an industrial-level current density of 600 mA cm^{-2}, which is rarely accessible in conventional water electrolysis systems. As a result, the overall electricity consumption for hydrogen production was dramatically reduced from 4.79 kWh m^{-3} H_2 in a traditional alkaline seawater electrolyzer to 2.45 kWh m^{-3} H_2, corresponding to an energy saving of nearly 50%. This substantial reduction directly originates from replacing the kinetically sluggish OER with the thermodynamically favorable EGOR, which lowers the anodic overpotential and compresses the full-cell voltage window. Importantly, this energy benefit was maintained under long-term operation and high current conditions, demonstrating that the PET-assisted EGOR is not only thermodynamically advantageous but also practically effective for lowering electricity demand in high-throughput hydrogen production systems.

4.2 Oxygen reduction to H_2O_2

The anodic EGOR can also be coupled with the cathodic two-electron reduction of H_2O to H_2O_2, enabling simultaneous production of two value-added oxidation products.[124] Unlike the $4e^-$ H_2O reduction to H_2O, the $2e^-$ pathway forms H_2O_2 at lower overpotential, suppresses electron loss to the HER, and retains more chemical energy on both electrodes.[184] Qi *et al.* reported a waste-to-chemical electrosynthesis route that integrates $2e^-$ ORR-to-H_2O_2 generation with the EGOR.[185] Using a Ni–Mn bimetallic catalyst and onion-like carbon, the paired cell simultaneously catalyzes H_2O_2 formation and the EGOR, achieving FEs of 97.5% (H_2O_2) and 93.0% (formate), respectively. Remarkably, this integrated electrolyzer delivers 400 mA cm^{-2} at only 0.927 V, surpassing all previously reported H_2O_2 electrosynthesis platforms (Fig. 11a and b). Mechanistically, in *in situ* reconstructed NiMn-MOF-Se/NF, Se is replaced by lattice oxygen under anodic polarization to form NiOOH, which adsorbs OH^- and EG through Ni–O coordination. EG undergoes stepwise dehydrogenation and oxidation to aldehyde and carboxyl intermediates, followed by C–C bond cleavage to form formate, which then desorbs into the electrolyte (Fig. 11c). Polarization curves show that the ORR||EOR configuration requires <1.0 V, significantly lower than the ORR||OER system (Fig. 11d). Replacing the ORR with the HER causes the cell voltage to rise by ~0.9 V at both 200 and 400 mA cm^{-2}, confirming the energetic superiority of the ORR-coupled route (Fig. 11e).

Pairing the EGOR with the $2e^-$ ORR not only delivers value-added anodic products but also represents an effective strategy to reduce cell voltage and overall electricity consumption in electrosynthetic systems. A representative example is provided by Sun *et al.* who coupled the EGOR with the $2e^-$ ORR.[124] By replacing the anodic OER with the EGOR, the coupled ORR||EGOR configuration exhibited a substantially reduced cell voltage across a wide current density range. At an industrially relevant current density of −261.7 mA cm^{-2}, the system operated stably at a cell voltage of −1.7 V while simultaneously achieving FEs of 99.83% for H_2O_2 and 97.80% for GA. Quantitative energy analysis further showed that the ORR||EGOR system produced more H_2O_2 per unit electricity input than the conventional ORR||OER configuration (0.240 *vs.* 0.226 g kWh^{-1}), directly demonstrating improved electrical energy utilization. Importantly, energy savings originate from both the lower thermodynamic potential of the EGOR compared to the OER and the kinetic acceleration enabled by favorable organic oxidation pathways.

4.3 CO_2 reduction reaction

While the EGOR–HER coupling enables low-voltage hydrogen production, the cathodic pathway is often dominated by the HER, resulting in a single product stream and limited value escalation. In contrast, pairing the EGOR with the CO_2 reduction reaction (CO_2RR) unlocks a more advanced carbon-utilization route.[186,187] Electrons released from the EGOR can drive CO_2 conversion to CO, formate, methanol or multi-electron C_2 oxygenates at lowered overpotential.[188] Importantly, the lower anodic potential of the EGOR suppresses the competitive HER at the cathode, significantly improving CO_2RR selectivity. Coupling the EGOR with the cathodic CO_2RR enables the simultaneous generation of value-added formate at both the anode and the cathode.[189,190]

Wang *et al.* integrated the EGOR with CO_2 reduction in a paired electrolyzer, achieving a remarkably low operational cell voltage of 1.55 V to simultaneously drive the two half-reactions.[191] Under a higher applied voltage of 1.90 V, the system delivered an outstanding 155% FE toward FA, indicating effective electron reuse and product crossover enhancement within the coupled EGOR–CO_2 conversion process (Fig. 11f–h). Ma *et al.* demonstrated that $Ni(OH)_2$-V_O and Bi/Bi_2O_3 catalysts deliver remarkable HCOOH selectivity

(86% and 91%) while sustaining industrial-level current densities at ultralow cell potentials of 300 mA cm^{-2} at 1.6 V and −272 mA cm^{-2} at −1.4 V, respectively (Fig. 11i–k).[181]

EGOR–CO_2RR paired electrolysis also offers a highly effective pathway to reduce electricity consumption while enhancing the overall techno-economic viability of electrochemical plastic upcycling systems.[186,192] Yu *et al.* demonstrated that replacing the anodic OER with the EGOR in a PET upcycling-assisted electrolysis system substantially improved overall process efficiency.[187] Specifically, the introduction of the EGOR led to a 51.3% increase in FA productivity, while simultaneously achieving a 46.3% reduction in energy consumption compared with the conventional OER-coupled system.

4.4 Nitrate reduction reaction

Compared with the HER, $2e^-$ ORR, and CO_2RR-coupled configurations, integrating the anodic EGOR with the cathodic NO_3^-RR offers a dual-resource upgrading pathway that simultaneously enables carbon upcycling from PET-derived EG and nitrogen remediation, while producing high-value NH_3.[82] Furthermore, converting nitrate into NH_3 not only mitigates water pollution but also transforms a harmful contaminant into a commercially valuable nitrogen product.[82,193] Thermodynamically, nitrate-to-NH_3 conversion is more favorable than N_2 reduction and often more economically rewarding than the HER.[55,80] Within an EGOR||NO_3^-RR paired system, PET-derived EG undergoes selective anodic oxidation to formate, acetate, and glycolate, while nitrate acts as the terminal electron acceptor at the cathode. For example, Ren *et al.* reported a co-production system that couples nitrate reduction with the EGOR to simultaneously generate NH_3 and GA.[27] In this configuration, low-crystalline CoOOH supported on carbon foam (LCCoOOH/CF) serves as the cathode, while Pd nanothorns grown on NF (Pd NTs/NF) function as the anode. The paired electrolyzer enables NH_3 and GA co-production at an ultralow onset voltage of only 0.5 V, significantly lower than the ~1.4 V typically required for standalone nitrate electrolysis (Fig. 12a and b). Wang *et al.*

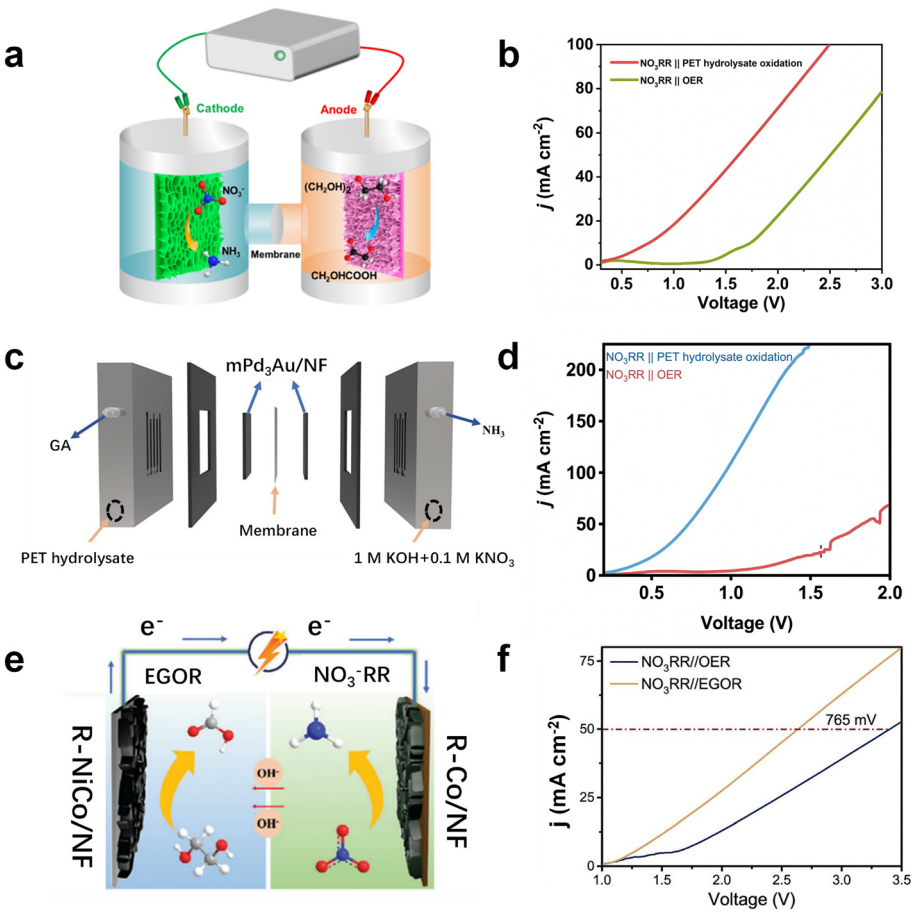

Fig. 12 (a) Scheme of the integrated system enabling co-production of GA and NH_3; (b) LSV comparison of LC-CoOOH/CF (cathode) and Pd NTs/NF (anode) under (−)NO_3^-RR||EGOR(+) and (−)NO_3^-RR||OER(+) conditions. Reprinted with permission from ref. 27. Copyright 2023, American Chemical Society; (c) scheme of a two-electrode MEA flow electrolyzer designed for simultaneous NH_3 and GA production; (d) LSV curves of mPd_3Au/NF operated in NO_3^-RR||EGOR and NO_3^-RR||OER systems. Reprinted with permission from ref. 58. Copyright 2024, Wiley; (e) scheme of the electrocatalytic configuration coupling NO_3^-RR with the EGOR; (f) LSV curves of (−)NO_3^-RR||EGOR(+) and (−)NO_3^-RR||OER(+) using an R-Co/CF||R-NiCo/NF paired electrode setup. Reprinted with permission from ref. 193. Copyright 2025, Wiley.

reported a co-production system that electrochemically upgrades nitrate and PET plastics to NH_3 and GA using a mesoporous Pd_3Au film supported on NF (mPd_3Au/NF).[58] The catalyst delivers remarkable FEs of 97.28% for NH_3 and 95.32% for GA at 0.9 V. Moreover, the NO_3^-RR||PET-hydrolysate-oxidation configuration achieves significantly higher current density than the conventional NO_3^-RR||OER system, underscoring the energetic and kinetic advantages of coupling the EGOR with nitrate reduction (Fig. 12c and d).

Coupling the EGOR with the NO_3^-RR offers a clear energy-saving advantage by replacing the kinetically sluggish OER with a lower-potential anodic oxidation process, thereby significantly reducing the overall cell voltage and electricity consumption.[194] The NO_3^-RR is particularly attractive due to its low onset potential (−0.2 to −0.5 V *vs.* RHE), meaning that the reaction can operate at significantly lower cell voltages than OER-coupled systems.[27,58] For example, Wang *et al.* developed a paired electrocatalytic system that co-produces NH_3 and FA by coupling nitrate reduction on a reconstructed Co-modified copper foam cathode (R-Co/CF) with the EGOR on reconstructed NiCo-modified NF (R-NiCo/NF).[193] The device delivers excellent FE (96.2% for NH_3 and 98.2% for FA) highlighting an effective dual-product conversion route for PET-derived carbon streams. Compared with the conventional NO_3^-RR||OER configuration, the NO_3^-RR||EGOR system exhibits markedly lower onset potential and higher current density, consistent with the more favorable anodic thermodynamics of the EGOR relative to the OER (Fig. 12e and f).

Based on the discussion above, recent studies have shown that pairing the EGOR with cathodic reactions can lower cell voltage and enable co-production of valuable products such as H_2, H_2O_2, CO, and NH_3. However, most current studies still focus mainly on reducing voltage. In practice, low voltage does not always mean low energy cost. The real metric should be electricity consumption per unit product. Cathodic selectivity, mass transport of nitrate or oxygen, and side reactions such as the HER can strongly affect the true energy efficiency, even when polarization curves look favorable. Another important issue is product and ion crossover between the anode and cathode. In some paired systems, crossover can artificially increase apparent FE, such as formate yields exceeding 100%. This does not reflect true electrochemical conversion and may create serious challenges for downstream separation. Future studies should clearly separate electrochemical formation from crossover effects using carbon and nitrogen mass balances. More importantly, paired electrolysis should move from simple reaction matching to system-level design. The cathodic reaction should be selected based on pH compatibility, membrane stability, product separation feasibility, and kinetic matching at high current density. For example, NO_3^-RR||EGOR systems are attractive for waste treatment, but their practical value depends on stable nitrogen selectivity and efficient NH_3 recovery under realistic conditions. Similarly, EGOR–H_2O_2 systems are often limited by peroxide stability and oxygen transport rather than reaction thermodynamics. Overall, future progress should focus less on achieving the lowest voltage and more on integrated performance, including energy consumption per product, single-pass conversion, separation cost, and long-term stability. Only with such metrics can EGOR paired electrolysis move from laboratory demonstrations toward practical implementation.

4.5 Performance comparison in EGOR-coupled electrolysis

Table 4 summarizes the main cathodic coupling strategies for the EGOR and compares their activity, selectivity, energy efficiency, and potential for practical application. Overall, each coupling pathway targets different products and applications, resulting in distinct advantages and limitations. Among them, the EGOR–HER is currently the most mature and industrially feasible configuration. The HER has fast kinetics and well-established catalysts, enabling high current densities and efficient hydrogen production. In addition, replacing the OER with the EGOR significantly lowers the cell voltage, improving energy efficiency in electrolysis systems. In contrast, the EGOR–2e$^-$ ORR enables the co-production of H_2O_2 and EGOR products, offering a promising route for decentralized H_2O_2 synthesis. However, achieving high selectivity toward the two-electron pathway remains challenging. More complex systems such as the EGOR–CO_2-RR and EGOR–NO_3^-RR provide opportunities for integrated carbon utilization or wastewater treatment, but their practical application is still limited by slower reaction kinetics and system complexity. Overall, the EGOR–HER currently offers the best balance of activity, energy efficiency, and scalability,

Table 4 Comparison of EGOR-cathodic coupling strategies in paired electrolysis systems

Coupling strategy	Main products	Kinetics	Selectivity	Energy efficiency	Industrial feasibility	Overall potential
EGOR||HER	H_2 + FA/GA	High	High for H_2	High	High	Most promising for practical implementation
EGOR||2e$^-$ ORR	H_2O_2 + FA/GA	Moderate–high	High for H_2O_2 with selective catalysts	Moderate–high	Medium	Promising for decentralized H_2O_2 production
EGOR||CO_2RR	CO + FA/GA	Moderate	Tunable depending on the catalyst	Moderate	Low–medium	Attractive for carbon utilization but still early-stage
EGOR||NO_3^-RR	NH_3 + FA/GA	Moderate	Moderate–high	Moderate	Medium	Promising for wastewater treatment and ammonia synthesis

Table 5 Electrocatalytic upcycling of the EGOR *via* anodic oxidation coupled with energy-saving cathodic reactions

Anode	Electrolyte	Potential (V *vs.* RHE)	j (mA cm^{-2})	Prod.$_{anode}$	FE$_{anode}$ (%)	Cathode	Coupling	Prod.$_{cathode}$	FE$_{cathode}$ (%)	Ref.
Ni–Co_9S_8 NSAs/NF	1 M KOH	1.5	≈140	FA	≈92	Pt wire	HER	H_2	≈100	85
$NiSe_2$/GC	1 M KOH	1.395	50	FA	>80	Pt wire	HER	H_2	≈100	60
CuO/Cu	1 M KOH	1.45	10	FA	88	Pt gauze	HER	H_2	≈100	195
Au/$Ni(OH)_2$	1 M KOH	1.7	—	GA	97.8	Ni-SAC	2e$^-$ ORR	H_2O_2	99.83	124
Co_3O_4/NF	1 M KOH	2.13	16	FA	80	Mo_2N–Co_3O_4@Fe_2O_3/PVDF/NF	2e$^-$ ORR	H_2O_2	~ 80	184
NiMn-MOF-Se/NF	1 M KOH	1.362	400	FA	>90	B/N–onion carbon	2e$^-$ ORR	H_2O_2	97.5	185
NiOOH/NF	1 M KOH	1.8	20	FA	>88	Bi_2O_3/CP	CO_2RR	FA	>90	186
$NiCo_2O_4$/NF	1 M KOH	1.5	250	FA	90	BiOI-C	CO_2RR	FA	90	189
$NiCo_2O_4$/CFP	1 M NaOH	1.45	20	FA	~90	SnO_2/CC	CO_2RR	FA	70	191
Pd NTs/NF	1 M KOH	0.774	—	GA	87.87	LC-CoOOH/CF	NO_3^-RR	NH_3	97.38	27
Ru–Co_3O_4/NF	3 M KOH	1.34	200	FA	99	Ru–Co_3O_4/NF	NO_3^-RR	NH_3	98.5	82
R-NiCo/NF	1 M KOH	1.45	50	FA	98.2	R-Co/CF	NO_3^-RR	NH_3	96.2	193

while other coupling strategies remain promising but require further catalyst and system optimization.

Table 5 summarizes recent results of electrochemical PET upcycling *via* the EGOR coupled with energy-saving cathodic reactions. Overall, most systems still favor C_1 products at the anode, while pairing with the HER, 2e$^-$ ORR, CO_2RR, or NO_3^-RR at the cathode to reduce overall cell voltage. High FEs are frequently reported on both electrodes, demonstrating the technical feasibility of paired electrolysis. However, a closer comparison reveals several important limitations.

First, many reported systems operate at relatively high anodic potential (often >1.5 V *vs.* RHE) or modest current densities, which raises concerns regarding energy efficiency and scalability. In several cases, high selectivity is achieved under conditions that are not directly comparable, making performance benchmarking difficult. Second, although paired reactions such as the 2e$^-$ ORR and NO_3^-RR improve energy utilization, the choice of cathodic reactions remains limited, and product compatibility and downstream separation are rarely discussed. Third, while a few studies demonstrate GA formation, C_2-selective systems are clearly underrepresented, indicating that maintaining C_2 selectivity under practical current densities remains challenging. Finally, most studies rely on alkaline electrolytes and clean

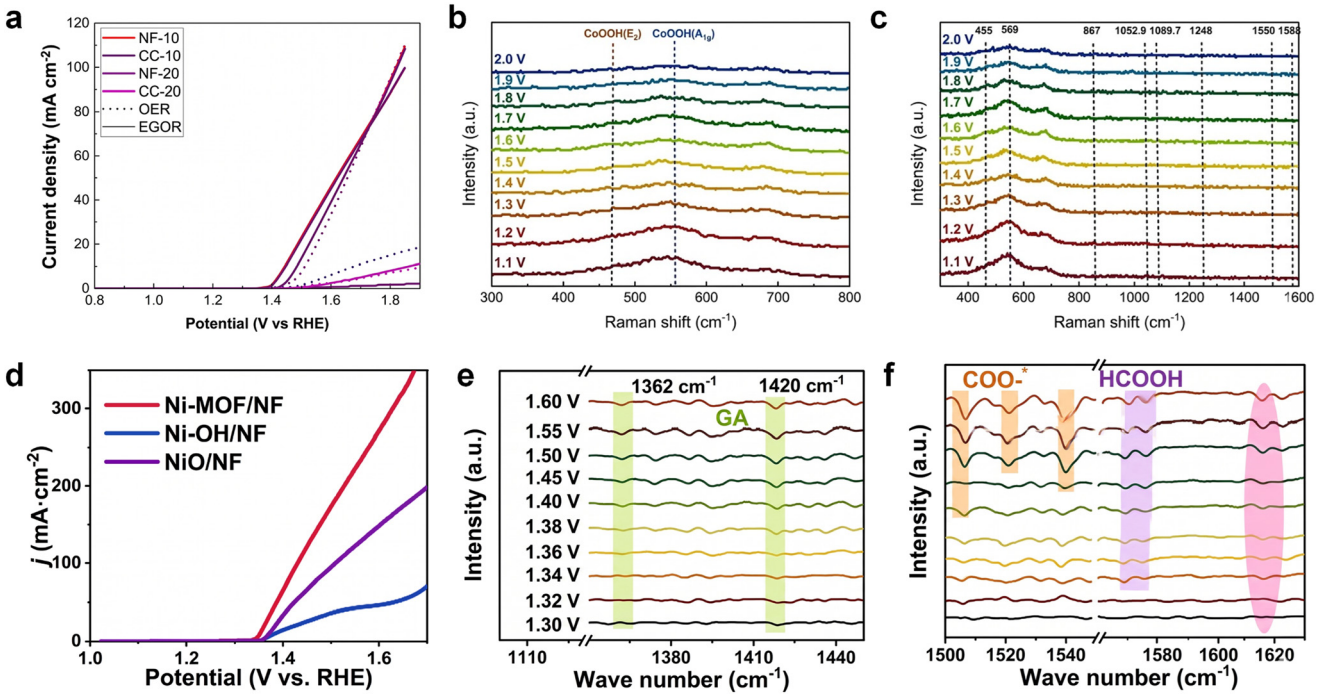

Fig. 13 (a) LSV curves in 1 M KOH (±0.1 M EG); *in situ* Raman spectra of the EGOR (b) in the 300–800 cm^{-1} range and (c) in the 300–1600 cm^{-1} range at different potentials of NF-10. Reprinted with permission from ref. 121. Copyright 2025, Elsevier; (d) the EGOR activity of Ni-MOF/NF, Ni-OH/NF, and NiO/NF; (e) *in situ* FTIR spectra of Ni-MOF at various potentials in 1 M KOH with 0.1 M EG, covering 1100–1450 cm^{-1}; (f) FTIR spectra in the higher wavenumber range of 1500–1630 cm^{-1}. Reprinted with permission from ref. 46. Copyright 2024, Elsevier.

model feeds, with limited assessment of long-term stability under realistic operating conditions. Overall, Table 5 not only highlights clear progress in paired electrolysis for PET upcycling but also underscores the need for lower-potential operation, improved C_2 selectivity, standardized testing conditions, and system-level evaluation to enable meaningful comparison and practical translation.

5 Mechanism analysis for the EGOR

5.1 Mechanism characterization

5.1.1 Raman. *In situ* spectroscopic techniques play a central role in elucidating the reaction mechanism of the EGOR, providing molecular-level insight.[60,196] *In situ* Raman spectroscopy is particularly powerful for monitoring catalyst surface reconstruction and intermediate evolution under applied potential. During the EGOR, Raman can directly capture the formation of high-valent MOOH species through characteristic E_g and A_{1g} vibrational modes, indicating the activation of transition-metal sites (*e.g.*, CoOOH, NiOOH).[40] Simultaneously, Raman allows the real-time observation of the gradual disappearance of EG-related bands (C–H or C–O stretching features) as the reactant is consumed. More importantly, the emergence of new Raman bands associated with key carbon-containing intermediates, such as glycolate, 2-hydroxyacetyl, or adsorbed *COO^-, provides solid evidence of C–H activation, C–C cleavage, and the formation of C_1/C_2 oxidation products. Zhang *et al.* prepared a non-noble CoFe-LDH catalyst through electrodeposition, achieving an active CoFe-LDH/NF-10 min material for selectively converting PET-derived EG into formate.[121] To elucidate its reaction mechanism, *in situ* electrochemical Raman spectroscopy was employed. As the applied potential exceeded 1.30 V *vs.* RHE, vibrational features at 458 and 569 cm^{-1} appeared, corresponding to the E_g and A_{1g} modes of activated CoOOH, confirming the formation of high-valent CoOOH as the key oxidizing species. Meanwhile, the organic Raman bands of EG (≈867, 1053, and 1090 cm^{-1}) gradually diminished and disappeared above 1.70 V, indicating consumption of the reactant. At higher potentials, new bands emerged at 1550 cm^{-1} (symmetric O–C–O of *HCOO), 1248 cm^{-1} (C–H twisting of glycolate), and 1585 cm^{-1} (C═O of glycolate), directly evidencing the formation of formate and glycolate. These spectral evolutions clearly reveal a pathway in which CoOOH drives the EGOR, suppresses side products, and promotes selective C–C cleavage toward formate (Fig. 13a–c).

5.1.2 IR. Complementing Raman, *in situ* infrared spectroscopy/Fourier transform infrared spectroscopy (IR/FTIR) offers high sensitivity to functional groups such as C═O, C–O, and COO^-, enabling precise identification of reaction intermediates and products.[89,152] FTIR can track the growth of characteristic bands: GA (~1360–1420 cm^{-1}), formate (~1350–1388 and ~1585 cm^{-1}), glycolate (~1240 and 1580 cm^{-1}), and adsorbed *COO^- species that appear at higher potentials and signify deep oxidation pathways. The potential-dependent evolution of these IR signatures allows direct mapping of product selectivity and kinetic onset potential. For example, Li *et al.* investigated Ni-MOF@MnCo–OH for the EGOR using *in situ* FTIR spectroscopy to clarify its reaction pathway.[46] The spectra reveal characteristic bands at 1362 and 1420 cm^{-1} that increase with potential, confirming GA as a key intermediate. In the higher-wavenumber region, the growth of the 1577 cm^{-1} COO^- band indicates formate formation, while additional peaks at 1511, 1519, and 1541 cm^{-1} above 1.50 V correspond to adsorbed COO* species involved in deeper oxidation. A distinct feature at 1620 cm^{-1} further identifies 2-hydroxyacetyl as an important intermediate. Together, these observations outline a sequential EGOR pathway from GA to formate, followed by the emergence of high-potential oxidation intermediates (Fig. 13d–f).

5.1.3 EPR. In EGOR research, understanding the reaction mechanism and identifying reactive intermediates are essential for explaining catalytic activity enhancement.[176] Among the available characterization techniques, electron paramagnetic resonance (EPR) spectroscopy is particularly powerful for detecting short-lived radical species generated during electrochemical reactions.[116,197] By using spin-trapping agents, EPR can capture transient radicals and provide direct evidence of reactive oxygen species involved in the catalytic process.[82] For example, Chang *et al.* employed EPR with DMPO as a spin-trapping agent to investigate the catalytic behavior of PdNi/NF during the EGOR.[183] The characteristic DMPO–·OH signal confirmed the generation of ·OH radicals under electrochemical operation, and the signal intensity decreased after the addition of EG, indicating that these radicals were partially consumed during the EGOR. These results demonstrate that EPR can reveal key reaction intermediates and help elucidate how catalyst modification promotes EGOR activity and reaction pathways. Lu *et al.* compared the generation of reactive oxygen species during the EGOR using quasi *in situ* EPR with DMPO as the spin-trapping agent.[198] The characteristic quartet signal of DMPO–·OH (1 : 2 : 2 : 1) is observed for all catalysts, confirming the formation of ·OH radicals under electrochemical conditions. Notably, PtPd–$Ni(OH)_2$ exhibits a significantly stronger DMPO–·OH signal than Pd–$Ni(OH)_2$ and Pt–$Ni(OH)_2$, indicating that the alloyed catalyst promotes the generation of more active ·OH species, which plays a key role in accelerating the EGOR.

5.1.4 XPS. X-ray photoelectron spectroscopy (XPS) is widely employed to probe the surface chemical states and electronic structures of electrocatalysts, providing crucial insights into catalytic mechanisms during the EGOR.[110] By analyzing the binding energies of core-level electrons, XPS can reveal variations in metal valence states, surface oxidation, and the interaction between catalyst components.[124,184] For instance, the deconvolution of O 1s spectra often distinguishes lattice oxygen and adsorbed oxygen species, which are closely related to the adsorption and activation of OH^- in alkaline media.[139] A higher proportion of surface adsorbed oxygen typically indicates enhanced formation of reactive *OH intermediates, facilitating the oxidation of EG and the removal of poisoning

intermediates on the catalyst surface. In addition, shifts in metal core-level peaks can reflect electronic interactions induced by alloying or heterostructure construction, which modulate adsorption energies of key intermediates and ultimately influence EGOR activity and stability.[84,178] Therefore, XPS analysis provides essential evidence for understanding how catalyst composition and surface chemistry regulate the reaction pathway and catalytic performance.

Lu *et al.* investigated the surface oxygen species of different catalysts using O 1s XPS spectroscopy.[198] The increased adsorbed oxygen indicates stronger adsorption and activation of OH^- species on the catalyst surface. This facilitates the formation of active OH species, which are crucial for the EGOR and for preventing catalyst poisoning by CO intermediates, thereby enhancing EGOR activity. Liu *et al.* used high-resolution XPS to probe the interfacial electronic interaction in Pd–$Ni(OH)_2$.[174] In the Pd 3d spectra, the Pd 3d peaks of Pd–$Ni(OH)_2$ shift positively by about 0.2 eV relative to metallic Pd, indicating decreased electron density on Pd due to electron transfer from Pd to $Ni(OH)_2$. In the O 1s spectra, besides the signals assigned to adsorbed H_2O and O–$Ni(OH)_2$, a new peak at 530.2 eV appears in Pd–$Ni(OH)_2$, which is attributed to lattice oxygen in the Pd–O–Ni bond, directly evidencing the formation of an interfacial Pd–O–Ni linkage. These results confirm strong electronic coupling between Pd and $Ni(OH)_2$, which downshifts the Pd d-band center, weakens the adsorption of poisoning carbonyl species, and thereby improves the activity, selectivity, and stability of the EGOR.

5.1.5 XAS. X-ray absorption spectroscopy (XAS) can also be used to probe the electronic structure and local coordination environment of electrocatalysts under reaction conditions, providing important insights into the mechanism of the EGOR.[86,144] In particular, XANES can reveal changes in the oxidation state and electronic structure of active metal centers, while EXAFS provides information on the local atomic coordination and bond distances during the reaction.[47,185] These analyses enable the identification of dynamic structural transformations, such as metal oxidation, reconstruction, or the formation of metal–oxygen species under operating potentials.[49] For example, the emergence of metal–O coordination signals or variations in white-line intensity often indicate the formation of surface oxyhydroxide species, which are widely considered active phases for alcohol oxidation.[149,199] In addition, O K-edge SXAS can be used to evaluate the degree of transition metal–oxygen covalency through the hybridization between metal 3d and O 2p orbitals, which has been proposed as a key descriptor correlating the catalyst structure with alcohol oxidation activity.[124,189] Therefore, XAS provides direct evidence linking electronic structure evolution to catalytic performance, offering a critical mechanistic understanding of how catalyst modification enhances EGOR activity and stability.

Kang *et al.* employed O K-edge SXAS spectroscopy to investigate the electronic structure modulation induced by oxygen vacancies in Co_3O_4.[200] The integrated pre-edge intensity of V_O-Co_3O_4 reaches approximately 50%, which is significantly higher than that of pristine Co_3O_4 (15%). This result indicates stronger Co 3d–O 2p hybridization and enhanced TM–O covalency, suggesting that oxygen vacancies promote electron delocalization and improve the electronic conductivity and catalytic activity for alcohol oxidation. Zhao *et al.* employed *in situ* XAS to monitor the structural and electronic changes of Pd catalysts during the EGOR. The Pd K-edge XANES spectra collected at +1.23 V exhibit a higher white-line intensity compared with those at +0.33 V, indicating that the Pd surface becomes more oxidized under EGOR conditions.[91] Meanwhile, the EXAFS spectra reveal the emergence and enhancement of the Pd–O coordination signal, confirming the formation of surface Pd–O species during the reaction. These results demonstrate that XAS can directly track the oxidation state and coordination environment of active sites under operating conditions, providing crucial evidence that surface oxidation of Pd occurs during the EGOR and contributes to catalyst deactivation.

5.2 Theoretical calculation

5.2.1 Adsorption energy. In DFT calculations, adsorption energy quantifies the thermodynamic favorability of binding by comparing the total energy of the adsorbate–catalyst system with the energies of the isolated catalyst and free molecule.[89] A more negative adsorption energy indicates stronger binding, which is generally associated with more efficient activation of the reactant. For PET-derived EG, calculating the adsorption energies of key species such as EG, *OH, and dehydrogenated intermediates helps reveal how the surface electronic structure, coordination environment, and active-site composition govern catalytic performance. Adsorption energetics determine whether EG can be effectively anchored, dehydrogenated, and converted along the desired C_2 or C_1 oxidation pathways, while simultaneously influencing resistance to over-oxidation or surface poisoning.[201]

For example, Tu *et al.* developed self-supporting CuPd alloy nanosheets as bifunctional catalysts for electrooxidizing PET-derived EG to GA and for NO_3^-RR. DFT calculations show that EG binds more strongly to CuPd/NF (−1.42 eV) than to Pd/NF (−1.01 eV), indicating enhanced EG activation. In contrast, GA desorbs more readily from CuPd/NF (0.11 eV) than from Pd/NF (0.40 eV), demonstrating that Cu incorporation facilitates product release and prevents over-oxidation. Ying *et al.* designed a heterostructure Fe_3O_4–$NiCo_2O_4$ catalyst for the selective electrooxidation of PET-derived EG.[88] DFT calculations show that Fe incorporation dramatically strengthens EG adsorption on Ni sites, with the binding energy increasing from −0.98 eV to −2.72 eV. *OH adsorption is similarly enhanced, shifting from a weak endergonic +0.67 eV to a strongly exergonic −2.79 eV after Fe integration. This simultaneous strengthening of EG and *OH adsorption indicates improved co-adsorption and synergistic activation of the key EGOR intermediates. Liu

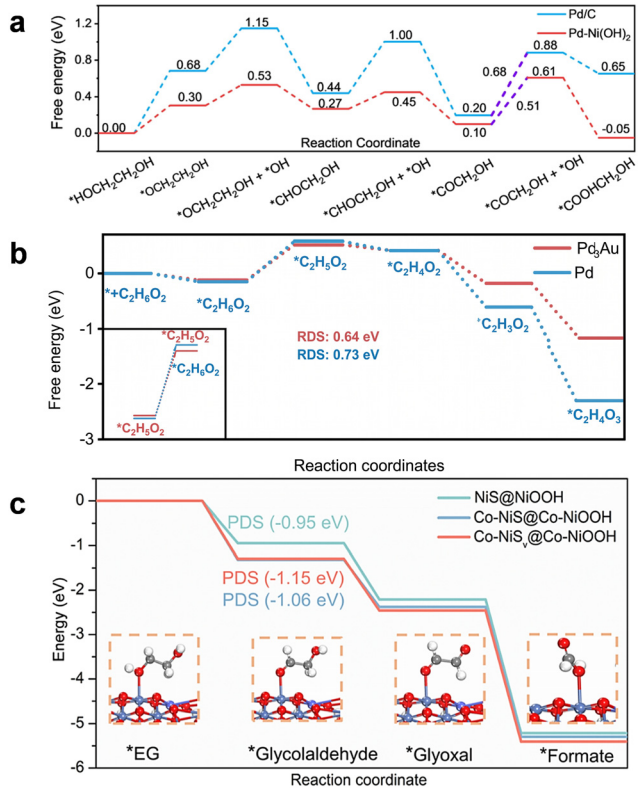

Fig. 14 (a) Gibbs free-energy diagrams for EG-to-GA oxidation on Pd and Pd–Ni(OH)$_2$, with all labeled values representing Gibbs free energies in eV. Reprinted with permission from ref. 174. Copyright 2023, Wiley; (b) Gibbs free-energy diagrams for the EG-to-GA conversion pathway on $Pd_3Au(111)$ and Pd(111) active sites. Reprinted with permission from ref. 58. Copyright 2024, Wiley; (c) Gibbs free-energy profiles for the EGOR on NiS@NiOOH, Co-NiS@Co-NiOOH, and Co-NiS_v@Co-NiOOH at zero potential to form FA. Reprinted with permission from ref. 145. Copyright 2023, Springer.

et al. developed a bifunctional Co–Ni_3N nanosheet catalyst for the EGOR with the HER.[120] DFT calculations show that Co–Ni_3N exhibits a more negative H_2O adsorption energy (−0.32 eV) than Ni_3N, indicating stronger water activation for hydrogen evolution. Likewise, its more negative EG adsorption energy (−0.52 eV *vs.* −0.42 eV for Ni_3N) confirms enhanced EG binding essential for the EGOR.

5.2.2 Energy diagram for EG decomposition pathways. The electrochemical degradation of PET-derived EG can be fundamentally understood by analyzing its Gibbs free-energy diagram along the reaction coordinate.[148,180,201] Theoretical studies show that the EGOR generally proceeds through a sequence of dehydrogenation and deprotonation steps, beginning with the adsorption of EG on the catalyst surface followed by the formation of several oxygenated products.[85,138] The overall shape of the free-energy profile determines whether the reaction preferentially yields C_2 products or undergoes further C–C bond cleavage to form C_1 products.[152,165,174] By analyzing changes in ΔG across each step of the pathway, this approach offers essential guidance for designing catalysts capable of promoting efficient, selective, and energy-favorable electrochemical upcycling of PET-derived EG.

Liu *et al.* employed a Pd–Ni(OH)$_2$ catalyst to electro-oxidize PET-derived EG into GA.[174] Gibbs free-energy profiles for the EG → GA pathway on Pd and Pd–Ni (OH)$_2$ were calculated. The entire energy landscape on Pd–Ni(OH)$_2$ lies below that on pure Pd on Pd–Ni(OH)$_2$ has a free-energy change of 0.51 eV, significantly lower than the 0.68 eV barrier on Pd, indicating that the Ni(OH)$_2$ more easily oxidizes OH^- to *OH, which then efficiently converts the key *CO–CH_2OH intermediate to GA. The final GA-related state on Pd–Ni(OH)$_2$ is slightly exergonic (≈ −0.05 eV), showing that product formation is thermodynamically favored (Fig. 14a). Wang *et al.* developed a mesoporous Pd_3Au film supported on NF to enable the EGOR into GA.[58] The mechanism consists of three sequential deprotonation steps (*$HOCH_2$–CH_2OH → *OCH_2–CH_2OH → *OCH–CH_2OH → *OC–CH_2OH → GA), with the first deprotonation identified as the rate-determining step (RDS) on both $Pd_3Au(111)$ and Pd(111). Importantly, the free-energy barrier on $Pd_3Au(111)$ is only 0.64 eV, lower than the 0.73 eV barrier on Pd(111), indicating that the Pd–Au ensemble more effectively activates EG for GA formation (Fig. 14b). Chen *et al.* designed a Co,Cl–Ni_3S_2 catalyst for the EGOR to formate and H_2 generation.[145] Free-energy calculations show that all EGOR steps are downhill on NiS@NiOOH, Co-NiS@Co-NiOOH, and Co-NiS_v@Co-NiOOH surfaces. Co-NiS_v@Co-NiOOH exhibits the most exergonic PDS (−1.15 eV), accounting for its superior catalytic activity (Fig. 14c).

6 Challenges and perspectives

Despite rapid advances in the EGOR for PET upcycling, several fundamental and technological challenges continue to constrain performance. At the molecular level, precise control over whether EG is converted into C_1 or C_2 products remains elusive, as product selectivity is dictated not only by applied potential but also by coupled effects of the surface electronic structure, defect chemistry, and the adsorption energetics of key intermediates. In parallel, many state-of-the-art catalysts undergo substantial structural reconstruction under operating conditions, but dynamic evolution and true active sites are still poorly understood. On the cathode side, only a limited set of paired reactions (HER, 2e$^-$ ORR, CO_2RR, and NO_3^-RR) has been experimentally coupled with the EGOR, thereby restricting the diversity of co-products and the flexibility of overall cell energetics. From a system perspective, most studies remain confined to lab-scale reactors with suboptimal mass transport, modest current densities, and limited consideration of membrane selection, gas–liquid interface regulation, and long-term operational stability, collectively impeding translation toward practical deployment. Moreover, meaningful cross-study comparison is hampered by the widespread use of disparate testing conditions, including electrolyte pH, PET or EG concentration, temperature, and reactor configuration; the establishment of standardized testing protocols would represent an important step toward benchmarking catalyst

performance and accelerating rational design across the field. Besides electrochemical performance, downstream product separation has received little attention, particularly in paired systems that generate liquid products on both electrodes, where separation complexity may dominate overall process cost and energy demand. Moreover, most studies rely on pure EG or clean PET hydrolysates, overlooking the impurity tolerance required for realistic PET waste streams containing dyes, additives, and polymer residues that may induce catalyst poisoning or performance decay. Therefore, the following sections outline future research directions for PET upcycling (Fig. 15).

6.1 Fundamental control of C_1/C_2 selectivity

Product selectivity cannot be dictated by applied potential alone but instead emerges from a complex interplay among the surface electronic structure, oxidation state dynamics, defect chemistry, and the adsorption and lifetime of key reaction intermediates. Strategies such as electronic structure modulation through doping, regulation of oxygen vacancy populations, and spatial control of active sites may enable preferential stabilization or rapid desorption of C_2 intermediates while suppressing deep oxidation toward C_1 products.

6.2 Decoding catalyst phase transitions during the reaction

The mechanisms behind these transformations, including when the reconstruction begins, how fast it proceeds, which bonds break or reform, whether lattice oxygen participates, and how electron-transfer pathways evolve, are still poorly understood. These unanswered questions limit our ability to rationally design catalysts with predictable performance. To address this gap, future research must leverage advanced *operando* tools such as XAS, Raman, SEIRAS, and cryo-TEM to capture transient intermediates and visualize real-time structural evolution under working conditions. By directly observing how catalysts change during the reaction, the field can move beyond simple correlations between precursor materials and activity and instead focus on designing catalysts based on the actual active phases formed *in situ*.

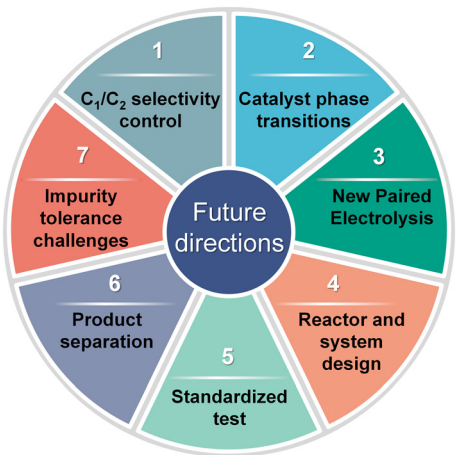

Fig. 15 Schematic illustration of future research directions for advancing electrochemical PET upcycling.

6.3 Emerging cathodic reactions for new paired electrolysis

While the EGOR has already been paired with several cathodic reactions, including the HER, $2e^-$ ORR, CO_2RR, and NO_3^-RR, the search for next-generation cathodic pathways remains a largely unexplored frontier. Among these, coupling the EGOR with CO reduction (CORR) represents a particularly promising but unrealized opportunity: the CORR bypasses the $*CO_2 \rightarrow *CO$ activation barrier, is expected to operate at lower overpotentials, and could enable highly selective C_1 chemicals. Besides the CORR, several emerging cathodic reactions, such as biomass-derived oxalate reduction, electro-organic nitrogen incorporation, and other hybrid organic redox systems, have been conceptually demonstrated but remain at the proof-of-concept stage.

6.4 Reactor and system-level engineering for enhanced PET upcycling efficiency

Besides catalyst innovation, the next stage of progress will rely heavily on advanced reactor architectures capable of maximizing mass transport, reaction selectivity, and energy utilization during PET electro-upcycling. Flow-by and flow-through electrochemical reactors with tailored hydrodynamics can significantly accelerate the EGOR, while also enabling precise synchronization with cathodic paired reactions. Meanwhile, ion-exchange membranes with optimized conductivity and crossover suppression are essential to maintain long-term operational stability.

6.5 Establishing standardized testing protocols for benchmarking and translation

The lack of standardized testing protocols has emerged as a critical barrier to meaningful performance comparison and technology translation. Future research should prioritize the development of community-accepted evaluation frameworks that define reference reaction conditions, standardized reporting parameters, and unified durability and stability testing protocols.

6.6 Product separation considerations in paired PET electro-upcycling

The practical viability of electrochemical PET upcycling critically depends on downstream product separation, an aspect that remains largely underexplored in current studies. In paired electrolysis systems that generate liquid products at both electrodes (*e.g.*, formate at the anode coupled with ammonia or other reduced nitrogen species at the cathode), separation processes can become a dominant contributor to overall energy consumption and operating cost. Future research should explicitly evaluate separation complexity when designing paired reaction schemes, prioritizing product combinations that enable spontaneous phase separation,

membrane-assisted compartmentalization, or low-energy purification pathways.

6.7 Impurity tolerance toward realistic PET waste electro-upcycling

PET waste contains a wide range of additives, including dyes, plasticizers, stabilizers, adhesives, and residual polymers, which may adsorb onto catalyst surfaces, modify interfacial reaction environments, or induce irreversible catalyst poisoning. Addressing impurity tolerance therefore constitutes a critical step toward practical deployment. Future research should systematically compare catalyst performance in clean model systems and impurity-rich realistic feeds, coupled with *operando* spectroscopic and electrochemical diagnostics to elucidate poisoning mechanisms. These insights will inform the rational design of impurity-resilient catalysts and pretreatment strategies, ultimately enabling robust electrochemical PET upcycling under real-world conditions.

7 Conclusion

In this work, the PET-derived EGOR proceeds through competitive C_1 and C_2 pathways, whose selectivity is governed not only by the applied potential but also by the catalyst electronic structure, surface reconstruction, mass transport, and intermediate lifetime. While most reported systems favor C_1 products due to the facile C–C cleavage on highly oxidizing oxyhydroxide surfaces, steering selectivity toward C_2 products remains a critical goal for improving carbon utilization and energy efficiency. Significant progress has been achieved in catalyst development, spanning noble metals, transition-metal compounds, MOFs, organic catalysts, and heterojunction interfaces. In parallel, coupling the EGOR with energy-saving cathodic reactions, such as the HER, $2e^-$ ORR, CO_2RR, and NO_3^-RR, has emerged as a powerful system-level strategy to replace the oxygen evolution reaction, significantly lowering cell voltage while enabling dual production of fuels and chemicals. Despite these advances, several challenges must be addressed to enable practical deployment. These include maintaining C_2 selectivity at industrially relevant current densities, improving tolerance toward impurities in real PET waste streams, addressing downstream product separation in paired electrolysis, and establishing standardized testing protocols for meaningful performance comparison. Addressing these challenges will require a shift from catalyst-centric optimization toward mechanism-guided control and system-level design. Overall, electrochemical PET upcycling stands at the intersection of plastic waste management, green chemistry, and energy conversion, and continued progress in this field could play a transformative role in enabling a circular carbon economy.

Conflicts of interest

The authors declare no conflicts of interest.

Data availability

No primary research results, software or code have been included and no new data were generated or analysed as part of this review.

Acknowledgements

This work was financially supported by the National Natural Science Foundation of China (No. 52200076), the Special Research Fellowship of the Chinese Academy of Sciences (No. E3296201), the Research Foundation of Chongqing University of Science and Technology (No. ckrc2022015), and the Natural Science Foundation of Chongqing (No. CSTB2025NSCQ-GPX0920).

References

1 M. Alreshidi, K. Yadav, A. Gacem, S. Padmanabhan, S. Ganesan, L. Guganathan, P. Saravanan, K. Thajudeen, A. Fallatah, M. Ahmed, F. Aldosari, G. Shoba, C. Kavitha, P. Tamizhdurai, A. Subramani and R. Kumaran, Nanocatalytic upcycling of plastic waste: Advances in selective conversion technologies for sustainable high-value products recovery, *Results Eng.*, 2025, **28**, 107042.
2 W. Li, Q. Li, L. Zhu and S. Chen, Generation of singlet oxygen by 2D Fe_3O_4-decorated black phosphorus nanosheets to boost photothermal catalytic upcycling of PET wastes, *Chem. Eng. J.*, 2025, **521**, 166866.
3 R. Xue, C. Qiu, X. Zhou, Y. Cheng, Z. Zhang, Y. Zhang, U. Schröder, U. Bornscheuer, W. Dong, R. Wei and M. Jiang, Enzymatic upcycling of PET waste to calcium terephthalate for battery anodes, *Angew. Chem., Int. Ed.*, 2024, **63**, e202313633.
4 Z. Chen, W. Wei, X. Chen, Y. Liu, Y. Shen and B.-J. Ni, Upcycling of plastic wastes for hydrogen production: Advances and perspectives, *Renewable Sustainable Energy Rev.*, 2024, **195**, 114333.
5 Z. Chen, W. Wei and B.-J. Ni, Prioritizing capture and utilization for microplastic management in water systems, *Nat. Rev. Clean Technol.*, 2025, **1**, 525–527.
6 Z. Guo, Y. Li, M. Wang and D. Ma, Catalytic upcycling of PET: From waste to chemicals and degradable polymers, *Acc. Chem. Res.*, 2025, **58**, 3184–3194.
7 Y. Ma, M. Han, Y. Qian, D. Xing, J. Ma, Y. Yu, B. Qiu and Y. Zhang, Tandem depolymerization-electrocatalysis for plastic waste upcycling, *Green Chem.*, 2026, **28**, 96–119.
8 N. Hamidi, M. Yazdani-Pedram and N. Abdussalam, Upcycling poly(ethylene terephthalate) wastes by solvent extraction: Thermal stability and kinetics studies of the recovered PET, *J. Appl. Polym. Sci.*, 2022, **139**, 51905.
9 J. Liu, X. Ouyang, Y. Zhang, G. Luo, Q. Mei and S. Zhang, Research progress on chemical depolymerization and upcycling of PET waste plastics, *Chin. Sci. Bull.*, 2025, **70**, 2878–2891.
10 S. Cai, Y. Wang, Z. Guo, X. Deng, D. Liu, J. Beiyuan, D. Lv, J. Peng, L. Huang, R. Cha and W. Yuan, Mechanochemically

catalytic upcycling of PET wastes toward aerogels for thermal insulation, *Chem. Eng. J.*, 2024, **497**, 154583.
11 E. Yalcinkaya, H. Baskan-Bayrak and B. Okan, Growing of 2D/3D graphene structures on natural substrates from aromatic plastic wastes by scalable thermal-based upcycling process with a comparative CO_2 footprint analysis, *Sustainable Mater. Technol.*, 2023, **37**, e00687.
12 M. Jung, I. Yang, D. Choi, J. Lee and J. Jung, Activated carbons derived from polyethylene terephthalate for coin-cell supercapacitor electrodes, *Korean J. Chem. Eng.*, 2023, **40**, 2442–2454.
13 C. Podara, S. Termine, M. Modestou, D. Semitekolos, C. Tsirogiannis, M. Karamitrou, A. Trompeta, T. Milickovic and C. Charitidis, Recent trends of recycling and upcycling of polymers and composites: A comprehensive review, *Recycling*, 2024, **9**, 37.
14 D. Ejeta, M. Li, Y. Hsu, M. Iqbal and C. Lin, Upcycling waste PET into benzoxazines with simultaneously low curing temperatures and high thermal stability, *Chem. Eng. J.*, 2025, **521**, 166130.
15 J. Lee, N. Hayat, X. Soo, S. Tan, Y. Hnin, S. Wang, F. Wei, D. Kai, F. Wang, P. Luo, J. Xu, X. Loh and Q. Zhu, Upcycling of PET plastics into diethyl terephthalate for applications as phase change materials in energy harvesting, *J. Energy Storage*, 2023, **73**, 109084.
16 H. Kang, D. He, C. Turchiano, X. Yan, J. Chai, M. Weed, G. Elliott, D. Onofrei, X. Pan, X. Xiao and J. Gu, Mining the carbon intermediates in plastic waste upcycling for constructing C-S bond, *J. Am. Chem. Soc.*, 2024, **146**, 18639–18649.
17 V. Küçük, T. Uygunoglu and B. Simsek, Investigation of the effect of high-purity terephthalic acid obtained by hydrolysis of PET bottle wastes on the cementitious composite properties, *J. Mater. Civ. Eng.*, 2025, **37**, 04025128.
18 N. Li, Z. Li, Y. Cui, L. Liang, W. Peng, Z. Cheng, B. Yan and G. Chen, Chemical upcycling of biodegradable plastic waste: A critical review, *Green Chem.*, 2025, **27**, 9000–9015.
19 H. Zhang, T. Fang, X. Yao, X. Li and W. Zhu, Catalytic amounts of an antibacterial monomer enable the upcycling of poly(ethylene terephthalate) waste, *Adv. Mater.*, 2023, **35**, 2210758.
20 M. Du, R. Xue, W. Yuan, Y. Cheng, Z. Cui, W. Dong and B. Qiu, Tandem integration of biological and electrochemical catalysis for efficient polyester upcycling under ambient conditions, *Nano Lett.*, 2024, **24**, 9768–9775.
21 J. Yang, Z. Li, Q. Xu, W. Liu, S. Gao, P. Qin, Z. Chen and A. Wang, Towards carbon neutrality: Sustainable recycling and upcycling strategies and mechanisms for polyethylene terephthalate via biotic/abiotic pathways, *Eco-Environ. & Health*, 2024, **3**, 117–130.
22 T. Zhang, X. Li, J. Wang, Y. Miao, T. Wang, X. Qian and Y. Zhao, Photovoltaic-driven electrocatalytic upcycling poly(ethylene terephthalate) plastic waste coupled with hydrogen generation, *J. Hazard. Mater.*, 2023, **450**, 131054.
23 J. Zhang, X. Zhang, C. Shi, X. Yu, Y. Zhou and L. Di, Plasma-constructed Co_2P-Ni_2P heterointerface for electro-upcycling of polyethylene terephthalate plastic to co-produce hydrogen and formate, *Small*, 2024, **20**, 2406767.
24 G. Wang, Z. Chen, W. Wei and B. Ni, Electrocatalysis-driven sustainable plastic waste upcycling, *Electron*, 2024, **2**, e34.
25 Y. X. Leiu, K. M. Lim, Z. J. Chiah, E. S. Z. Mah and W. J. Ong, Plastic-to-treasure: Innovative advances in photo/electro-catalytic upcycling technologies for commodity chemicals and fuels, *EcoEnergy*, 2024, **3**, 217–253.
26 J. Li, J. Chen, L. Zhang, J. Matos, L. Wang and J. Yang, Electrocatalytic upcycling of plastic waste: Progress, challenges, and future, *Electron*, 2024, **2**, e63.
27 T. Ren, Z. Duan, H. Wang, H. Yu, K. Deng, Z. Wang, H. Wang, L. Wang and Y. Xu, Electrochemical co-production of ammonia and biodegradable polymer monomer glycolic acid via the co-electrolysis of nitrate wastewater and waste plastic, *ACS Catal.*, 2023, **13**, 10394–10404.
28 Y. Ma, X. Guo, W. Yuan, P. Yang, Y. Zhang, W. Chen, L. Cai, V. Nicolosi, W. Wang, Y. Chai and B. Qiu, Paired electrochemical synthesis of glycolic acid and ammonia from polyester and nitrate sewage, *Chem. Catal.*, 2025, **5**, 101336.
29 K. Liu, X. Gao, C. X. Liu, R. Shi, E. C. M. Tse, F. Liu and Y. Chen, Energy-saving hydrogen production by seawater splitting coupled with PET plastic upcycling, *Adv. Energy Mater.*, 2024, **14**, 2304065.
30 C. O. Ehi-Eromosele, C. N. Onwucha, S. O. Ajayi, G. Melinte, A. L. Hansen, S. Indris and H. Ehrenberg, Ionothermal synthesis of activated carbon from waste PET bottles as anode materials for lithium-ion batteries, *RSC Adv.*, 2022, **12**, 34670–34684.
31 S. Ren and A. Kamali, Upcycling waste polyethylene terephthalate for enhanced Na-ion storage, *J. Energy Storage*, 2025, **118**, 116127.
32 L. Wang, R. Fu, M. Ouyang, C. Li, Z. Cui, H. Wu, C. Zhang and K. Wang, Turning plastic trash into energy: Converted MOFs and carbon for energy storage, *J. Power Sources*, 2025, **645**, 237156.
33 M. Tan, L. Goh, D. Safanama, W. Loh, N. Ding, S. Chien, S. Goh, W. Thitsartarn, J. Lim and D. Fam, Upcycling waste poly(ethylene terephthalate) into polymer electrolytes, *J. Mater. Chem. A*, 2022, **10**, 24468–24474.
34 N. Alhokbany, J. Ahmed, M. Ubaidullah, S. Mutehri, M. Khan, T. Ahamad and S. Alshehri, Cost-effective synthesis of $NiCo_2O_4$@nitrogen-doped carbon nanocomposite using waste PET plastics for high-performance supercapacitor, *J. Mater. Sci.: Mater. Electron.*, 2020, **31**, 16701–16707.
35 M. Kigozi, G. Kasozi, S. Mohite, S. Zamisa, R. Karpoormath, J. Kirabira and E. Tebandeke, Non-emission hydrothermal low-temperature synthesis of carbon nanomaterials from poly (ethylene terephthalate) plastic waste for excellent supercapacitor applications, *Green Chem. Lett. Rev.*, 2023, **16**, 2173025.
36 S. Chen and Y. Hu, All-plastic supercapacitors from poly(ethylene terephthalate) waste, *Energy Fuels*, 2025, **39**, 18128–18137.

37 R. Cherian, C. J. Binish and A. V. Vijayasankar, Eco-frameworks for a cleaner planet: Harnessing next-gen MOFs for pollution and plastic waste remediation, *Polym. Degrad. Stab.*, 2025, **238**, 111349.
38 Z. Xu, Z. Zhou, Q. Chen, X. Zeng, J. Sun, Z. Sun, P. Song and R. Song, Upcycling waste PET to oxygen-rich carbon nanotubes for high-performance supercapacitor with ultra-high cycling stability, *J. Mater. Chem. A*, 2025, **13**, 28090–28099.
39 X. Wei, Z. Shen, R. Wei, X. Zhang, Z. Zhu, Y. Wang, L. Wang, S. Wang and S. Yin, Engineering p-d orbital hybridization in PdSb bimetallene for energy-saving H_2 production parallel upgrade plastic waste, *Chem. Eng. J.*, 2024, **498**, 155104.
40 S. Han, L. Sun, D. Fan and B. Liu, Pulsed electrosynthesis of glycolic acid through polyethylene terephthalate upcycling over a mesoporous PdCu catalyst, *Nat. Commun.*, 2025, **16**, 3426.
41 L. Jiao, W. Wei, X. Li, C. B. Hong, S. G. Han, M. I. Khan and Q. L. Zhu, Value-added formate production from selective ethylene glycol oxidation based on cost-effective self-supported MOF nanosheet arrays, *Rare Met.*, 2022, **41**, 3654–3661.
42 Z. Wang, Q. Zhang, J. Gao, J. Wang, H. He, S. Pan, Y. Zhao and X. Zhang, Solar-driven plastic reforming with CO_2 conversion to value-added chemicals using bifunctional copper hydroxide catalyst, *Small*, 2025, **21**, 2502144.
43 H. Zhang, Y. Wang, X. Li, K. Deng, H. Yu, Y. Xu, H. Wang, Z. Wang and L. Wang, Electrocatalytic upcycling of polyethylene terephthalate plastic to formic acid coupled with energy-saving hydrogen production over hierarchical Pd-doped NiTe nanoarrays, *Appl. Catal., B*, 2024, **340**, 123236.
44 F. Liu, J. Zhou, X. Gao, R. Shi, Z. Guo, E. Tse and Y. Chen, Modulating adsorption behavior by single-site Pt on RuO_2 for efficient electrosynthesis of glycolic acid from plastic wastes, *Angew. Chem., Int. Ed.*, 2025, **64**, e202422183.
45 S. Kang, W. Yuan, X. Guo, Y. Zhang, J. Shang, P. Yang, Y. Ma, V. Nicolosi, L. Cai and B. Qiu, Concurrent production of glycolic acid via anode valorization of plastic paired with cathode upcycling of biomass derivative, *Angew. Chem., Int. Ed.*, 2025, **64**, e202504993.
46 W. Li, D. Xiao, X. Gong, X. Xu, F. Ma, Z. Wang, P. Wang, Y. Liu, Y. Dai, Z. Zheng, Y. Fan and B. Huang, Electrocatalytic upgrading of polyethylene terephthalate plastic to formic acid at an industrial-scale current density via Ni-MOF@MnCo-OH catalyst, *Chem. Eng. J.*, 2024, **480**, 148087.
47 J. Qi, J. Li, X. Meng, Z. Jiang, Z. Wang, Y. Ma, H. Zou, Y. Du, Z. Lin and J. Qiu, Chromium-modified nickel sulfide catalysts enable energy-efficient electrochemical polyethylene terephthalate upcycling, *Adv. Energy Mater.*, 2025, **15**, e04208.
48 J.-J. Zhao, H.-R. Zhu, C.-J. Huang, M.-H. Yin and G.-R. Li, Recent advances of ethylene glycol oxidation reaction: Catalytic mechanism, catalyst design and applications, *J. Mater. Chem. A*, 2025, **13**, 3236–3272.
49 D. Jang, M. Park, J. Maeng, J. Ha, S. Choi, N. Kim, M. H. Seo and W. B. Kim, Structural modification effect of Se-doped porous carbon for hydrogen evolution coupled selective electrooxidation of ethylene glycol to value-added glycolic acid, *Small*, 2024, **20**, e2404540.
50 Z. Yu, M. Ji, Z. Zhang, Y. Zhang, A. Barras, A. Addad, L. Tang, Y. Chi, P. Roussel, S. Szunerits and R. Boukherroub, Electrocatalytic upcycling of polyethylene terephthalate to formic acid and hydrogen fuels using $CoCuO_x$/MXene catalyst, *J. Energy Chem.*, 2025, **104**, 91–100.
51 M. Jiang, Y. Yang, Y. Wang, Y. Wang, M. Ratova and D. Wu, Closed-loop electro-upcycling of PET waste into formate and hydrogen via self-supported $NiCo_2O_4$ spinel arrays, *Green Chem.*, 2025, **27**, 9978–9991.
52 Y. Zhou, T. Tian, S. Jiang, R. Shen, H. Yu, Z. Wang, H. Wang, L. Wang and K. Deng, Alternating pulse driven periodic reactivation of high-entropy mesoporous film boosts continuous membrane-free PET waste upcycling coupled with H_2 production, *Adv. Funct. Mater.*, 2025, **36**, e11835.
53 A. Serov, T. Asset, M. Padilla, I. Matanovic, U. Martinez, A. Roy, K. Artyushkova, M. Chatenet, F. Maillard, D. Bayer, C. Cremers and P. Atanassov, Highly-active Pd–Cu electrocatalysts for oxidation of ubiquitous oxygenated fuels, *Appl. Catal., B*, 2016, **191**, 76–85.
54 Y. Wang, M. Zheng, H. Sun, X. Zhang, C. Luan, Y. Li, L. Zhao, H. Zhao, X. Dai, J.-Y. Ye, H. Wang and S.-G. Sun, Catalytic Ru containing Pt_3Mn nanocrystals enclosed with high-indexed facets: Surface alloyed Ru makes Pt more active than Ru particles for ethylene glycol oxidation, *Appl. Catal., B*, 2019, **253**, 11–20.
55 Z. Tu, X. He, X. Liu, D. Xiong, S. Xue, D. Wu, J. Wang and Z. Chen, Upcycling polyethylene terephthalate plastic to C2 chemicals in parallel with nitrate reduction to ammonia or electric energy generation, *Chem. Mater.*, 2025, **37**, 1195–1204.
56 Y. Yang, X. Cao, L. Huang, Q. Li, L. Gu, Z. Yan, M. Li, R. Cheng, Z. Lu, A. Wang and W. Yang, Hybrid oxidization of ethylene glycol on defective Ag-PtPd electrocatalyst beyond 3000 h stability at an industrial-scale current density, *Adv. Funct. Mater.*, 2025, **35**, 2418588.
57 Z. Shen, Z. Niu, L. Zhang, X. Wei, Z. Zhu, F. Zheng, S. Yin and S. Wang, Ligand-modified PdPb bimetallenes electrocatalysts for efficient PET upcycling, *AIChE J.*, 2025, **71**, e70006.
58 Z. Wang, J. Song, H. Zhang, K. Deng, H. Yu, Y. Xu, H. Wang and L. Wang, Electrocatalytic valorization of nitrate and polyester plastic for simultaneous production of ammonia and glycolic acid, *Small*, 2024, **20**, e2404124.
59 Z. Li, S. Wang, Y. Yin, R. Qin, C. Wei, H. Luo and T. Mu, Electrooxidation of ethylene glycol to glycolic acid with Pt-$Ni(OH)_2$ catalysts: High efficiency and selectivity for PET plastics upgrading, *Chem. – Asian J.*, 2025, **20**, e202401843.
60 J. Li, L. Li, X. Ma, X. Han, C. Xing, X. Qi, R. He, J. Arbiol, H. Pan, J. Zhao, J. Deng, Y. Zhang, Y. Yang and A. Cabot, Selective ethylene glycol oxidation to formate on nickel

selenide with simultaneous evolution of hydrogen, *Adv. Sci.*, 2023, **10**, e2300841.
61 H. Lv, Y. Mao, H. Yao, H. Ma, C. Han, Y. Y. Yang, Z. A. Qiao and B. Liu, Ir-doped CuPd single-crystalline mesoporous nanotetrahedrons for ethylene glycol oxidation electrocatalysis: Enhanced selective cleavage of C–C bond, *Angew. Chem., Int. Ed.*, 2024, **63**, e202400281.
62 R. B. de Lima, V. Paganin, T. Iwasita and W. Vielstich, On the electrocatalysis of ethylene glycol oxidation, *Electrochim. Acta*, 2003, **49**, 85–91.
63 R. G. Freitas, E. P. Antunes, P. A. Christensen and E. C. Pereira, The influence of Ir and Pt_1Ir_1 structure in metallic multilayers nanoarchitectured electrodes towards ethylene glycol electro-oxidation, *J. Power Sources*, 2012, **214**, 351–357.
64 J.-X. Tang, Q.-S. Chen, L.-X. You, H.-G. Liao, S.-G. Sun, S.-G. Zhou, Z.-N. Xu, Y.-M. Chen and G.-C. Guo, Screw-like PdPt nanowires as highly efficient electrocatalysts for methanol and ethylene glycol oxidation, *J. Mater. Chem. A*, 2018, **6**, 2327–2336.
65 J. Qi, N. Benipal, C. Liang and W. Li, PdAg/CNT catalyzed alcohol oxidation reaction for high-performance anion exchange membrane direct alcohol fuel cell (alcohol = methanol, ethanol, ethylene glycol and glycerol), *Appl. Catal., B*, 2016, **199**, 494–503.
66 J. Qi, Z. An, C. Li, X. Chen, W. Li and C. Liang, Electrocatalytic selective oxidation of ethylene glycol: A concise review of catalyst development and reaction mechanism with comparison to thermocatalytic oxidation process, *Curr. Opin. Electrochem.*, 2022, **32**, 100929.
67 B. Qiao, T. Yang, S. Shi, N. Jia, Y. Chen, X. Chen, Z. An and P. Chen, Highly active hollow RhCu nanoboxes toward ethylene glycol electrooxidation, *Small*, 2021, **17**, e2006534.
68 M. Park, J. Hwang, S. Jin, D. Jang, H. J. Kim, S. M. Choi, M. H. Seo and W. B. Kim, Unveiling the role of hydroxyl groups in glycerol as a critical descriptor for efficient electrocatalytic reforming of biomass molecules using PtCu alloy nanoparticle catalysts, *Chem. Eng. J.*, 2023, **466**, 143138.
69 A. Dailey, J. Shin and C. Korzeniewski, Ethylene glycol electrochemical oxidation at platinum probed by ion chromatography and infrared spectroscopy, *Electrochim. Acta*, 1998, **44**, 1147–1152.
70 E. G. Mahoney, W. Sheng, M. Cheng, K. X. Lee, Y. Yan and J. G. Chen, Analyzing the electrooxidation of ethylene glycol and glucose over platinum-modified gold electrocatalysts in alkaline electrolyte using in-situ infrared spectroscopy, *J. Power Sources*, 2016, **305**, 89–96.
71 H. Wang, B. Jiang, T.-T. Zhao, K. Jiang, Y.-Y. Yang, J. Zhang, Z. Xie and W.-B. Cai, Electrocatalysis of ethylene glycol oxidation on bare and Bi-modified Pd concave nanocubes in alkaline solution: An interfacial infrared spectroscopic investigation, *ACS Catal.*, 2017, **7**, 2033–2041.
72 A. Falase, K. Garcia, C. Lau and P. Atanassov, Electrochemical and in situ IR characterization of PtRu catalysts for complete oxidation of ethylene glycol and glycerol, *Electrochem. Commun.*, 2011, **13**, 1488–1491.
73 J. Schnaidt, M. Heinen, Z. Jusys and R. J. Behm, Electrooxidation of ethylene glycol on a Pt-film electrode studied by combined in situ infrared spectroscopy and online mass spectrometry, *J. Phys. Chem. C*, 2012, **116**, 2872–2883.
74 L. Xin, Z. Zhang, J. Qi, D. Chadderdon and W. Li, Electrocatalytic oxidation of ethylene glycol (EG) on supported Pt and Au catalysts in alkaline media: Reaction pathway investigation in three-electrode cell and fuel cell reactors, *Appl. Catal., B*, 2012, **125**, 85–94.
75 W. J. Pech-Rodríguez, C. Calles-Arriaga, D. González-Quijano, G. Vargas-Gutiérrez, C. Morais, T. W. Napporn and F. J. Rodríguez-Varela, Electrocatalysis of the ethylene glycol oxidation reaction and in situ Fourier-transform infrared study on PtMo/C electrocatalysts in alkaline and acid media, *J. Power Sources*, 2018, **375**, 335–344.
76 I. Kohlhaas and R. Palkovits, Elucidating the influence of catalyst cycling and activation on the activity of Ni-based layered double hydroxides for electrochemical oxidation of ethylene glycol to formate, *ChemElectroChem*, 2025, **12**, e202500190.
77 E. Sitta, R. Nagao and H. Varela, The electro-oxidation of ethylene glycol on platinum over a wide pH range: Oscillations and temperature effects, *PLoS One*, 2013, **8**, e75086.
78 I. Danaee, M. Jafarian, A. Sangachin and F. Gobal, A comparative study of the electrooxidation of ethylene glycol on transition metal electrodes in alkaline solution, *J. New Mater. Electrochem. Syst.*, 2012, **15**, 255–263.
79 E. Sitta, R. Nagao, I. Z. Kiss and H. Varela, Impact of the alkali cation on the oscillatory electro-oxidation of ethylene glycol on platinum, *J. Phys. Chem. C*, 2015, **119**, 1464–1472.
80 X. Wang, Y. Su, J. Chen, E. Yan, Q. Xia, J. Wu, S. Gong, M. Tang, W. Yip, Y. Mu, Y. Yi, J. Wu, F. Xu, X. Yang, X. Zhang, S. Dou, J. Sun and G. Zheng, Revisiting Pt foil catalysts for formamide electrosynthesis achieved at industrial-level current densities, *Nat. Commun.*, 2025, **16**, 8040.
81 X. Li, J. Sun, H. Ma, X. Long, T. Li, Y. Shimoyama, T. Naito, K. Sato, H. Yamada, K. Nagaoka, Y. Zhao and X. Qian, Efficient metallic Ni as a bifunctional electrocatalyst for integrating continuous PET plastic upcycling with hydrogen production, *Appl. Catal., B*, 2025, **371**, 125211.
82 J. Jiang, L. Zhang, G. Wu, J. Zhang, Y. Yang, W. He, J. Zhu, J. Zhang and Q. Qin, Efficient electrochemical-enzymatic conversion of PET to formate coupled with nitrate reduction over Ru-doped Co_3O_4 catalysts, *Angew. Chem., Int. Ed.*, 2025, **64**, e202421240.
83 Y. Ma, H. Ge, Y. Zhang, N. Jian, J. Yu, J. Arbiol, C. Li, Y. Zhong, L. Li, H. Kang, J. Wang, A. Cabot and J. Li, Selective electrooxidation of ethylene glycol to formate with hydrogen cogeneration in Ni_3S_2 nanodomains on NiFeMn-LDH nanosheet arrays, *ACS Sustainable Chem. Eng.*, 2025, **13**, 5601–5612.
84 L. Yun, X. Shi, T. Chen, Y. Gu, M. Qiao, H. Zhang and J. Wang, High-gravity-assisted synthesis of $NiCo_2O_4$/C for electro-upcycling polyethylene terephthalate to commodity chemicals, *Chem. Eng. Sci.*, 2025, **304**, 121084.

85 Y. Ma, L. Li, J. Tang, Z. Hu, Y. Zhang, H. Ge, N. Jian, J. Zhao, A. Cabot and J. Li, Electrochemical PET recycling to formate through ethylene glycol oxidation on Ni–Co–S nanosheet arrays, *J. Mater. Chem. A*, 2024, **12**, 33917–33925.

86 R. Rojas-Luna, L. Cousins, R. Germaney, D. Gil-Gavilan, M. Castillo-Rodriguez, D. Osorio, T. Doughty, D. Esquivel, C. Creissen and S. Roy, Coelectrolysis of PET and CO_2 using an electrochemically restructured Co-MOF-74 anode and a polymeric Co-phthalocyanine cathode, *ACS Appl. Mater. Interfaces*, 2026, **18**, 6937–6951.

87 S. Dinda, R. Bhavana, S. Behera and B. Mondal, Metal-free electrocatalytic upcycling of polyethylene terephthalate plastic to C_2 products, *Chem. Commun.*, 2024, **60**, 7777–7780.

88 Z. Ying, F. Sultana, R. Li, X. Zhang, R. Li, T. Li and X. Yan, Efficient electrooxidation of PET-derived ethylene glycol using a Fe_3O_4-$NiCo_2O_4$ heterostructure: Toward sustainable plastic upcycling, *Int. J. Hydrogen Energy*, 2025, **190**, 152218.

89 M. Song, Y. Wu, Z. Zhao, M. Zheng, C. Wang and J. Lu, Corrosion engineering of part-per-million single atom Pt1/$Ni(OH)_2$ electrocatalyst for PET upcycling at ampere-level current density, *Adv. Mater.*, 2024, **36**, e2403234.

90 Y. Li, L. Liu, X.-H. Wang, C. Chen, M. Li, J.-Y. Wang and S.-N. Li, Electrochemical upgrading of PET plastic wastes for hydrogen production using porous Fe–Ni_2P nanosheets, *Int. J. Hydrogen Energy*, 2024, **96**, 794–802.

91 G. Zhao, J. Lin, M. Lu, L. Li, P. Xu, X. Liu and L. Chen, Potential cycling boosts the electrochemical conversion of polyethylene terephthalate-derived alcohol into valuable chemicals, *Nat. Commun.*, 2024, **15**, 8463.

92 M. Etesami and N. Mohamed, Electrooxidation of ethylene glycol using gold nanoparticles electrodeposited on pencil graphite in alkaline medium, *Sci. China: Chem.*, 2011, **55**, 247–255.

93 L. Sun, H. Lv, J. Xiao and B. Liu, Enzymatic mesoporous metal nanocavities for concurrent electrocatalysis of nitrate to ammonia coupled with polyethylene terephthalate upcycling, *Adv. Mater.*, 2024, **36**, 2402767.

94 X.-Y. Wang, Z. Han, J.-J. Duan, J.-J. Feng, H. Huang and A.-J. Wang, Facile construction of 3D hyperbranched PtRh nanoassemblies: A bifunctional electrocatalyst for hydrogen evolution and polyhydric alcohol oxidation reactions, *Int. J. Hydrogen Energy*, 2020, **45**, 8433–8443.

95 C. Hu, Y. Zhou, M. Xiao and G. Yu, Precise size and dominant-facet control of ultra-small Pt nanoparticles for efficient ethylene glycol, methanol and ethanol oxidation electrocatalysts, *Int. J. Hydrogen Energy*, 2020, **45**, 4341–4354.

96 S. Mondal, V. S. K. Choutipalli, B. K. Jena, V. Subramanian and C. R. Raj, Bifunctional electrocatalytic activity of ordered intermetallics based on Pd and Sn, *J. Phys. Chem. C*, 2020, **124**, 9631–9643.

97 H. Zhang, Z. Liu, H. Li, Z. Fu, G. Zhang, H. Zhang, G. Wang and Y. Zhang, PdFe alloy nanoparticles supported on nitrogen-doped carbon nanotubes for electrocatalytic upcycling of poly(ethylene terephthalate) plastics into formate coupled with hydrogen evolution, *J. Mater. Chem. A*, 2024, **12**, 15984–15995.

98 M. Zhan, L. Guo, X. Liang, Z. Zhao, X. Luo, R. Yu, Q. Wu, L. Zhang, R. Jin, Y. Zhu, Y. Jia and H. Zheng, Anchoring Pd single atoms through S vacancies of defective nickel-sulfur for efficient electrocatalytic polyethylene terephthalate oxidation coupled with hydrogen evolution, *J. Mater. Chem. A*, 2025, **13**, 26669–26680.

99 B. Zou, Y. Zhang, F. Gao, Z. Li, C. Wang, Z. Wu, D. Wang and Y. Du, 3D PdPb nanochain networks with efficient catalytic performance for ethylene glycol electrooxidation, *Int. J. Hydrogen Energy*, 2022, **47**, 33329–33337.

100 F. Varela, S. Luna and O. Savadogo, Synthesis and evaluation of highly tolerant Pd electrocatalysts as cathodes in direct ethylene glycol fuel cells (DEGFC), *Energies*, 2009, **2**, 944–956.

101 S. Xie, H. Huang, L. Deng, J. Li, R. Yue and J. Xu, Crinkly polypyrrole-modified reduced graphene oxide loaded Pd nanoparticles as highly efficient electrocatalyst for ethylene glycol oxidation, *Appl. Surf. Sci.*, 2022, **598**, 153879.

102 M. Hao, J. Bi, J. Hou, H. Ding and H. Xia, Plasmon-induced highly efficient cleavage of C–C bonds in electrocatalytic oxidation of ethylene glycol, *Chem. Eng. J.*, 2025, **524**, 168967.

103 W. Jiang, C. Zhu, H. Xu, J. Liu, Y. Wu, S. Cao, H. Yuan, P. Liu and Y. Zhou, In situ reconstruction of Au promoted CuOOH/NiOOH for efficient and selective ethylene glycol electrooxidation, *Chem. Eng. J.*, 2025, **515**, 163804.

104 H. Ma, S. He, Y. Zhang, L. Wang, Y. Yi and Y. Yang, Selective electrocatalytic oxidation of ethylene glycol into glycolic acid at coin-group electrodes: An investigation on catalytic activity and selectivity, *ACS Sustainable Chem. Eng.*, 2024, **12**, 12249–12259.

105 Q. Wu, H. Sun, Y. Min, L. Wang, Z. Wang, Y. Wang, Y. Zhao and Y. Zheng, Amine oxide surfactant-mediated synthesis of plate-based gold nanocrystals with tunable surface wrinkles and their applications in the ethylene glycol oxidation reaction, *CrystEngComm*, 2024, **26**, 5030–5038.

106 C. Wang, C. Wu, L. Xing, W. Duan, X. Zhang, Y. Cao and H. Xia, Facet-dependent long-term stability of gold aerogels toward ethylene glycol oxidation reaction, *ACS Appl. Mater. Interfaces*, 2020, **12**, 39033–39042.

107 A. S. Douk, H. Saravani, M. Farsadrooh and M. Noroozifar, An environmentally friendly one-pot synthesis method by the ultrasound assistance for the decoration of ultrasmall Pd-Ag NPs on graphene as high active anode catalyst towards ethanol oxidation, *Ultrason. Sonochem.*, 2019, **58**, 104616.

108 X. Guo, H. Shang, J. Guo, H. Xu and Y. Du, Ultrafine two-dimensional alloyed PdCu nanosheets-constructed three-dimensional nanoflowers enable efficient ethylene glycol electrooxidation, *Appl. Surf. Sci.*, 2019, **481**, 1532–1537.

109 Q. Zheng, L. Huang, S. Yang, Q. Liang, Y. Yang, L. Gu, R. Cheng, Y. Shen, Z. Yan and X. Cao, Synergy between multi-components and Ir dopant in Ir-doped high-entropy alloy

nanoparticles for efficient and robust ethylene glycol electro-oxidation at an industrial-level current, *Nanoscale*, 2025, **17**, 12989–12999.

110 Z. Zhang, Z. Yu, Y. Zhang, A. Barras, A. Addad, P. Roussel, L. Tang, S. Szunerits and R. Boukherroub, Seawater corrosive engineering assisted in-situ room temperature synthesis of Ni/Co/Fe trimetallic composition to achieve polyester plastics upgrading and green hydrogen production, *Chem. Eng. J.*, 2024, **498**, 155472.

111 H. Li, L. Li, W. Yang, J. Yang, S. Wang, H. Zhang, P. Cui, S. Yin, Y. Wang and J. Qi, Binary nonmetal boron and phosphorus co-doping into PdRh nanosheets boosts electro-upgrading polyethylene terephthalate, *Chem. Eng. J.*, 2024, **490**, 151696.

112 Z. Wang, J. Chen, Y. Wang, H. Yu, Y. Xu, K. Deng, H. Wang and L. Wang, Synergistic electronic effect in high-entropy PdPtSnBiAg metallene for electrochemical reforming of PET plastic into glycolic acid, *J. Mater. Chem. A*, 2025, **13**, 37178–37184.

113 H. Dai, K. Dong, T. Zhang, H. Pu, Y. Wang and Y. Deng, Electrodeposition of shaped PtIr alloy nanocrystals with high–index facets for the electro–catalytic oxidation of alcohols, *Appl. Surf. Sci.*, 2023, **609**, 155225.

114 V. Mudzunga, T. Matthews, S. Mbokazi, N. Maxakato, O. Fakayode, T. Mokrani and R. Sigwadi, Electrooxidation of ethylene glycol on carbon black-supported palladium-ruthenium nanoparticle's surface, *Fuel*, 2025, **381**, 133396.

115 X. Gu, H. Sun, N. Zhang, J. Yu, J. Li, C. Ye and Y. Du, Universal synthesis of highly active PdM (Sb, Ir, and Bi) nanowire networks for ethylene glycol and glycerol electrooxidation, *J. Colloid Interface Sci.*, 2025, **688**, 775–783.

116 H. Zhang, Z. Bian, S. Zhang, Z. Mao, H. Yin, G. Wang, H. Zhang, Y. Zhang and H. Zhao, Promoted hydroxylation on synergistic Ru single atom/cluster enables PET upcycling at industrial-level current densities, *Appl. Catal., B*, 2026, **383**, 126067.

117 N. Maxakato, C. Arendse and K. Ozoemena, Insights into the electro-oxidation of ethylene glycol at Pt/Ru nanocatalysts supported on MWCNTs: Adsorption-controlled electrode kinetics, *Electrochem. Commun.*, 2009, **11**, 534–537.

118 L. Fu, M. Wang, L. Hao, J. Lei, T. Liu, Z. Chen and C. Li, Ternary PdIrNi telluride amorphous mesoporous nanocatalyst for efficient electro-oxidation of ethylene glycol, *Catalysts*, 2025, **15**, 143.

119 J. J. Duan, X. X. Zheng, H. J. Niu, J. J. Feng, Q. L. Zhang, H. Huang and A. J. Wang, Porous dendritic PtRuPd nanospheres with enhanced catalytic activity and durability for ethylene glycol oxidation and oxygen reduction reactions, *J. Colloid Interface Sci.*, 2020, **560**, 467–474.

120 X. Liu, Z. Fang, D. Xiong, S. Gong, Y. Niu, W. Chen and Z. Chen, Upcycling PET in parallel with energy-saving H_2 production via bifunctional nickel-cobalt nitride nanosheets, *Nano Res.*, 2022, **16**, 4625–4633.

121 X. Zhang, X. Li, X. Zhang, H. Lu, Y. Sun, X. Duan and Y. Ren, Hierarchical CoFe-LDH with nanoneedle-assembled architecture for selective and efficient electrocatalytic oxidation of ethylene glycol to formate, *J. Electroanal. Chem.*, 2025, **998**, 119532.

122 X. Lu, Y. Guo, H. Fu, J. Song, C. Liang, H. Jiang, Z. Wang, Y. Liu, H. Cheng, Z. Zheng, Y. Wu, P. Wang and B. Huang, Electrochemical upcycling strategy for polyethylene terephthalate plastic coupled with efficient hydrogen production, *Chem. Eng. J.*, 2025, **506**, 159810.

123 J. Wu, J. Zheng, Z. Yu, C. Lin, K. Chen, N. Zhang and P. Chen, Industrial-grade electrocatalytic valorization of waste plastics via reconstructed Ni^{2+}-CoOOH nanosheet arrays, *Nano Res.*, 2025, **18**, 94907806.

124 Y. Sun, K. Fan, J. Li, L. Wang, Y. Yang, Z. Li, M. Shao and X. Duan, Boosting electrochemical oxygen reduction to hydrogen peroxide coupled with organic oxidation, *Nat. Commun.*, 2024, **15**, 6098.

125 Y. Yan, H. Zhou, S. Xu, J. Yang, P. Hao, X. Cai, Y. Ren, M. Xu, X. Kong, M. Shao, Z. Li and H. Duan, Electrocatalytic upcycling of biomass and plastic wastes to biodegradable polymer monomers and hydrogen fuel at high current densities, *J. Am. Chem. Soc.*, 2023, **145**, 6144–6155.

126 J. Liu, Y. Yang, E. Petit, V. Bonniol, Z. Anfar, B. Rebiere, B. A. Karamoko, W. Wang, H. Wu, M. Moderne, R. Guéret, P. Miele, N. M. Bedford, C. Salameh and D. Voiry, Structural insights into Ni-Fe layered double hydroxides as anode catalysts for pairing CO_2 reduction and ethylene glycol oxidation, *ACS Catal.*, 2025, **15**, 11861–11874.

127 X. Zhao, C. Kuang, C. An and M. Wang, Preparation of NiCo hydroxide by chloride corrosion for electrocatalytic upcycling of polyethylene terephthalate plastic waste, *Chem. Eng. J.*, 2024, **500**, 157275.

128 M. Jiang, Y. Yang, Y. Wang, Y. Wang, M. Ratova, W. Dai and D. Wu, Energy-efficient electrocatalytic upcycling of post-consumer PET plastics into valuable chemicals and hydrogen over MOF-derived NiCo hydroxide nanosheets, *Chem. Eng. Sci.*, 2025, **317**, 122101.

129 S. Yang, J. Han, W. Bao, T. Ai, X. Wei, P. Jiang, Z. Deng and J. Zhang, NiVFe-LDH nanosheets reinforced MoS_2 heterogeneous interface design for glycol-assisted water electrolysis, *Fuel*, 2025, **388**, 134482.

130 X. Xie, S. Zhou, C. Zhang, S. Dong and Z. Yang, Comparing copper and tin-based medium-entropy alloy oxide for producing hydrogen linking to waste polyethylene terephthalate (PET) upcycling, *J. Colloid Interface Sci.*, 2025, **698**, 138018.

131 P. Liu, G. Liu, J. Yang, S. Dong, Z. Zhang and Z. Yang, Rhenate-based low-entropy alloy oxide for polyethylene terephthalate upcycling coupling producing hydrogen, *Int. J. Hydrogen Energy*, 2025, **139**, 80–85.

132 S. A. Aladeemy, T. R. AlRijraji, M. S. Amer, P. Arunachalam and A. M. Al-Mayouf, Electrooxidation of ethylene glycol coupled with hydrogen production on porous NiO/Ni@ NF nanosheet electrocatalysts, *Catal. Sci. Technol.*, 2025, **15**, 2571–2583.

133 X. Zhao, C. Kuang, H. Liu, C. An, M. Wang and T. Mu, Spent lithium-ion batteries derived Co_3O_4 for

electrocatalytic polyethylene terephthalate plastic recycling, *ChemSusChem*, 2024, **17**, e202400105.

134 Y. Wang, F. Liu, J. Chen, E. Tse, R. Shi and Y. Chen, Scale-up upcycling of waste polyethylene terephthalate plastics to biodegradable polyglycolic acid plastics, *Nat. Commun.*, 2025, **16**, 4440.

135 S. Yang, C. Cai, J. Sun, N. Normakhamatov, A. Sharipov, C. Lu, X. Zhuang, X. Qian, Y. Zhao and T. Wang, Photovoltaic-driven electro-reforming of poly (ethylene terephthalate) (PET) waste plastics and nitrate pollutants, *Chem. Eng. Sci.*, 2024, **295**, 120186.

136 H.-R. Zhu, X.-L. Wang, J.-J. Zhao, M.-H. Yin, H.-M. Xu and G.-R. Li, Efficient photoelectrochemical cell composed of Ni single atoms/P, N-doped amorphous $NiFe_2O_4$ as anode catalyst and Ag NPs@CuO/Cu_2O nanocubes as cathode catalyst for microplastic oxidation and CO_2 reduction, *Chin. J. Catal.*, 2025, **76**, 159–172.

137 J. Xu, Y. Shi, J. Cheng and X. Wang, Recent research of $NiCo_2O_4$/carbon composites for supercapacitors, *Surfaces*, 2022, **5**, 334–349.

138 Y. Chen, C. Jia, C. Zhou, S. Wu, X. Xiang, N. Zhang, S. Zhao and Z. Lin, Electrocatalytic polyester waste upcycling via lattice oxygen redox activation, *Angew. Chem., Int. Ed.*, 2025, **64**, e202513447.

139 Y. Mao, S. Fan, X. Li, J. Shi, M. Wang, Z. Niu and G. Chen, Trash to treasure: electrocatalytic upcycling of polyethylene terephthalate (PET) microplastic to value-added products by $Mn_{0.1}Ni_{0.9}Co_2O_{4-\delta}$ RSFs spinel, *J. Hazard. Mater.*, 2023, **457**, 131743.

140 P. M. Pataniya, P. J. Sharma, S. A. Bhakhar, N. Rajani, M. N. Nandpal, K. A. Bhakhar, S. G. Patel, C. Vijayakumar and S. Ck, Coupling polyethylene terephthalate plastic upcycling and hydrogen evolution using cerium-doped nickel cobalt sulfide electrocatalysts, *ACS Appl. Mater. Interfaces*, 2026, **18**, 1843–1853.

141 L. Trotochaud, S. L. Young, J. K. Ranney and S. W. Boettcher, Nickel-iron oxyhydroxide oxygen-evolution electrocatalysts: The role of intentional and incidental iron incorporation, *J. Am. Chem. Soc.*, 2014, **136**, 6744–6753.

142 X. Zhu, Recent advances of transition metal oxides and chalcogenides in pseudo-capacitors and hybrid capacitors: A review of structures, synthetic strategies, and mechanism studies, *J. Energy Storage*, 2022, **49**, 104148.

143 Z. Chen, W. Wei, Y. Shen and B.-J. Ni, Defective nickel sulfide hierarchical structures for efficient electrochemical conversion of plastic waste to value-added chemicals and hydrogen fuel, *Green Chem.*, 2023, **25**, 5979–5988.

144 X. Wang, Y. Tang, J.-M. Lee and G. Fu, Recent advances in rare-earth-based materials for electrocatalysis, *Chem. Catal.*, 2022, **2**, 967–1008.

145 Z. Chen, R. Zheng, T. Bao, T. Ma, W. Wei, Y. Shen and B. J. Ni, Dual-doped nickel sulfide for electro-upgrading polyethylene terephthalate into valuable chemicals and hydrogen fuel, *Nano-Micro Lett.*, 2023, **15**, 210.

146 T. Matthews, T. H. Dolla, R. Mohamed, T. L. Yusuf, P. Chabalala, E. C. Agwamba, B. P. Doyle, E. Carleschi, L. Malepe and N. W. Maxakato, A novel Co_3Se_4-CNFs hybrid system as a versatile enhancer for Pd NPs toward ethylene glycol electrooxidation, *Adv. Mater. Interfaces*, 2025, **12**, e00475.

147 P. M. Pataniya, P. J. Sharma, S. A. Bhakhar, M. Patel, M. Nandpal, K. A. Bhakhar, S. Patel, P. Sahatiya, G. Nagaraju and C. K. Sumesh, Binder-free nickel iron selenide catalyst arrays for coupling hydrogen production with polyethylene terephthalate plastic electro-upcycling, *J. Mater. Chem. A*, 2025, **14**, 1923–1935.

148 H. Tu, Y. Zhong, Z. Yang, C. Zhang, Y. Ma, Y. Zhang, N. Jian, H. Ge and J. Li, Nickel selenides in electrocatalysis: Coupled formate and hydrogen production through methanol oxidation reaction, *Catalysts*, 2025, **15**, 516.

149 C.-Y. Lin, S.-C. Huang, Y.-G. Lin, L.-C. Hsu and C.-T. Yi, Electrosynthesized Ni-P nanospheres with high activity and selectivity towards photoelectrochemical plastics reforming, *Appl. Catal., B*, 2021, **296**, 120351.

150 J. Chang, L. Wang, D. Wu, F. Xu, K. Jiang, Y. Guo and Z. Gao, Concurrent electrocatalytic hydrogen evolution and polyethylene terephthalate plastics reforming by self-supported amorphous cobalt iron phosphide electrode, *J. Colloid Interface Sci.*, 2024, **655**, 555–564.

151 T. Xia, Z. Chen, C. Dong, X. Hu, S. Zhang, C. Yang, J. Hu, Y. Zhang, X. Jiang, H. Yang and B. Xia, Yeast inherited phosphide/bio-carbon for controllable polyethylene terephthalate upcycling, *Adv. Funct. Mater.*, 2025, **35**, 2503193.

152 Z. Fang, X. Du, K. Qian, Z. Deng, A. Hong, T. Li, T. Wei and R. Li, Interfacial effects in $Ni(OH)_2$/MnO@Ni aerogel heterostructures promote highly efficient electrooxidation of ethylene glycol to formate and hydrogen, *Int. J. Hydrogen Energy*, 2024, **74**, 39–48.

153 H. Zhou, Y. Ren, Z. Li, M. Xu, Y. Wang, R. Ge, X. Kong, L. Zheng and H. Duan, Electrocatalytic upcycling of polyethylene terephthalate to commodity chemicals and H_2 fuel, *Nat. Commun.*, 2021, **12**, 4679.

154 S. K. Kilaparthi, P. Pareek, A. Addad, P. Roussel, S. Szunerits, S. Sampath and R. Boukherroub, Integrated electrochemical conversion of plastic waste and CO_2 to formate using non-noble-metal catalysts: In situ Raman study, *ACS Appl. Mater. Interfaces*, 2025, **17**, 50591–50602.

155 T. Yang, C. Zhang, Z. Wang, P. Bai, X. Wang and Z. Chai, Ternary interface of Pt|few-layered N-rGO|TiN for the boasting electrocatalytic activity in ethylene glycol oxidation, *Adv. Mater. Interfaces*, 2020, **7**, 2000808.

156 E. Mari, P.-C. Tsai, M. Eswaran and V. K. Ponnusamy, Efficient electro-catalytic oxidation of ethylene glycol using flower-like graphitic carbon nitride/iron oxide/palladium nanocomposite for fuel cell application, *Fuel*, 2020, **280**, 118646.

157 Q. Li, G. Qin, L. Wu, Y. Zhao and X. Wang, High catalytic performance of a Pd-loaded TaN-TaC electrocatalyst for ethylene glycol oxidation in an alkaline medium, *Appl. Surf. Sci.*, 2021, **537**, 147849.

158 K. Deng, X. Liu, P. Liu, X. Lv, W. Tian and J. Ji, Stable and highly selective Co-CeF_3@Ni_3N sheet-on-sheet

heterostructures for PET electro-upgrading and hydrogen production, *Chem. Sci.*, 2025, **16**, 13905–13915.

159 M. Hadi, M. Khonjouki, H. Mostaanzadeh and A. Ehsani, Electrocatalytic oxidation of ethylene glycol on metal-organic framework (Ni-BTC)/multi-walled carbon nanotubes composite electrode, *Anal. Bioanal. Electrochem.*, 2024, **16**, 671–682.

160 Y. Zhao, D. Li, P. Cai, X. Ni, G. Chen, D. Xia, Z. Sun and H. Yuan, Architectural modulation of binary metal-organic frameworks upcycled from waste polyethylene terephthalate for high-performance supercapacitors, *J. Colloid Interface Sci.*, 2025, **700**, 138666.

161 L. Yun, M. Qiao, B. Zhang, H. Zhang and J. Wang, Upcycling plastic wastes into high-performance nano-MOFs by efficient neutral hydrolysis for water adsorption and photocatalysis, *J. Mater. Chem. A*, 2024, **12**, 19452–19461.

162 S. Das, T. Zhang, G. J. Clarkson, M. Walker, X. Qian, X. Long, Y. Zhao and R. I. Walton, Selective electrocatalytic production of formic acid from plastic waste using a nickel metal-organic framework constructed from a biomass-derived ligand, *ChemSusChem*, 2025, **18**, e202402319.

163 Z. Guo, M. Liu, L. Ga and J. Ai, Terbium-doped cobalt-based metal–organic frameworks for electrocatalytic hydrogen production and polyethylene terephthalate plastic upcycling, *Chem. Eng. J.*, 2024, **496**, 154062.

164 Z. Guo, M. Liu, L. Ga, J. Ai and W. Hai, Upcycling plastic waste: Ce-doped Co-based metal-organic framework synthesis using discarded polyethylene terephthalate and electrooxidation of polyethylene terephthalate hydrolysate coupled with hydrogen production, *Energy Mater. Adv.*, 2026, **7**, 0264.

165 M. Li, T. Xia, M. Wang, Y. Peng, S. Zhang, X. Jiang and H. Yang, Biocarbon-confined bimetallic FeCo metal-organic framework orthogonal nanosheet arrays for industry-level ethylene glycol oxidation, *Chin. J. Struct. Chem.*, 2025, **44**, 100627.

166 Z. L. He, X. Huang, Q. Chen, C. Zhai, Y. Hu and M. Zhu, Pt nanoclusters embedded Fe-based metal-organic framework as a dual-functional electrocatalyst for hydrogen evolution and alcohols oxidation, *J. Colloid Interface Sci.*, 2022, **616**, 279–286.

167 Q. Yu, Q. Xiang, J. Xie, Y. Zhou, X. Pan and H. Zhu, Efficient and stable MoCo-Ni$(OH)_2$/NF electrocatalyst for the upcycling of waste PET via ethylene glycol oxidation, *J. Electroanal. Chem.*, 2025, **994**, 119262.

168 X. Jin, X. Chen, C. Chen, X. Xiao, L. Chen, Z. Wang, B. Sun and D. Sun, Shell-like Ni$(OH)_2$ loaded with Pd nanoparticle catalyst mediated efficient electrocatalytic upcycling of polyethylene terephthalate plastics to glycolic acid, *J. Colloid Interface Sci.*, 2025, **688**, 403–410.

169 J. Sun, B. Shi, P. Wu, Y. Wang, L. Chu, H. Wang, S. Dai and M. Huang, Advanced electrocatalytic reforming of PET-derived ethylene glycol via electric field-driven d-band center modulation, *Nano Res.*, 2025, **18**, 94907473.

170 R. Qin, C. Wei, Y. Yin, Z. Yang, S. Wang, Y. Tian, L. Chen, Z. Xue and T. Mu, Closed-loop upcycling of PET waste into defect-engineered Ni@C electrocatalysts for efficient formate production, *Green Chem.*, 2025, **27**, 14279–14289.

171 S. Prabu, M. Vinu and K. Chiang, Upcycling polyethylene terephthalate-derived CoNi-metal-organic framework $MoSe_2$ hybrids for high-performance aqueous supercapacitors, *ChemSusChem*, 2025, **18**, e202501003.

172 X. Zhang, R. Wei, M. Yan, X. Wang, X. Wei, Y. Wang, L. Wang, J. Zhang and S. Yin, One-pot synthesis inorganic-organic hybrid PdNi bimetallenes for PET electrocatalytic value-added transformation, *Adv. Funct. Mater.*, 2024, **34**, 2401796.

173 J. Sun, B. Shi, S. Dai, L. Chu, H. Wang and M. Huang, Promoted *OH adsorption facilitates C–C bond cleavage for efficient electrochemical upcycling of polyethylene terephthalate, *ACS Catal.*, 2024, **15**, 529–542.

174 F. Liu, X. Gao, R. Shi, Z. Guo, E. C. M. Tse and Y. Chen, Concerted and selective electrooxidation of polyethylene-terephthalate-derived alcohol to glycolic acid at an industry-level current density over a Pd-Ni$(OH)_2$ catalyst, *Angew. Chem., Int. Ed.*, 2023, **62**, e202300094.

175 S. G. Peera and S. W. Kim, Rare earth Ce/CeO_2 electrocatalysts: Role of high electronic spin state of Ce and Ce^{3+}/Ce^{4+} redox couple on oxygen reduction reaction, *Nanomaterials*, 2025, **15**, 600.

176 Y. Wu, Y. Chang, Y. Su and J. Jia, Spinel $NiCo_2O_4$@CeO_{2-x}/NF with abundant oxygen vacancies and heterogeneous interfaces for efficient polyethylene terephthalate electrocatalytic conversion, *Electrochim. Acta*, 2026, **550**, 148072.

177 Z. Lang, Z. Zhuang, S. Li, L. Xia, Y. Zhao, Y. Zhao, C. Han and L. Zhou, MXene surface terminations enable strong metal-support interactions for efficient methanol oxidation on palladium, *ACS Appl. Mater. Interfaces*, 2020, **12**, 2400–2406.

178 W. Lv, X. Kong, H. Shi, L. Pan, R. Liu, C. Wang, M. Wei, R. Zhang and W. Wang, D NiCo bimetallic oxide nanowires for ethylene glycol electrooxidation with formate reoxidation suppression via concentration gradient strategy, *Inorg. Chem. Commun.*, 2025, **182**, 115605.

179 S. Behera, S. Dinda, R. Saha and B. Mondal, Quantitative electrocatalytic upcycling of polyethylene terephthalate plastic and its oligomer with a cobalt-based one-dimensional coordination polymer having open metal sites along with coproduction of hydrogen, *ACS Catal.*, 2022, **13**, 469–474.

180 F. Meng, H. Yan, X. Zhou, J. Zeng, X. Zhou, Y. Liu, X. Feng, D. Chen and C. Yang, Carbon-based metal-free catalysts for selective oxidation of glycerol to glycolic acid, *Chem. Eng. Sci.*, 2023, **268**, 118394.

181 F. Ma, Z. Li, R. Hu, Z. Wang, J. Wang, J. Li, Y. Nie, Z. Zheng and X. Jiang, Electrocatalytic waste-treating-waste strategy for concurrently upgrading of polyethylene terephthalate plastic and CO_2 into value-added formic acid, *ACS Catal.*, 2023, **13**, 14163–14172.

182 M. Wang, Q. Zhang, K. Chen, C. Lin, H. Wang, Y. Zhao and P. Chen, Atomic vacancy engineering of Co(OH)F nanoarray

toward high-performance ammonia electrosynthesis with waste plastics upgrading, *J. Energy Chem.*, 2025, **109**, 558–565.

183 J. Chang, L. Wang, Z. Hu, S. Zhi, D. Wu, K. Jiang and Z. Gao, Concurrent production of glycolate and H_2 via paired electrolysis: Ethylene glycol oxidation and hydrogen evolution from polyethylene terephthalate hydrolysate, *Chem. Eng. J.*, 2025, **520**, 166475.

184 X. Feng, L. Yang and L. Zhang, Sustainable solar-and electro-driven production of high concentration H_2O_2 coupled to electrocatalytic upcycling of polyethylene terephthalate plastic waste, *Chem. Eng. J.*, 2024, **482**, 149191.

185 J. Qi, Y. Du, Q. Yang, N. Jiang, J. Li, Y. Ma, Y. Ma, X. Zhao and J. Qiu, Energy-saving and product-oriented hydrogen peroxide electrosynthesis enabled by electrochemistry pairing and product engineering, *Nat. Commun.*, 2023, **14**, 6263.

186 Y. Fang, C. Cai, H. Yamashita, X. Qian and Y. Zhao, Efficient and cost-effective electrocatalysts for coproduction of formate through electrocatalytic oxidation of PET-derived ethylene glycol coupled with CO reduction, *Catal. Today*, 2026, **462**, 115544.

187 X. Yu, H. Rabiee, A. Dutta, Y. Li, Z. Szakaly, S. Vesztergom, L. Warmuth, A. Rieder and P. Broekmann, Upcycling CO_2 and PET waste: Ampere-level formate electrosynthesis in an integrated electrolyzer, *J. Am. Chem. Soc.*, 2025, **147**, 41481–41491.

188 S. Hao, M. Cong, Z. Han, H. Xu, T. Liu, M. Guo, X. Ding and Y. Gao, Electrocatalytic formate synthesis from polyethylene terephthalate and carbon dioxide through sulfide-and-reconstruct engineering of catalyst, *Chem. Eng. J.*, 2024, **498**, 155106.

189 P. Sui, M. Zhu, M. Gao, Y. Wang, R. Feng, X. Wang, S. Liu and J. Luo, Energy-conservative CO_2 electroreduction for efficient formate co-generation, *Appl. Catal., B*, 2025, **373**, 125355.

190 S. Kilaparthi, A. Addad, A. Barras, S. Szunerits and R. Boukherroub, Simultaneous upcycling of PET plastic waste and CO_2 reduction through Co-electrolysis: A novel approach for integrating CO_2 reduction and PET hydrolysate oxidation, *J. Mater. Chem. A*, 2023, **11**, 26075–26085.

191 J. Wang, X. Li, M. Wang, T. Zhang, X. Chai, J. Lu, T. Wang, Y. Zhao and D. Ma, Electrocatalytic valorization of poly(ethylene terephthalate) plastic and CO_2 for simultaneous production of formic acid, *ACS Catal.*, 2022, **12**, 6722–6728.

192 L. Zhou, Z. Qu, L. Fu and Y. Ding, Interfacial engineering of In-SnO_2 heterostructure for promoting electrocatalytic CO_2 reduction to formate, *Appl. Catal., B*, 2025, **377**, 125471.

193 H. Wang, B. Yang, R. L. Smith, Y. Su and X. Qi, Electro-reconstructed transition metal electrodes for coupled-upgrading of nitrate pollution and waste poly(ethylene terephthalate) plastics, *Adv. Funct. Mater.*, 2025, **35**, 2425333.

194 M. Du, T. Sun, X. Guo, M. Han, Y. Zhang, W. Chen, M. Han, J. Ma, W. Yuan, C. Zhou, V. Nicolosi, J. Shang, N. Zhang and B. Qiu, Efficient co-production of ammonia and formic acid from nitrate and polyester via paired electrolysis, *Mater. Horiz.*, 2025, **12**, 3743–3751.

195 J. Wang, X. Li, T. Zhang, Y. Chen, T. Wang and Y. Zhao, Electro-reforming polyethylene terephthalate plastic to co-produce valued chemicals and green hydrogen, *J. Phys. Chem. Lett.*, 2022, **13**, 622–627.

196 Z. Chen, G. Zhang, H. Yang, Y. Zhao, A. Pei, P. Wang, J. Yang, J. Zhang, P. Sun, H. Qin, J. Zhan, J. Peng, W. Huang, L. Zhou and G. Chen, $LiCoO_2$-derived Ni-doped catalysts for electrochemical upcycling of polyethylene terephthalate waste to formic acid, *ACS Nano*, 2025, **19**, 26572–26582.

197 H. Wu, H. Tian, L. Chen, W. Luo, S. Li, L. Wang, X. Cui and J. Shi, Advances and insights in electrocatalytic upcycling of polyethylene terephthalate plastic wastes, *Adv. Mater.*, 2025, **38**, e15766.

198 X. Lu, Y. Guo, C. Liang, J. Song, Y. Wu, Z. Wang, Y. Liu, H. Cheng, Z. Zheng, B. Huang and P. Wang, Alloying strategy for the electro-upcycling of polyethylene terephthalate (PET) to C_2 products at industrial-grade current density for over 700 h, *Small*, 2025, **21**, e05978.

199 Q. Xia, S. Gong, J. Wu, Y. Zhai, W. Li, Y. Zhou and X. Zhang, Electrochemical upgrading plastic to organosulfurs through Fe-N_3 single atom catalyst under ambient conditions, *Angew. Chem., Int. Ed.*, 2025, **64**, e202507901.

200 S. Kang, X. Guo, D. Xing, W. Yuan, J. Shang, V. Nicolosi, N. Zhang and B. Qiu, Unraveling the impact of oxygen vacancy on electrochemical valorization of polyester over spinel oxides, *Small*, 2024, **20**, 2406068.

201 H. Wang, R. L. Smith and X. Qi, Upcycling of monomers derived from waste polyester plastics via electrocatalysis, *J. Energy Chem.*, 2025, **101**, 535–561.